Improvement of surface wave methods for constructing subsurface S-wave velocity structures

Tatsunori Ikeda

ACKNOWLEDGEMENTS

First of all, I would like to appreciate my supervisor, Prof. Toshifumi Matsuoka at Kyoto University, who introduced me geophysical exploration, particularly surface wave analysis. Prof. Matsuoka gave me much advice not only for my research but also on how to be a good researcher.

I want to sincerely thank Prof. Toshifumi Matsuoka, Prof. Junji Kiyono, and Prof. Katsuaki Koike for reviewing this dissertation and for providing me constructive comments and suggestions.

I am grateful to Dr. Takeshi Tsuji at Kyushu University for providing me with many helpful comments and suggestions. I am also thankful to Dr. Koichi Hayashi at Geometrics for teaching me the basics of surface wave analysis and providing me various field data. I would like to thank to Dr. Yasuhiro Yamada for his constructive comments and suggestions.

I owe chapter 2 to Dr. Masanori Saito, Professor Emeritus at the Tokyo Institute of Technology, for his kind advice and encouragement of my work.

I owe chapter 3 to Prof. Michael Asten at Monash University. I learned not only the microtremor analysis method but also a lot about Australian culture from Prof. Asten. I also thank Clive Collins and Theodora Volti at Geoscience Australia, who assisted with field observations in Newcastle and Sydney, Australia.

I thank the Port and Airport Research Institute for permission to use the field data. I am grateful to Mr. Toru Nakayama at Japan Petroleum Exploration Co. (JAPEX), who performed the procedure for permission to use seismic data in chapter

6. I also thank Japan Oil, Gas and Metals National Corporation (JOGMEC), Japan Canada Oil Sands Limited (JACOS), and JAPEX for permission to use the three-component seismic data set acquired jointly by JACOS and JOGMEC. I also thank Shikoku Electric Power Co. Inc. and Shikoku Research Institute Inc. for seismic data acquired across the Median Techtronic Line.

I gratefully appreciate the financial support of the Japan Society for the Promotion of Science (JSPS) Fellowship that made it possible to complete this dissertation.

I wish to express my gratitude to all of my colleagues in Kyoto University. In particular, I am grateful to Dr. Ayumu Miyakawa at the National Institute of Advanced Industrial Science and Technology, Dr. Shohei Minato at Delft University of Technology, Dr. Nori Nakata at Stanford University, and Mr. Kazuya Ishitsuka, Mr. Hirotatsu Yamabe, and Mr. Kazuya Kobayashi at Kyoto University for precious discussions.

Finally, I would like to thank to my father, mother, and brother for their moral support and warm encouragement.

TABLE OF CONTENTS

LIST OF FIGURES

Figure

LIST OF TABLES

Table

LIST OF APPENDICES

Appendix

ABSTRACT

Improvement of surface wave methods for constructing subsurface S-wave velocity structures

by

Tatsunori Ikeda

Chair: Toshifumi Matsuoka

Seismic surface waves are guided waves propagating on the surface of the earth. Although surface waves have a long history in seismological studies, the use of surface waves has not been common in geophysical explorations. In a reflection or refraction seismic survey, surface waves are regarded as noise to be eliminated. Recently, however, a seismic exploration method using surface waves has been dramatically developed mainly for engineering purposes. The surface wave method is attractive because it is non-destructive, low cost, and simple compared to other seismic methods. By the surface wave method, subsurface S-wave velocity structures can be efficiently estimated from dispersion of surface waves. Since S-wave velocity structures down to several tens of meters play an important role for evaluating local ground-motion amplification, the surface wave method is one of the most important geophysical methods to be established for earthquake-prone countries such as Japan.

The surface wave method utilizes velocity dispersion of surface waves, which can be extracted from both passive and active seismic data by surface wave analysis. Since surface waves can be theoretically modeled for horizontally layered structures, S-wave

velocity structures can be obtained by inversion of observed surface wave dispersion.

Although a number of applications of the surface wave method have demonstrated the effectiveness of the method, there still remain some issues to be resolved. In this dissertation, we studied several challenging issues with the surface wave method to improve the accuracy of S-wave velocity estimations and further extend its applicability.

First we studied a theoretical issue in surface waves. In the surface wave method, we usually analyze surface waves assuming isotropic media. One reason for this restriction is that the forward modeling of surface waves in anisotropic media is not well developed, although analyses of anisotropy have a potential to reveal attractive information such as lithological alignment, aligned cracks, and stress conditions of media. Therefore, we developed a forward computation method of surface waves on transversely isotropic media with enough accuracy and computation time. It can be effectively used in inversion analysis, which sometimes requires a number of forward calculations.

We then studied the surface wave method using passive seismic data. By inverting observed dispersion curves with the microtremor analysis method, S-wave velocities of sedimentary layers can be retrieved well. The combined use of a horizontal-to-vertical particle motion spectral ratio (HVSR) with dispersion curves can further constrain bedrock depth or velocity contrasts in bedrock. Although a Love wave contribution to Rayleigh waves is necessary for inverting HVSR curves, in some conditions, we need to give an assumption of Love wave contribution. We investigated the effect of the Love wave contribution in the joint inversion of cross-correlations including information on surface wave dispersion with HVSR curves. The results suggested that the choice of the assumption of Love wave contribution is insensitive to the inverted velocity models down to bedrock, although there is an ambiguity to estimating S-wave velocities of bedrock.

The use of higher modes of surface waves is one of the most important issues in the surface wave method because it can improve S-wave velocity estimations, increasing investigation depth. One of the biggest problems in multimode analysis is that several mode components are mixed in observed surface waves. This ambiguity causes significant errors in inversion analysis, and therefore only the fundamental mode of surface waves is sometimes used in the surface wave analysis.

We proposed two kinds of multimode inversion methods considering the effects of different receiver separation distances in array observations for passive seismic data analysis. Multimode inversion can be performed for phase velocity or cross-correlation data before converting into phase velocities. Both methods don't require mode numbering for observed data. The multimode inversion methods were successfully applied for both simulated and field data. The inverted velocity models had a good agreement with logging data.

We also studied higher modes of surface waves in the surface wave method using active sources. To separate mixing multimode surface waves from observed seismic data acquired by active sources, we proposed the deconvolution technique based on the fact that dispersion images can be described by convolution of the theoretical spectrum with absolute values of the array smoothing function. Applying the deconvolution technique can separate two mixing modes from single peaks. Separating mixing modes with the deconvolution technique contributes not only to improving phase velocity estimations but also to identifying mode transition points.

Furthermore, we studied the characteristics of horizontal components of multimode Rayleigh waves. Only the vertical components of Rayleigh waves are usually used in the surface wave method, although Rayleigh waves are also included in horizontal components of P-SV waves. We demonstrated that when an explosive source is located at a deeper depth, additional mode information can be extracted from horizontal component data improving the sensitivity to S-wave velocity changes. This

result suggests that the multimode analysis of horizontal components of Rayleigh waves with vertical component data can be efficiently applied in seismic data acquired for standard reflection seismic surveys with three-component seismometers.

In surface wave analysis, two-dimensional S-wave velocity structures can be obtained by assembling one-dimensional S-wave velocity structures because surface wave analysis requires the assumption of horizontally layered structures in inversion analysis. The key to improving the lateral resolution of estimated S-wave velocity structures is estimating dispersion curves corresponding to one-dimensional S-wave velocity structures, removing lateral heterogeneity. To improve lateral resolution of inverted two-dimensional velocity structures, we proposed the combined technique of CMP cross-correlation analysis for surface waves with applying spatial windows to CMP gathers. The wavelength-dependent window is applied, keeping enough resolution to estimate phase velocities. The proposed method is successfully applied for removing lateral heterogeneity in estimating dispersion curves for one-dimensional velocity structures. Therefore, two-dimensional S-wave velocity structures with high lateral resolution can be obtained by the subsequent inversion.

In summary, we improved surface wave analysis methods to enhance the accuracy of S-wave velocity structure estimations. We demonstrated the effectiveness of the analysis methods by applying both numerically simulated data and field data. Our findings in this dissertation will contribute to extending the applicability of the surface wave method.

CHAPTER I

Introduction

1.1 Motivation

An earthquake is one of the most dangerous natural hazards in the world. Japan is an especially earthquake-prone country because it is surrounded by plate boundaries. The 2011 Tohoku earthquake (Mw 9.0) that occurred northeast of Japan reminded us not only of the fear of earthquakes but also of the importance of a risk assessment for earthquake damages.

In order to evaluate local ground conditions in terms of local ground-motion amplification, impedance, damping, and resonance are key parameters (*Kramer*, 1996). For example, when seismic waves propagate through low-impedance materials (e.g., silt and clay), the amplitude of seismic waves is increased to conserve energy (*McPherson and Hall*, 2013). However, the above parameters are difficult to obtain from a practical point of view. As an alternative approach, S-wave velocity structures down to 30 m (Vs_{30}) are widely used for characterizing site conditions for earthquake site response (e.g. *Borcherdt*, 1994; *Boore*, 2004; *Matsuoka et al.*, 2005; *Wald and Allen*, 2007; *McPherson and Hall*, 2013). S-wave velocity models are also important for use in estimation of strong ground motion by numerical simulation (e.g. *Yamanaka and Yamada*, 2006; *Kasamatsu and Yamanaka*, 2006).

There are several approaches to estimating subsurface S-wave velocity structures.

The direct measurement of S-wave velocities at boreholes gives a good estimation. However, it is difficult to estimate the spatial distribution of S-wave velocity structures, and this method cannot be applied in urban areas due to environmental problems. On the other hand, the shallow S-wave refraction method is a non-destructive method of obtaining good estimates of near-surface S-wave velocities on the assumption of horizontally layered structures. The S-wave refraction method has been commonly used in engineering and environmental studies. In non-horizontal media, however, estimating correct S-wave velocities is difficult because SH-waves cannot be distinguished from converted waves in refraction data (*Xia et al.*, 2002b). We need to establish an alternative approach for constructing near-surface S-wave velocity structures.

1.2 Surface wave method for constructing subsurface S-wave velocity models

To overcome this problem, a geophysical method using seismic surface waves has received a lot of attention and has been significantly developed in recent years because subsurface S-wave velocity structures can be easily obtained at low cost. Surface wave analysis has been widely applied for various fields; for example, for mapping bedrock (*Miller et al.*, 1999), soil liquefaction potential (*Lin et al.*, 2004), pavement structures (*Ryden and Lowe*, 2004), geothermal fields (*Xu et al.*, 2012; *Galgaro et al.*, 2013) and glaciers (*Tsuji et al.*, 2012).

Surface waves are guided waves propagating between different materials. In this dissertation, we focus on surface waves propagating on the surface of the earth. These surface waves can be classified into two types: Rayleigh waves and Love waves. Rayleigh waves are generated by the interaction of P- and SV-waves, whereas Love waves are generated by SH-waves. Rayleigh waves are usually used in surface wave

analysis because they can be easily excited.

The velocities of surface waves on layered media differ in frequency. The energy of surface waves is concentrated down to about one wavelength. Surface waves with shorter wavelengths (high frequencies) are sensitive to S-wave velocities at a shallower depth, whereas surface waves with longer wavelengths (low frequencies) are sensitive to a deeper structure. Thus, the depth sensitivity of surface waves depends on wavelengths (frequencies).

The standard procedure for surface wave analysis can be divided into three main steps (*Socco et al.*, 2010):

(1) acquire the experimental data

(2) process the signal to obtain the experimental dispersion curve

(3) solve the inverse problem to estimate model parameters

In short, subsurface velocity structures can be estimated by the inversion of observed surface waves extracted from acquired seismic data. We note that in forward modeling of surface waves, we should assume one-dimensionally layered structures because theoretical computations of surface waves are constrained to horizontally layered structures developed by *Thomson* (1950) and *Haskell* (1953).

Surface wave analysis methods can be divided into two main methods depending on data acquisition. One is the method of using surface waves included in seismic data excited by an active source. *Nazarian and Stokoe* (1984) introduced the spectral analysis of surface waves (SASW) method, in which dispersion curves of surface waves can be estimated from a pair of receivers. In order to improve the accuracy of dispersion curve estimations, *Park et al.* (1998, 1999a) proposed the method of using multichannel waveform data, referred to as the multichannel analysis of surface waves (MASW).

The other is the microtremor survey method (e.g. *Okada*, 2003) using microtremors (ambient noise). Microtremors are passive seismic data excited by ambient noise from

natural phenomena (e.g., winds and ocean waves) and human activities (e.g., traffic noise and industrial noise). Microtremors at low frequencies (<1 Hz), mostly generated by natural phenomena (*Asten*, 1978), contribute to retrieving deeper S-wave velocity structures, compared to surface wave analysis using active sources.

The spatial autocorrelation (SPAC) method proposed by *Aki* (1957, 1965) and the frequency-wavenumber (*f-k*) method developed by *Lacoss et al.* (1969) and *Capon* (1969) are two main microtremor analysis methods for estimating surface wave dispersion curves with an array observation. As a single-station method, the horizontal-to-vertical particle motion spectral ratio (HVSR) method originally proposed by *Nogoshi and Igarashi* (1971) and widely popularized by *Nakamura* (1989) uses a spectral ratio between vertical and horizontal components of microtremors. A peak of a HVSR curve usually agrees well with the fundamental resonance frequency (*Bonnefoy-Claudet et al.*, 2008). HVSR curves can be efficiently combined with estimated dispersion curves by an active or passive surface wave method to constrain a depth or S-wave velocity of bedrock (e.g. *Scherbaum et al.*, 2003; *Parolai et al.*, 2005; *Arai and Tokimatsu*, 2005). Also, a difference between in observed HVSR frequency maxima for axial and transverse components can be an indicator of 2D effects in the geology (e.g. *Roten et al.*, 2006; *Claprood et al.*, 2012).

1.3 Outline of the dissertation

In this dissertation, we have studied several challenging issues that remain in surface wave analysis for improving subsurface S-wave velocity estimations. Figure 1.1 shows a flowchart of this dissertation. We have considered the use of surface waves from a theoretical aspect of surface waves (chapter 2) to data processing for surface waves included in microtremors (chapters 3 and 4) and in seismic data excited by active sources (chapters 5-7).

In chapter 2, we address the computation of Rayleigh waves on transversely

isotropic media. In surface wave analysis, we usually assume isotropic media. Although analyses of anisotropy have potential to reveal various properties of a medium (e.g. *Crampin*, 1981), very few studies have been conducted on surface wave analysis considering anisotropy. To extend surface wave analysis to anisotropic media, the most important point is a development of stable forward modeling of surface waves with enough accuracy and computational time for inversion. Therefore, we develop the theoretical computation method of Rayleigh waves on transversely isotropic media. The basic theory of P-SV waves and Rayleigh waves is described in chapter 2.

In chapter 3, we apply joint inversion of the SPAC method with HVSR curves for field data acquired in Newcastle, Australia. When we invert HVSR curves by using modelled Rayleigh wave ellipticity, the assumption of Love wave contribution is required in some conditions. We consider the effect of the assumption of Love wave contribution to joint inversion. We also evaluate observed HVSR curves by zero-lag cross-correlations to remove noise effects other than Rayleigh waves.

In chapter 4, we propose two kinds of multimode inversion procedures in the SPAC method considering the effect of different receiver spacings. One is multimode inversion in a phase velocity domain, and the other is in a coherency domain without conversion from coherencies to phase velocities. Although different mode signals are rarely separated by the SPAC method, neither inversion technique requires mode identification for observed data owing to consideration of theoretical amplitude for each mode component. The proposed multimode inversion methods can be easily adapted for cross-correlation data with multiple receiver separation distances.

In chapter 5, we propose the deconvolution technique for separating mixing multimode surface waves in the MASW. When the fundamental mode of surface waves is dominant, a dispersion spectrum constructed by the MASW can be described by convolution of the theoretical spectrum with absolute values of the array smoothing

function (ASF), which can be defined by the receiver configurations. Based on this fact, we apply the deconvolution technique for dispersion spectra by using the ASF to separate mixing mode signals.

In chapter 6, we study fundamental characteristics of horizontal components of multimode Rayleigh waves. Although only vertical components of seismic data are usually used to estimate multimode Rayleigh waves, Rayleigh waves are also included in horizontal components of P-SV waves. The horizontal component of multimode Rayleigh waves has different amplitude distribution from vertical component data. To reveal the advantages of the use of horizontal components of Rayleigh waves, we investigate the effects of source types and source depths on multimode Rayleigh waves in horizontal component data as well as vertical component data.

In chapter 7, we discuss how to improve the lateral resolution of dispersion curve estimations in laterally heterogeneous media. In the inversion of surface wave dispersion curves, we should assume horizontally layered structures. Therefore, in surface wave analysis, two-dimensional S-wave velocity structures are obtained by assembling one-dimensional S-wave velocity structures estimated from local dispersion curves for different reference points. The key to improving lateral resolution of two-dimensional S-wave velocity models is extracting local dispersion curves corresponding to one-dimensional velocity structures beneath reference points. To improve lateral resolution of local dispersion curve estimations, we propose the window-controlled CMP cross-correlation analysis. In the proposed method, wavelength-dependent spatial windows are applied for the cross-correlation gathers to provide a weight for reference points.

In chapter 8, we make a conclusion and describe a recommendation for future work.

These researches have been published in or submitted to the following journals.

Chapter 2: Computation of Rayleigh waves on transversely isotropic media by the

reduced delta matrix method, 2013, *Bulletin of the Seismological Society of America*, **103**, 2083-2093. doi: 10.1785/0120120207.

Chapter 3: Submitted to *Geophysical Journal International*.

Chapter 4: Multimode inversion with amplitude response of surface waves in the spatial autocorrelation method, 2012, *Geophysical Journal International*, **190**, 541-552. doi: 10.1111/j.1365-246X.2012.05496.x.

Chapter 5: A part of chapter 5 has been submitted to *Geophysical Journal International*.

Chapter 6: Submitted to *Geophysics*.

Chapter 7: Window-controlled CMP crosscorrelation analysis for surface waves in laterally heterogeneous media, 2013, *Geophysics*, **78**, EN95-EN105. doi: 10.1190/GEO2013-0010.1.

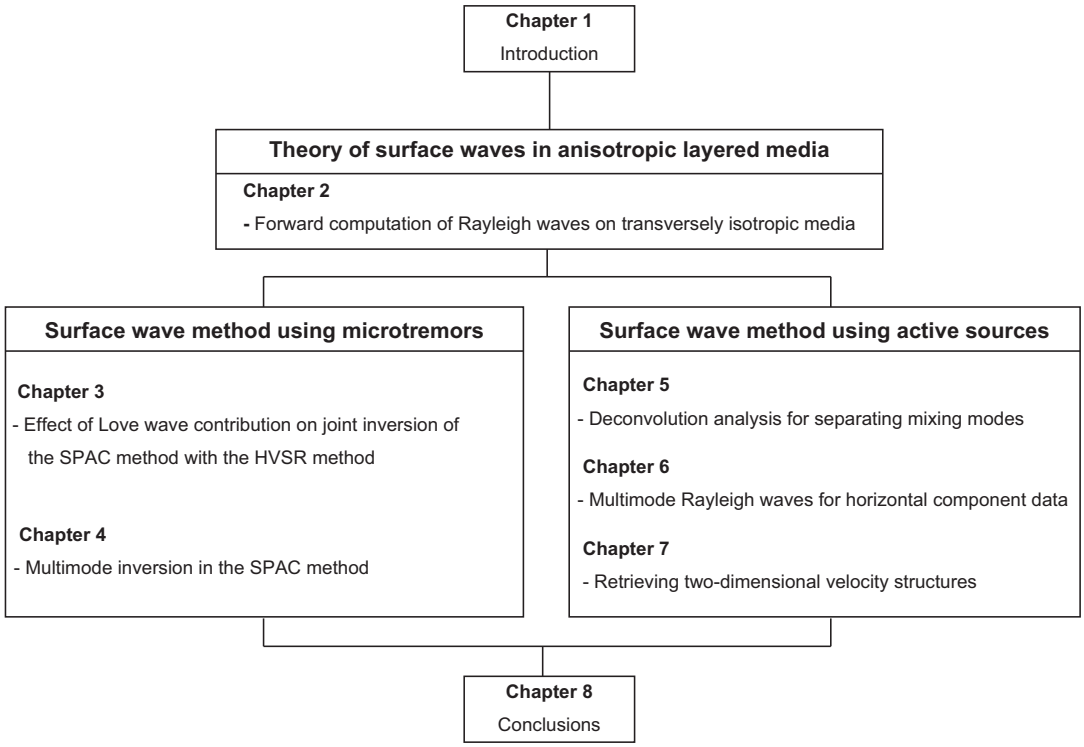

Figure 1.1: Flow chart of this dissertation.

CHAPTER II

Computation of Rayleigh waves on transversely isotropic media by the reduced delta matrix method

2.1 Introduction

Because anisotropy of a medium is mainly caused by crystal alignment, lithological alignment, stress-induced effects, and aligned cracks (*Crampin*, 1981), analyses of seismic anisotropy can reveal information about underground structures. The analysis of S-wave splitting, the separation of an incident S-wave into two directions, is the most general technique used in the study of seismic anisotropy. The strength of the anisotropy and the predominant direction, estimated by S-wave splitting, has been used for structural interpretations of the crust and the upper mantle (e.g. *Crampin et al.*, 1980; *Silver and Chan*, 1991; *Crampin and Peacock*, 2008).

In contrast, analyses of surface wave anisotropy have the potential to determine anisotropy velocities with their depth distribution. The Love-Rayleigh discrepancy (*Anderson*, 1961), or the directional dependence of surface waves, has been used to reveal anisotropy mainly in the lithosphere (e.g. *Maupin and Cara*, 1992; *Friederich and Huang*, 1996; *Gaherty*, 2004; *Alvizuri and Tanimoto*, 2011). Recently, the anisotropy of surface waves propagating on near the surface has been discussed (*Zhang et al.*,

2009; *Dal Moro and Ferigo*, 2011).

The estimation of underground structures using surface waves is based on an inversion in which observed surface waves are compared with theoretically calculated surface waves for assumed media. Theoretical computations of surface waves are complicated and usually confined to horizontally layered media. For isotropic layered media, surface waves can be calculated by the Haskell method (*Haskell*, 1953), in which surface waves are obtained by root searches of the characteristic functions. In the computation of Rayleigh waves, however, the huge exponential functions of the layer matrices in the Haskell method generate numerical instabilities such as underflow at high frequencies. *Dunkin* (1965) overcame this problem by analytically decreasing the order of the characteristic functions by using the delta matrix. *Watson* (1970) further extended this method as the reduced delta matrix method, which can compute Rayleigh waves more efficiently than the standard delta matrix method by decreasing the number of independent variables. *Saito and Kabasawa* (1993) reformulated the reduced matrix method so that Rayleigh waves could be computed without using complex numbers. Similar computational methods to overcome the numerical instabilities of Rayleigh waves have been developed by *Schwab* (1970), *Schwab and Knopoff* (1972), and *Abo-Zena* (1979). *Kennett* (1974) and *Kennett and Kerry* (1979) developed a quite different approach using the Reflection-Transmission (RT) matrix method, which was improved by *Chen* (1993). Although the computational efficiencies of the above methods are different, their accuracies are essentially the same for the computation of the characteristic function (*Buchen and Ben-Hador*, 1996).

Anderson (1961) computed surface waves on transversely isotropic media by extending the Haskell method, and *Crampin* (1970) further extended the Haskell method to general anisotropic media. *Takeuchi and Saito* (1972) developed a method of computing surface waves on transversely isotropic media by a numerical integration of the equations of motion. This approach was extended to general anisotropy by *Kawasaki*

and Koketsu (1990). However, instabilities in the computation of surface waves at high frequencies also exist for anisotropic media. *Park* (1996) developed the computational method for layered anisotropic structures with an arbitrarily oriented axis of symmetry and three constants related to the wave speed variations of P- and S-waves by extending the method of *Chen* (1993). *Mandal and Mitchell* (1986) derived the delta matrix method for transversely isotropic media. As the use of the delta matrix method makes it possible to compute partial derivatives of characteristic functions analytically (*Saito and Kabasawa*, 1993), the group velocity and amplitude response (*Harkrider*, 1964, 1970) can be obtained without loss of numerical precision. However, *Mandal and Mitchell* (1986) did not discuss how to compute Rayleigh waves for transversely isotropic media as they used the delta matrix method for the computation of synthetic waveforms rather than surface waves. Moreover, the delta matrix method has not yet been extended to the reduced delta matrix method.

In this paper, we demonstrate the computation of Rayleigh waves on transversely isotropic media by the reduced matrix method. First, we derive layer matrices in the Haskell method and the matrix elements in the delta matrix method for transversely isotropic media. Second, we extend the delta matrix method to the reduced delta matrix method. Third, we discuss analytical computations of partial derivatives of the characteristic function. Finally, we show the effectiveness of the reduced matrix method by computing the phase velocity, group velocity, ellipticity, and amplitude response of Rayleigh waves on transversely isotropic media.

2.2 P-SV waves on transversely isotropic media

Let us consider a Cartesian coordinate system with the $x - y$ plane horizontal and the z axis vertical. Let the displacement, stress, and density be $\mathbf{u} = (u, v, w)^T$, $\sigma = (\sigma_{xx}, \sigma_{yy}, \sigma_{zz}, \sigma_{yz}, \sigma_{zx}, \sigma_{xy})^T$, and ρ, respectively. Then the equations of motion

can be expressed as

$$\begin{aligned}
\rho\frac{\partial^2 u}{\partial t^2} &= \frac{\partial \sigma_{xx}}{\partial x} + \frac{\partial \sigma_{xy}}{\partial y} + \frac{\partial \sigma_{xz}}{\partial z} \\
\rho\frac{\partial^2 v}{\partial t^2} &= \frac{\partial \sigma_{yx}}{\partial x} + \frac{\partial \sigma_{yy}}{\partial y} + \frac{\partial \sigma_{yz}}{\partial z} \\
\rho\frac{\partial^2 w}{\partial t^2} &= \frac{\partial \sigma_{zx}}{\partial x} + \frac{\partial \sigma_{zy}}{\partial y} + \frac{\partial \sigma_{zz}}{\partial z}.
\end{aligned} \tag{2.1}$$

Assuming Hooke's law, the stress-strain relationship for transversely isotropic media with five independent elastic constants is written as *Anderson* (1961)

$$\begin{pmatrix} \sigma_{xx} \\ \sigma_{yy} \\ \sigma_{zz} \\ \sigma_{yz} \\ \sigma_{zx} \\ \sigma_{xy} \end{pmatrix} = \begin{pmatrix} c_{11} & c_{12} & c_{13} & 0 & 0 & 0 \\ c_{12} & c_{11} & c_{13} & 0 & 0 & 0 \\ c_{13} & c_{13} & c_{33} & 0 & 0 & 0 \\ 0 & 0 & 0 & c_{44} & 0 & 0 \\ 0 & 0 & 0 & 0 & c_{44} & 0 \\ 0 & 0 & 0 & 0 & 0 & \frac{c_{11}-c_{12}}{2} \end{pmatrix} \begin{pmatrix} \frac{\partial u}{\partial x} \\ \frac{\partial v}{\partial y} \\ \frac{\partial w}{\partial z} \\ \frac{\partial w}{\partial y} + \frac{\partial v}{\partial z} \\ \frac{\partial u}{\partial z} + \frac{\partial w}{\partial x} \\ \frac{\partial v}{\partial x} + \frac{\partial u}{\partial y} \end{pmatrix}. \tag{2.2}$$

For P-SV waves, it is sufficient to consider waves propagating along the x axis at a velocity c because transversely isotropic media are symmetric about the z axis. Under this condition we have

$$v = 0 \quad \frac{\partial}{\partial y} = 0. \tag{2.3}$$

Substituting equation 2.3 into equations 2.1 and 2.2, we obtain

$$\begin{aligned}
\rho\frac{\partial^2 u}{\partial t^2} &= \frac{\partial \sigma_{xx}}{\partial x} + \frac{\partial \sigma_{xz}}{\partial z} \\
\rho\frac{\partial^2 w}{\partial t^2} &= \frac{\partial \sigma_{zx}}{\partial x} + \frac{\partial \sigma_{zz}}{\partial z} \\
\sigma_{xx} &= c_{11}\frac{\partial u}{\partial x} + c_{13}\frac{\partial w}{\partial z} \\
\sigma_{zz} &= c_{13}\frac{\partial u}{\partial x} + c_{33}\frac{\partial w}{\partial z} \\
\sigma_{zx} &= c_{44}\left(\frac{\partial u}{\partial z} + \frac{\partial w}{\partial x}\right).
\end{aligned} \tag{2.4}$$

We assume solutions of displacements and stresses in the form of

$$\begin{aligned}
w &= y_1(z)e^{-i(\omega t - kx)} \\
\sigma_{zz} &= y_2(z)e^{-i(\omega t - kx)} \\
u &= iy_3(z)e^{-i(\omega t - kx)} \\
\sigma_{zx} &= iy_4(z)e^{-i(\omega t - kx)},
\end{aligned} \tag{2.5}$$

where t is time, ω is angular frequency, k is horizontal wavenumber, and $\mathbf{y} = (y_1, y_2, y_3, y_4)^T$ is an unknown function to be determined. Substituting equation 2.5 into equation 2.4 and assuming that ρ and c_{ij} depend only on z, we obtain the following linear differential equations:

$$\begin{aligned}
\frac{dy_1(z)}{dz} &= \frac{1}{c_{33}}y_2(z) + \frac{c_{13}}{c_{33}}ky_3(z) \\
\frac{dy_2(z)}{dz} &= -\rho\omega^2 y_1(z) + ky_4(z) \\
\frac{dy_3(z)}{dz} &= -ky_1(z) + \frac{1}{c_{44}}ky_4(z) \\
\frac{dy_4(z)}{dz} &= -\frac{c_{13}}{c_{33}}ky_2(z) + \left[\left(c_{11} - \frac{c_{13}^2}{c_{33}}\right)k^2 - \rho\omega^2\right]y_3(z).
\end{aligned} \tag{2.6}$$

Even if $c_{ij}(z)$ is discontinuous along the z axis, $y_i(z)$ must be continuous.

As we consider only homogeneous media in the following discussion, we suppose

solutions of the above linear differential equations in the forms

$$y_1(z) = e^{\nu z} \quad y_3(z) = \epsilon e^{\nu z}. \tag{2.7}$$

Substituting equation 2.7 into equation 2.6, we obtain

$$\begin{aligned} y_2(z) &= (c_{33}\nu - c_{13}k\epsilon)e^{\nu z} \\ y_4(z) &= c_{44}(k + \nu\epsilon)e^{\nu z} \\ \epsilon &= \frac{c_{33}\nu^2 + \rho\omega^2 - c_{44}k^2}{(c_{13} + c_{44})k\nu} \\ &= \frac{(c_{13} + c_{44})k\nu}{c_{11}k^2 - \rho\omega^2 - c_{44}\nu^2}. \end{aligned} \tag{2.8}$$

From the third equation in equation 2.8, we obtain the following quartic equation about ν:

$$\begin{aligned} c_{33}c_{44}\nu^4 + [c_{44}(\rho\omega^2 - c_{44}k^2) + c_{33}(\rho\omega^2 - c_{11}k^2) \\ +(c_{13} + c_{44})^2k^2]\nu^2 + (\rho\omega^2 - c_{44}k^2)(\rho\omega^2 - c_{11}k^2) \\ = 0. \end{aligned} \tag{2.9}$$

Solutions for ν^2 in equation 2.9 can be expressed as

$$\nu^2 = \frac{-M_1 \pm \sqrt{M_1^2 - 4c_{33}c_{44}M_2}}{2c_{33}c_{44}}, \tag{2.10}$$

where

$$\begin{aligned} M_1 &= c_{44}(\rho\omega^2 - c_{44}k^2) + c_{33}(\rho\omega^2 - c_{11}k^2) + (c_{13} + c_{44})^2k^2 \\ M_2 &= (\rho\omega^2 - c_{44}k^2)(\rho\omega^2 - c_{11}k^2), \end{aligned} \tag{2.11}$$

and then the solutions for ν can be expressed as

$$\begin{aligned}\nu_1 &= \sqrt{\frac{-M_1 + \sqrt{M_1^2 - 4c_{33}c_{44}M_2}}{2c_{33}c_{44}}} \quad \nu_2 = -\nu_1 \\ \nu_2 &= \sqrt{\frac{-M_1 - \sqrt{M_1^2 - 4c_{33}c_{44}M_2}}{2c_{33}c_{44}}} \quad \nu_4 = -\nu_3.\end{aligned} \tag{2.12}$$

A general solution for $\mathbf{y}$ in a homogeneous layer can be expressed as follows:

$$\begin{aligned}y_1(z) &= \sum_{m=1}^{4} F_m e^{\nu_m z} \\ y_2(z) &= \sum_{m=1}^{4} (c_{33}\nu_m - c_{13}k\epsilon_m) F_m e^{\nu_m z} \\ y_3(z) &= \sum_{m=1}^{4} \epsilon_m F_m e^{\nu_m z} \\ y_4(z) &= \sum_{m=1}^{4} c_{44}(k + \nu_m \epsilon_m) F_m e^{\nu_m z}.\end{aligned} \tag{2.13}$$

Here, F_m is a constant of integration. We then replace $e^{\nu_m z}$ in equation 2.13 with a hyperbolic function. For example, $y_1(z)$ can be rewritten as

$$\begin{aligned}y_1(z) &= \sum_{m=1}^{4} F_m e^{\nu_m z} \\ &= F_1 e^{\nu_1 z} + F_2 e^{\nu_2 z} + F_3 e^{\nu_3 z} + F_4 e^{\nu_4 z} \\ &= F_1 e^{\nu_1 z} + F_2 e^{-\nu_1 z} + F_3 e^{\nu_3 z} + F_4 e^{-\nu_3 z} \\ &= (F_1 + F_2) cosh\nu_1 z + (F_1 - F_2) sinh\nu_1 z \\ &+ (F_3 + F_4) cosh\nu_3 z + (F_3 - F_4) sinh\nu_3 z.\end{aligned} \tag{2.14}$$

Finally, the general solution $\mathbf{y}$ can be expressed as

$$\mathbf{y}(z) = \mathbf{D}(z)\mathbf{F}, \tag{2.15}$$

where

$$\mathbf{D}(z) = \begin{pmatrix} C_1(z) & S_1(z) & C_3(z) & S_3(z) \\ d_1 S_1(z) & d_1 C_1(z) & d_2 S_3(z) & d_2 C_3(z) \\ \epsilon_1 S_1(z) & \epsilon_1 C_1(z) & \epsilon_3 S_3(z) & \epsilon_3 C_3(z) \\ c_{44} d_3 C_1(z) & c_{44} d_3 S_1(z) & c_{44} d_4 C_3(z) & c_{44} d_4 S_3(z) \end{pmatrix}$$

$$\mathbf{F}(z) = \begin{pmatrix} F_1 + F_2 \\ F_1 - F_2 \\ F_3 + F_4 \\ F_3 - F_4 \end{pmatrix} \tag{2.16}$$

and

$$\begin{aligned} C_1(z) &= cosh\nu_1 z \\ C_3(z) &= cosh\nu_3 z \\ S_1(z) &= sinh\nu_1 z \\ S_3(z) &= sinh\nu_3 z \\ d_1 &= c_{33}\nu_1 - c_{13}k\epsilon_1 \\ d_2 &= c_{33}\nu_3 - c_{13}k\epsilon_3 \\ d_3 &= k + \nu_1\epsilon_1 \\ d_4 &= k + \nu_3\epsilon_3. \end{aligned} \tag{2.17}$$

2.3 Computation of Rayleigh waves

2.3.1 Haskell method

We assume a stacked-layer structure in which each layer is homogeneous as in Figure 2.1. Here, we define $z_{n-1} = 0 < z < z_n = h_n$ as the n-th layer. If we define the origin of the z axis to be at z_{n-1}, from equation 2.15 the general solution of $\mathbf{y}_n$

within the n-th layer can be expressed as

$$\mathbf{y}_n(z) = \mathbf{D}_n(z)\mathbf{F}_n. \tag{2.18}$$

Substituting $z = z_{n-1} = 0$ into equation 2.18, we obtain

$$\mathbf{y}_n(0) = \mathbf{D}_n(0)\mathbf{F}_n, \tag{2.19}$$

where

$$\mathbf{D}_n(0) = \begin{pmatrix} 1 & 0 & 1 & 0 \\ 0 & d_1 & 0 & d_2 \\ 0 & \epsilon_1 & 0 & \epsilon_3 \\ c_{44}d_3 & 0 & c_{44}d_4 & 0. \end{pmatrix} \tag{2.20}$$

From equation 2.19, $\mathbf{F}_n$ is solved as

$$\mathbf{F}_n = \mathbf{D}_n^{-1}(0)\mathbf{y}_n(0) \tag{2.21}$$

where

$$\mathbf{D}_n^{-1}(0) = \begin{pmatrix} -\frac{d_4}{d_5} & 0 & 0 & \frac{1}{c_{44}d_5} \\ 0 & -\frac{\epsilon_3}{c_{33}d_6} & \frac{d_2}{c_{33}d_6} & 0 \\ \frac{d_3}{d_5} & 0 & 0 & -\frac{1}{c_{44}d_5} \\ 0 & \frac{\epsilon_1}{c_{33}d_6} & -\frac{d_1}{c_{33}d_6} & 0 \end{pmatrix} \tag{2.22}$$

and

$$d_5 = \nu_1\epsilon_1 - \nu_3\epsilon_3 \quad d_6 = \nu_3\epsilon_1 - \nu_1\epsilon_3. \tag{2.23}$$

Substituting equation 2.21 into equation 2.18, the general solution for the n-th layer can be written as

$$\mathbf{y}_n(z) = \mathbf{A}_n(z)\mathbf{y}_n(0), \tag{2.24}$$

where $\mathbf{A}_n$ is defined by

$$\mathbf{A}_n(z) = \mathbf{D}_n(z)\mathbf{D}_n^{-1}(0), \tag{2.25}$$

which is called Haskell's layer matrix. Haskell's layer matrices are listed in Appendix A. By using these relationships among d_i described in Appendix B, the layer matrices described by 16 elements as in *Mandal and Mitchell* (1986) decrease to 10 elements, which is the same number as for isotropic media. Equation 2.24 indicates that the solution in the n-th layer can be obtained from the solution at the bottom of the n th layer with elastic constants and the density of the n-th layer. Since the solution of the upper surface in the n-th layer must be continuous with that of the bottom in the $(n+1)$-th layer, it can be expressed as

$$\mathbf{y}_{n+1}(h_n) = \mathbf{y}_n(h_n) = \mathbf{A}_n(h_n)\mathbf{y}_n(0). \tag{2.26}$$

Thus, the solution at the top of the $(n+1)$-th layer can be generally expressed as

$$\mathbf{y}_{n+1}(h_{n+1} + h_n) = \mathbf{A}_{n+1}(h_{n+1})\mathbf{A}_n(h_n)\mathbf{y}_n(0). \tag{2.27}$$

By connecting the layer matrices to initial values at the bottom of the N-layered medium, the general solution in the horizontally layered medium can be obtained. If we define $z = 0$ as the boundary of the homogeneous half-space and $z = H$ as the

free surface, the solution on the free surface can be expressed as

$$\mathbf{y}_N(H) = \mathbf{A}_N(h_N)\mathbf{A}_{N-1}(h_{N-1})\cdots\mathbf{A}_3(h_3)\mathbf{A}_2(h_2)\mathbf{y}_1(0). \tag{2.28}$$

If the boundary of the half-space is deep enough and a source is located at $z > 0$, only down-going waves exist at $z < 0$. The solution under this condition must be $F_2 = F_4 = 0$ in equation 2.13. Thus, if we define the following initial values:

$$\mathbf{y}_a(0) = \begin{pmatrix} 1 \\ d_1 \\ \epsilon_1 \\ c_{44}d_3 \end{pmatrix} \quad \mathbf{y}_b(0) = \begin{pmatrix} 1 \\ d_2 \\ \epsilon_3 \\ c_{44}d_4 \end{pmatrix} \tag{2.29}$$

and solutions for these initial values as $\mathbf{y}_a(z)$, $\mathbf{y}_b(z)$, respectively, the general solution can be expressed as

$$\mathbf{y}(z) = F_1\mathbf{y}_a(z) + F_3\mathbf{y}_b(z). \tag{2.30}$$

From the boundary condition of vanishing stress at the free surface,

$$\begin{aligned} [\mathbf{y}(H)]_2 &= F_1[\mathbf{y}_a(H)]_2 + F_3[\mathbf{y}_b(H)]_2 = 0 \\ [\mathbf{y}(H)]_4 &= F_1[\mathbf{y}_a(H)]_4 + F_3[\mathbf{y}_b(H)]_4 = 0. \end{aligned} \tag{2.31}$$

A nontrivial solution of equation 2.31 exists only when

$$\Delta_R(c,\omega) = [\mathbf{y}_a(H)]_4[\mathbf{y}_b(H)]_4 - [\mathbf{y}_b(H)]_2[\mathbf{y}_a(H)]_4 = 0, \tag{2.32}$$

where Δ_R and equation 2.32 are called the characteristic function and the characteristic equation of Rayleigh waves, respectively. Δ_R can be obtained from the elastic constants, the density and thickness of each layer as functions of the phase velocity c

and frequency. The phase velocity c that satisfies equation 2.32 is defined to be that of Rayleigh waves. However, phase velocities at high frequencies cannot be obtained accurately due to loss of numerical precision in the computation of the characteristic functions.

2.3.2 Reduced delta matrix method

In this section, we apply the reduced delta matrix method (*Watson*, 1970; *Saito and Kabasawa*, 1993) for transversely isotropic media to prevent numerical instability at high frequencies. First, we define the following minor referred to as a delta matrix (also referred to as a compound matrix):

$$Y_{ij}(z) = [\mathbf{y}_a(z)]_i[\mathbf{y}_b(z)]_j - [\mathbf{y}_b(z)]_i[\mathbf{y}_a(z)]_j, \qquad i < j. \tag{2.33}$$

Because of the following relationship,

$$Y_{ji}(z) = -Y_{ij}(z) \quad Y_{ii}(z) = 0, \tag{2.34}$$

there are only six independent elements in $Y_{ij}(z)$. The characteristic function of a Rayleigh wave is defined in terms of $Y_{ij}(z)$ as

$$\Delta_R = Y_{24}(H). \tag{2.35}$$

The delta matrix elements satisfy a set of linear differential equations. By differ-

entiating the defining equation 2.33 and using equation 2.6, we obtain

$$\begin{aligned}
\frac{dY_{12}(z)}{dz} &= kY_{14}(z) - \frac{c_{13}}{c_{33}}kY_{23}(z) \\
\frac{dY_{13}(z)}{dz} &= \frac{1}{c_{44}}Y_{14}(z) + \frac{1}{c_{33}}Y_{23}(z) \\
\frac{dY_{14}(z)}{dz} &= -\frac{c_{13}}{c_{33}}kY_{12}(z) + \left[\left(c_{11} - \frac{c_{13}^2}{c_{33}}\right)k^2 - \rho\omega^2\right]Y_{13}(z) \\
&\quad + \frac{1}{c_{33}}Y_{24}(z) + \frac{c_{13}}{c_{33}}kY_{34}(z) \\
\frac{dY_{23}(z)}{dz} &= kY_{12}(z) - \rho\omega^2 Y_{13}(z) + \frac{1}{c_{44}}Y_{24}(z) - kY_{34}(z) \\
\frac{dY_{24}(z)}{dz} &= -\rho\omega^2 Y_{14}(z) + \left[\left(c_{11} - \frac{c_{13}^2}{c_{33}}\right)k^2 - \rho\omega^2\right]Y_{23}(z) \\
\frac{dY_{34}(z)}{dz} &= -kY_{14}(z) + \frac{c_{13}}{c_{33}}kY_{23}(z).
\end{aligned} \tag{2.36}$$

The sixth-order equation can be reduced to a fifth-order equation. From the first and last equations, we have

$$\frac{dY_{12}(z)}{dz} + \frac{dY_{34}(z)}{dz} = \quad 0, \tag{2.37}$$

that is,

$$Y_{12}(z) + Y_{34}(z) = const.. \tag{2.38}$$

Because we are interested only in surface waves, $Y_{ij}(z)$ must satisfy the radiation condition

$$Y_{ij}(z) \to 0 \qquad as\ z \to -\infty. \tag{2.39}$$

Therefore, the constant on the right-hand side in equation 2.38 should be zero, and

the delta matrix for surface waves satisfies

$$Y_{12}(z) = -Y_{34}(z). \tag{2.40}$$

Thus $Y_{34}(z)$ can be eliminated in equation 2.36.

For a stacked layer structure, we can integrate equation 2.36 by the matrix method. Substituting equation 2.24 into equation 2.33, we obtain

$$Y_{ij}(z) = \sum_{k} \sum_{l>k} b_{ijkl}(z) Y_{kl}(0), \tag{2.41}$$

where

$$b_{ijkl}(z) = [\mathbf{A}(z)]_{ik}[\mathbf{A}(z)]_{jl} - [\mathbf{A}(z)]_{il}[\mathbf{A}(z)]_{jk}. \tag{2.42}$$

The initial values at the boundary of the homogeneous half-space $z = 0$ can be obtained from equation 2.29 as

$$\begin{aligned}
Y_{12}(0) &= d_2 - d_1 \\
Y_{13}(0) &= \epsilon_3 - \epsilon_1 \\
Y_{14}(0) &= -c_{44} d_5 \\
Y_{23}(0) &= -c_{33} d_6 \\
Y_{24}(0) &= c_{44}(d_1 d_4 - d_2 d_3) \\
Y_{34}(0) &= c_{44}(\epsilon_1 d_4 - \epsilon_3 d_3) \\
&= -Y_{12}(0).
\end{aligned} \tag{2.43}$$

Because there are 5 independent values in $Y_{ij}(z)$, there are 25 elements in b_{ijkl}. Matrix elements in the delta matrix method are described by 21 independent elements, which is the same number as in *Mandal and Mitchell* (1986) due to symmetry. By using

the relationships in Appendix B, 21 independent elements of the delta matrix method further decreases to 15 independent elements (Appendix C), which is the same number as in isotropic media. The terms $C_1S_1, C_3S_3, C_1^2, C_3^2, S_1^2, S_3^2$ are cancelled out in the derivation of b_{ijkl} as in the case of isotropic media. This contributes to a decrease in the order of the characteristic function and prevents loss of numerical precision at high frequencies since C and S increase exponentially with increasing frequency when ν is a real number.

Our derivation shows that the number of independent variables in the delta matrices and matrix elements are decreased to 5 and 15, respectively, which are the same as those in the reduced matrix method for isotropic media. In this way, we extend the delta matrix method for transversely isotropic media to the reduced delta matrix method. Connecting the matrix elements of each layer to initial values at the bottom of the N-layered medium, the characteristic function can be obtained as equation 2.35.

For isotropic media, all the computations can be implemented in real numbers (*Buchen and Ben-Hador*, 1996) in the Haskell or (reduced) delta matrix methods. For transversely isotropic media, however, there is a possibility that ν as described in equation 2.12 becomes complex depending on the elastic constants, phase velocity, and frequency. If ν is complex, then the computation of complex numbers must be implemented in the algorithm. Consequently more computational time is required for transversely isotropic media. Because the coefficients of the differential equations described in equations 2.6 and 2.36 are real, however, the layer matrices and matrix elements themselves are also real, even if ν is complex. In contrast, the computation method of *Takeuchi and Saito* (1972), which directly solves the differential equations by a numerical integral, can avoid the use of complex numbers. Note that in the RT matrix method, complex numbers must be used even for isotropic media.

The characteristic function obtained by multiplying the matrix elements for each

layer by the initial values becomes real for isotropic media because the initial values are real. However, the initial values for transversely isotropic media described in equation 2.43 are not real numbers when ν is complex. In this case, ϵ_1 and ϵ_3 become complex conjugates because a branch of the square root of equation 2.12 can be taken where ν_1 and ν_3 are complex conjugates. From these features, we can find values of $Y_{13}(0)$ in equation 2.43 purely imaginary as follows:

$$Y_{13}(0) = \epsilon_3 - \epsilon_1 = 2Im(\epsilon_3). \tag{2.44}$$

Other initial values can be found purely imaginary as well. As a result, even if ν is complex, the characteristic function can be defined as real by multiplying the initial values by an imaginary number.

We obtain the phase velocities of Rayleigh waves by the following procedure. First, the characteristic functions are calculated by changing the phase velocities by a constant interval at a fixed frequency. Second, when the characteristic function changes sign, its intermediate velocity is kept as the tentative phase velocity for the frequency. Third, the estimation of the phase velocities is improved by using Newton' s method with the tentative phase velocity as the initial value. Finally, the dispersion curve can be obtained by repeating this procedure for necessary frequencies.

2.3.3 Computations of group velocity, ellipticity, and amplitude response

In this section, we explain the computation of group velocity, ellipticity, and amplitude response of Rayleigh waves by using the delta matrix. Following *Ben-Menahem and Singh* (1981), the group velocity U is defined as

$$\frac{1}{U} = \frac{1}{c} - \frac{\omega}{c^2}\frac{dc}{d\omega}, \tag{2.45}$$

where the derivative is taken along the dispersion curve. From the implicit function theorem, the derivatives of the characteristic equation 2.32 can be expressed as

$$\frac{\partial \Delta_R}{\partial \omega} + \frac{\partial \Delta_R}{\partial c}\frac{dc}{d\omega} = 0. \tag{2.46}$$

By using equations 2.45 and 2.46, the group velocity can be written as

$$\frac{c}{U} = 1 + \frac{\omega}{c}\frac{\partial \Delta_R}{\partial \omega}\left(\frac{\partial \Delta_R}{\partial c}\right)^{-1}. \tag{2.47}$$

Because the dispersion curve is defined by $\Delta_R(c, \omega) = 0$, the phase velocity in this equation must be at the root of the characteristic function, and the partialderivatives of the characteristic functions must be computed at this phase velocity. Although the partial derivatives of the angular frequency and phase velocity can be easily computed by numerical differentiation, they can be computed analytically by the delta matrix method (*Saito and Kabasawa*, 1993).

The partial derivatives of equation 2.41 with respect to the phase velocity can be written as

$$\frac{\partial Y_{ij}(z)}{\partial c} = \sum_k \sum_{l>k} \frac{\partial b_{ijkl}(z)}{\partial c} Y_{kl}(0) + \sum_k \sum_{l>k} b_{ijkl}(z) \frac{\partial Y_{kl}(0)}{\partial c}. \tag{2.48}$$

This equation indicates that the partial derivative of $Y_{ij}(z)$ with respect to the phase velocity can be obtained by using the partial derivatives of b_{ijkl} and $Y_{ij}(0)$. For stacked layer media, Y_{ij} at the boundary of each layer is required and must be simultaneously computed by using equation 2.41. From equations 2.10 and 2.11, the partial

derivatives of M_1, M_2, and ν with respect to the phase velocity can be expressed as

$$\begin{aligned}
\frac{\partial M_1}{\partial c} &= 2\frac{k^2}{c}[c_{11}c_{33} + c_{44}^2 - (c_{13} + c_{44})^2] \\
\frac{\partial M_2}{\partial c} &= 2\frac{k^2}{c}[(c_{11} + c_{44})\rho\omega^2 - 2c_{11}c_{44}k^2] \\
\frac{\partial \nu}{\partial c} &= \frac{1}{4c_{33}c_{44}\nu}\left[-\frac{\partial M_1}{\partial c} \pm \frac{1}{\sqrt{M_1^2 - 4c_{33}c_{44}M_2}}\left(M_1\frac{\partial M_1}{\partial c} - 2c_{33}c_{44}\frac{\partial M_2}{\partial c}\right)\right].
\end{aligned} \tag{2.49}$$

By applying a similar procedure, the partial derivatives of ϵ_i and d_i with respect to the phase velocity can be also obtained. Although it is too complicated to transcribe the partial derivatives of b_{ijkl} and $Y_{ij}(0)$ with respect to the phase velocity, they can be calculated by computer by using the differential formula. In this way, we can compute the partial derivative of $Y_{ij}(z)$ with respect to the phase velocity without numerical differentiation. The partial derivative of $Y_{ij}(z)$ with respect to the angular frequency can obtained similarly. Finally, by substituting the calculated partial derivatives of the characteristic functions at the free surface $z = H$ into equation 2.47, the group velocity of Rayleigh waves can be obtained.

The ellipticity and amplitude response of Rayleigh waves as defined by *Harkrider* (1970) and *Tokimatsu* (1997) can be written as follows:

$$H/V = -\frac{Y_{23}(H)}{Y_{12}(H)} = -\frac{Y_{12}(H)}{Y_{14}(H)}. \tag{2.50}$$

$$A_R = -\frac{k^2}{c}Y_{14}(H)\left(\frac{\partial Y_{24}(H)}{\partial c}\right)^{-1}. \tag{2.51}$$

2.4 Sample calculation

2.4.1 Transversely isotropic model

We computed Rayleigh waves on transversely isotropic media to verify the effectiveness of the reduced delta matrix method. The computational model is a structure with 20 horizontal layers overlying a halfspace of which 17 layers are transversely isotropic used in *Harkrider and Anderson* (1962)(Table 2.1). Figure 2.2 shows the calculated phase velocity, group velocity, ellipticity, and amplitude response of the fundamental mode and the first higher mode for Rayleigh waves. The Rayleigh wave results with the Haskell method by *Harkrider and Anderson* (1962) are also described in Figure 2.2. Note that the results by *Harkrider and Anderson* (1962) are only for the fundamental mode of Rayleigh waves and there are no results for the amplitude response.

In the computation by *Harkrider and Anderson* (1962), if ν was complex, the elastic constants of its layer were replaced with ones from an isotropic layer to avoid the computation of complex dispersion. Although the program we developed can implement the computation of complex numbers, we also make the replacement if ν is complex in order to compute Rayleigh waves that correspond to the results of *Harkrider and Anderson* (1962). We found that ν becomes complex near the roots of the characteristic functions for the 9 th, 10 th, 15 th, and 16 th layers depending on the frequency.

The calculated phase velocity and ellipticity are almost the same. However, there is a difference in the group velocity at about 8 Hz. This difference would come from how the partial derivatives of the characteristic function are computed. *Harkrider and Anderson* (1962) computed them by numerical differentiation which generates numerical errors near the group velocity minimum due to a lack of significance in the root k differences as written in their original paper. On the other hands, we analyti-

cally computed them from the delta matrix, as described in the previous section. The numerical accuracy in the calculation of partial derivatives by the implicit function theorem depends only on machine precision (*Cercato*, 2007).

2.4.2 Computational efficiency

We compared the computational time by the reduced delta matrix method with that by the delta matrix method. For the layered model described in Table 2.1, surface waves were computed from 2nd to 21st layered models. Characteristic functions with 5000 (phase velocities) $\times$ 200 (frequencies up to 100 Hz with frequency spacing of 0.5 Hz) pixels were calculated for each model. Phase velocities, group velocities, ellipticities and amplitude responses for all the modes were calculated. Figure 2.3 shows the comparison of the computational time by the reduced delta matrix method with those by the delta matrix method using 21 and 15 independent matrix elements. By using the reduced delta matrix method, the computational efficiency is increased by about 15.8 and 3.0 percent compared with the delta matrix method using 21 and 15 independent elements, respectively.

2.5 Summary

We have developed the reduced delta matrix method to compute Rayleigh waves, which has a better computational efficiency than the standard delta matrix method for transversely isotropic media.

First, we obtained Haskell's layer matrices for Rayleigh waves from P-SV waves in transversely isotropic media. The matrix elements for the delta matrix method were then derived from the delta matrix. We extended the delta matrix method to the reduced delta matrix method by showing that the delta matrices and matrix elements in the delta matrix method can be expressed by 5 and 15 independent variables, respectively. These are the same number of independent variables as for

isotropic media.

Moreover, we showed that if ν for the initial values is complex, the initial values for the delta matrix are purely imaginary. In this case, the characteristic function can be defined as real by multiplying the imaginary numbers by the initial values, although computer computation of complex numbers is required. We described how to compute analytically the partial differential of the characteristic function. The results of the computation example demonstrated the stability and computational efficiency of the reduced delta matrix method. We can state that the computation of Rayleigh waves in transversely isotropic media can be efficiently implemented by the reduced delta matrix method without loss of numerical precision at high frequencies.

Table 2.1: Parameters used for the transversely isotropic model used in *Harkrider and Anderson* (1962)

Layer Number	Thickness $(feet)$	V_p $(kfeet/s)$	V_s $(kfeet/s)$	$Density$ (g/cm^3)	PHI	NADA
1	5.00	1.2040	0.2600	2.0000	1.0000	1.0000
2	5.00	1.4880	0.4490	2.0000	1.0000	1.0000
3	5.00	1.3930	0.7320	2.0000	1.0000	1.0000
4	5.00	1.6060	1.0000	2.2500	1.0000	1.0000
5	5.00	1.7000	1.0860	2.2500	0.9060	0.9500
6	5.00	1.7000	1.0630	2.2500	0.9060	0.9500
7	5.00	1.7950	1.0630	2.2500	0.9060	0.8400
8	5.00	1.7950	0.9450	2.2500	0.9060	0.8400
9	5.00	1.8660	1.0000	2.2500	0.6280	0.8400
10	5.00	1.8660	1.0630	2.2500	0.6280	0.8400
11	5.00	2.0000	1.4170	2.2500	0.6280	0.7520
12	5.00	2.2440	1.4170	2.2500	0.6280	0.7520
13	5.00	3.8970	1.6060	2.5000	0.9500	0.9300
14	5.00	5.4080	1.6530	2.5000	0.9500	0.9300
15	5.00	5.4080	1.6300	2.5000	0.8500	0.9300
16	5.00	5.4080	1.6300	2.5000	0.8500	0.9300
17	5.00	5.6920	2.0310	2.5000	0.8500	0.9000
18	5.00	5.5970	1.7700	2.5000	0.8500	0.9000
19	5.00	5.5030	1.8420	2.5000	0.9000	0.9300
20	5.00	6.1170	1.7240	2.5000	0.9000	0.9300
21	∞	6.2350	2.0000	2.6000	0.9000	0.9300

[1]

[1]Note that we analogize units of each parameter because they are not described in *Harkrider and Anderson* (1962). PHI is squared ratio of vertical to horizontal traveling P-wave velocity and NADA is squared ratio of 45° to horizontal traveling P-wave velocity.

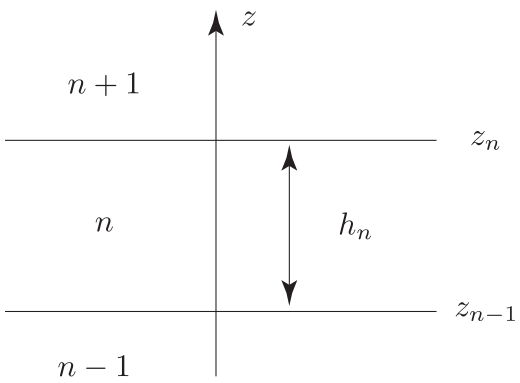

Figure 2.1: Coordinate axis for a stacked layer structure.

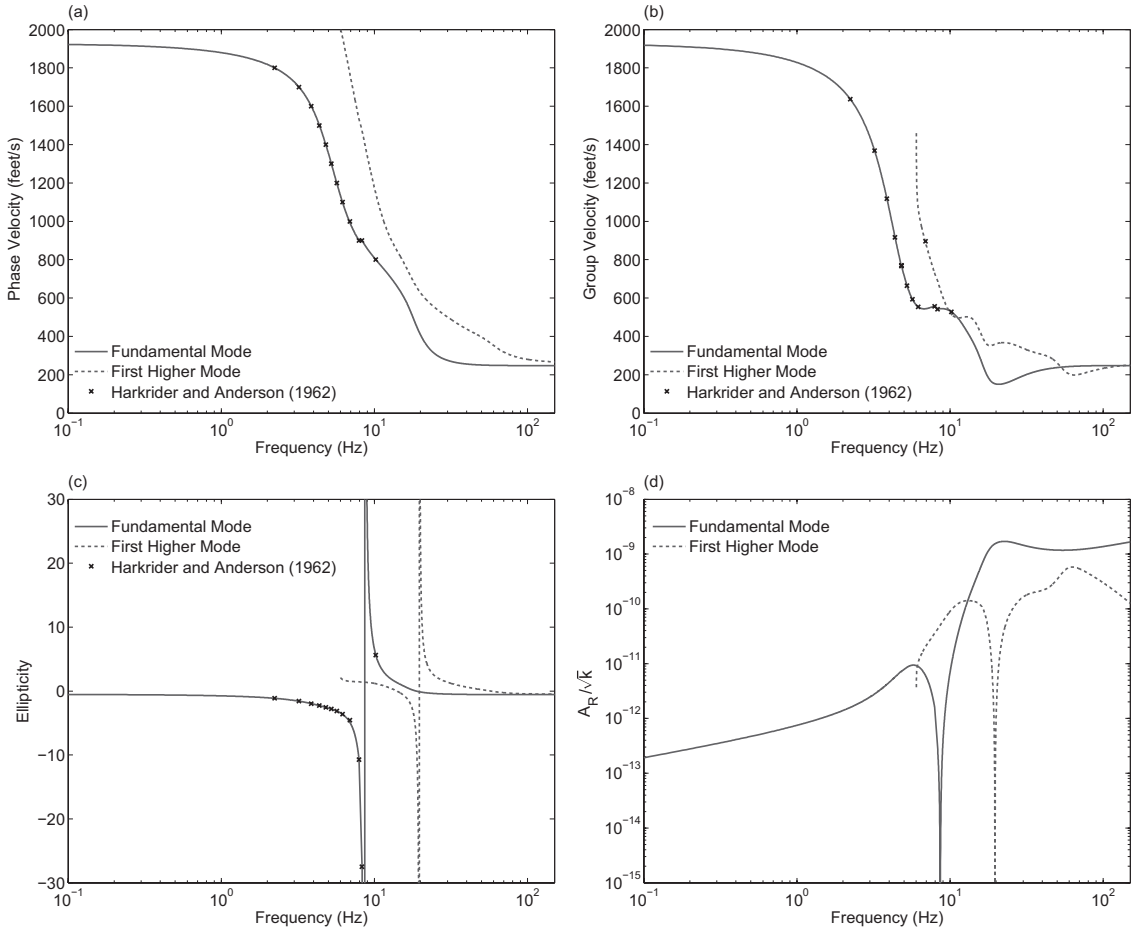

Figure 2.2: Comparison of the fundamental and first higher modes of Rayleigh waves for the transversely isotropic model shown in Table 2.1 used in *Harkrider* (1964). (a) Phase velocity, (b) Group velocity, (c) Ellipticity, and (d) Amplitude response. Note that the dimension of the amplitude response corresponds to one when the units of the velocity and density are $feet/s$ and kg/m^3, respectively.

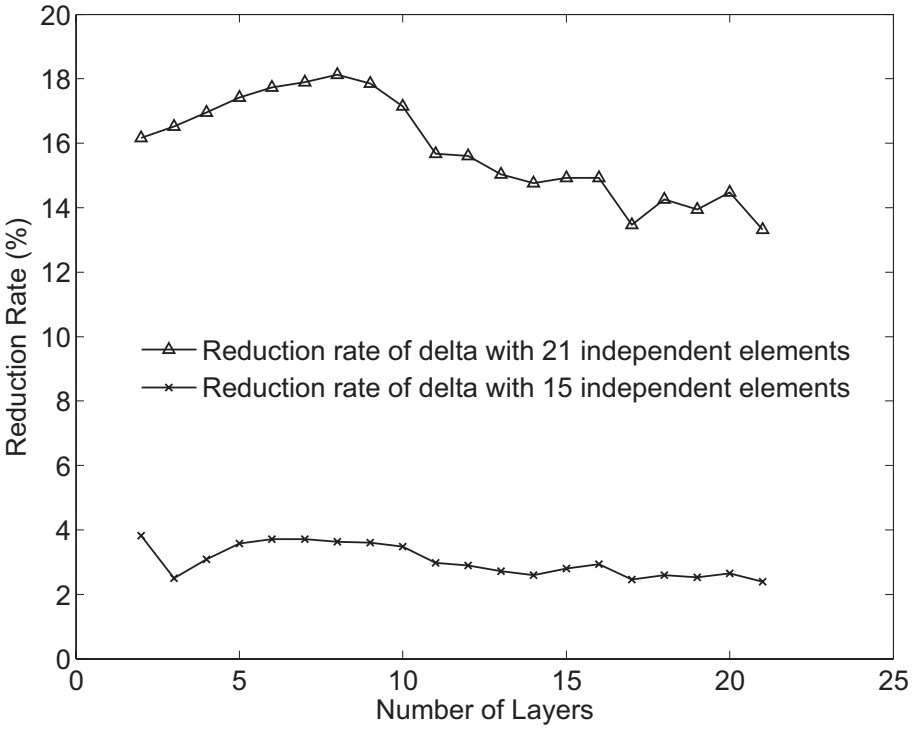

Figure 2.3: Comparison of the computational time by reduced delta matrix method T_R with those by the delta matrix method using 21 and 15 independent matrix elements T_{D21} and T_{D15}, respectively. Reduction rate of the computational time is defined as $(T_D - T_R)/T_D$.

CHAPTER III

Joint inversion of spatial autocorrelation curves with HVSR curves on the effect of Love wave contribution

3.1 Introduction

Constructing near surface velocity structures is a very important task for evaluating seismic hazard. In particular, an average S-wave velocity down to 30 m (Vs_{30}) is widely used for site classification. The direct measurement of S-wave velocities at boreholes gives a good estimation but it is expensive to estimate a large spatial distribution of S-wave velocity structures and it is difficult to apply it in an urban area.

As a non-destructive seismic method to estimate near surface S-wave velocity structures, much attention has been paid to the microtremor survey method in recent decades (e.g. *Okada*, 2003). Microtremors are passive seismic data excited by ambient noise from natural phenomena (e.g., winds and ocean waves) and human activities (e.g., traffic noise and industrial noise). The microtremor survey method usually extracts surface waves included in microtremors. S-wave velocity structures are then obtained by inversion of surface waves. As the array techniques to infer dispersion curves of surface waves, the spatial autocorrelation (SPAC) method (*Aki*,

1957, 1965) and frequency-wavenumber (*f-k*) analysis (*Capon*, 1969) are commonly used. Recently, *Cho et al.* (2004, 2006) developed the centerless circular array (CCA) method with miniature array by extending the SPAC method.

As a single station technique, the horizontal to vertical particle motion spectral ratio (HVSR) method originally proposed by *Nogoshi and Igarashi* (1971) and widely popularised by *Nakamura* (1989) uses a spectral ratio between vertical and horizontal components of microtremors. Although the origin of HVSR curves is a still controversial problem (e.g. *Bonnefoy-Claudet et al.*, 2008), HVSR curves can be interpreted as Rayleigh wave ellipticity on the assumption that surface waves are dominant in microtremors. *Fäh et al.* (2003) and *Arai and Tokimatsu* (2004) obtained S-wave velocity structures by inversion of HVSR curves using a prior information about S-wave velocities or thicknesses of sedimentary layers.

In order to obtain improved estimates of S-wave velocity structures, joint inversion of dispersion curves estimated by the array techniques and HVSR curves was proposed by *Scherbaum et al.* (2003). After that, a number of authors applied joint inversion (e.g. *Arai and Tokimatsu*, 2005; *Parolai et al.*, 2005; *Picozzi et al.*, 2005; *Hobiger et al.*, 2013). Most of them conclude that including HVSR curves in inversion constrains the depth or S-wave velocity of bedrock.

However, several unknown factors other than Rayleigh waves are included in HVSR curves observed in an actual wavefield. A Love wave contribution is usually neglected or assumed as constant values over frequencies (e.g. *Arai and Tokimatsu*, 2004; *Castellaro and Mulargia*, 2009). The energy proportion between Love and Rayleigh waves can be estimated by using the three-component SPAC method (*Aki*, 1957; *Köhler et al.*, 2007) or *f-k* method (*Poggi and Fäh*, 2010). *Hobiger et al.* (2009) also proposed the RayDec method to extract Rayleigh wave ellipticity based on the random decrement technique. Observations of the energy proportion revealed that it depends on not only frequencies (e.g. *Okada*, 2003; *Köhler et al.*, 2007; *Bonnefoy-*

Claudet et al., 2006a) but also time (*Endrun*, 2011).

Despite these observations, in some situations, we need to invert observed HVSR curves under some assumption regarding the Love waves contribution because applicable frequency ranges where the energy proportion of both Love and Rayleigh waves can be determined from the three-component SPAC method are restricted (*Bonnefoy-Claudet et al.*, 2008). The RayDec method also fails in reproducing Rayleigh wave ellipticity when vertical or horizontal component of Rayleigh waves vanishes (*Hobiger et al.*, 2009).

Moreover, the effect of body waves cannot be neglected for some combinations of impedance contrast and source positions (*Bonnefoy-Claudet et al.*, 2006a, 2008). Higher modes of surface waves also affect the shape of HVSR curves as studied by (*Arai and Tokimatsu*, 2004).

Due to above noise effects, absolute values of Rayleigh wave ellipticity are difficult to reproduce in some cases. For example, the result of joint inversion of dispersion curves with HVSR curves by *Hayashi et al.* (2011) shows that the absolute values of the observed HVSR curve are not consistent with the theoretical curve, although the shape of the HVSR curve is well retrieved. Therefore, in order to evaluate the shape of HVSR curves rather than the absolute values, *Zor et al.* (2010) prefer to use zero-lag crosscorrelations (ZLCC) in evaluating HVSR curves.

In this paper, we demonstrate the effectiveness of the joint inversion of the SPAC method with the HVSR method in which HVSR curves are evaluated by ZLCC. In addition, we investigate the effects of the assumption of the Love wave contribution and the weighting proportion between SPAC and HVSR curves. We apply the proposed inversion to field data acquired in the Newcastle city, Australia.

3.2 Method

3.2.1 SPAC method

The basic theory of the SPAC method can be summarized as follows (e.g. *Okada*, 2003; *Asten*, 2006). Suppose microtremors are obtained by a circle array with a radius x and surface waves of fundamental mode are dominant in microtremors. Then, the azimuthal average of complex coherencies between a central and a circumferential receiver goes to the Bessel function, referred to as SPAC curves (coefficients) ρ,

$$\rho(x, f) = J_0 \left[\frac{2\pi f}{c(f)} x \right], \tag{3.1}$$

where f is the frequency, c is the phase velocity, and J_0 is the Bessel function of the first kind of zero order. In the SPAC method, dispersion curves of Rayleigh waves can be estimated by fitting observed SPAC curves to the Bessel function for each x. The fitting procedure is extended by using all possible pairs of x referred to as the extended SPAC (ESPAC) method (*Ling and Okada*, 1993; *Ohori et al.*, 2002).

As proposed by *Asten et al.* (2004) and *Asten* (2006), however, observed SPAC curves can be directly compared with the theoretical curves. In this study, we prefer to use the direct fitting inversion of SPAC curves because it doesn't require the interpretation of phase velocities intrinsically and it can reduce bias caused by the conversion from SPAC curves to phase velocities. *Wathelet et al.* (2005) applied the direct fitting of SPAC curves by using neighborhood algorithm and *Ikeda et al.* (2012) also applied the direct fitting inversion including higher modes with genetic algorithm (GA). *Hobiger et al.* (2013) combined the direct fitting method of SPAC curves with HVSR curves as joint inversion.

3.2.2 HVSR method

Following *Arai and Tokimatsu* (2004), observed HVSR curves $(H/V)_{obs}$ considering Love and Rayleigh waves can be described as follows.

$$(H/V)_{obs}(f) = \sqrt{\frac{P_{HR}(f) + P_{HL}(f)}{P_{VR}(f)}}, \tag{3.2}$$

where P_{HR} is the horizontal-component power of Rayleigh waves, P_{VR} is the vertical-component power of Rayleigh waves and P_{HL} is the horizontal-component power of Love waves. Equation 3.2 can be expressed by using Rayleigh wave ellipticity $(H/V)_R$ and Rayleigh to Love wave amplitude ratio for horizontal motion β,

$$(H/V)_{obs}(f) = \sqrt{1 + \frac{1}{\beta^2}}(H/V)_R(f), \tag{3.3}$$

where

$$(H/V)_R(f) = \sqrt{\frac{P_{HR}(f)}{P_{VR}(f)}}, \tag{3.4}$$

$$\beta(f) = \sqrt{\frac{P_{HR}(f)}{P_{HL}(f)}}, \tag{3.5}$$

Assuming the value of β, theoretical HVSR curves corresponding observed curves (equation 3.2 or 3.3) can be computed by Rayleigh wave ellipticity. *Matsushima and Okada* (1990) and *Arai and Tokimatsu* (2000) indicated the value of the Rayleigh to Love wave amplitude ratio β is stable at in the range 0.4-1.0. Therefore, *Arai and Tokimatsu* (2004, 2005) assumed the value of β as 0.7 because it is an average between 0.4 and 1.0. To further investigate the effects of β in inversion, we apply firstly several constant values of β (0.4, 0.7 and 1.0) and secondly a frequency dependent β estimated by the three-component SPAC method.

3.2.3 Joint inversion scheme

In joint inversion of SPAC curves with HVSR curves, the misfit function for SPAC curves F_{SP} is defined as follows (*Wathelet et al.*, 2005);

$$F_{SP} = \sqrt{\frac{1}{\sum_{k=1}^{n_R} n_{Fk}} \sum_{i=1}^{n_R} \sum_{j=1}^{n_{F_i}} \frac{\{\rho_{obs}(x_i, f_j) - \rho_{theo}(x_i, f_j)\}^2}{\sigma_{ij}^2(x_i, f_j)}}, \tag{3.6}$$

where ρ_{obs} is the observed SPAC curve, ρ_{theo} is the theoretical SPAC curve, σ is the observed standard deviation, n_R is the number of receiver spacings and n_{F_i} is the number of frequency samples for receiver spacing i.

HVSR curves are usually evaluated by comparing absolute values of observed HVSR curves with theoretical curves (e.g. *Arai and Tokimatsu*, 2005; *Parolai et al.*, 2005; *Hobiger et al.*, 2013). *Scherbaum et al.* (2003) evaluate the shape of HVSR curves by using peak and trough frequencies. *Asten et al.* (2014) used both peak and trough frequencies plus qualitative shapes of HVSR curves . In this study, we employ ZLCC in log-scale proposed by *Zor et al.* (2010) to evaluate the shape of HVSR curves rather than absolute values. The misfit function for HVSR curves F_{HV} is defined by the inverse of ZLCC between observed and theoretical HVSR curves as follows;

$$F_{HV} = ZLCC^{-1}, \tag{3.7}$$

$$ZLCC = \frac{\sum_{i=1}^{N} log_{10}HV_{obs}(f_i) log_{10}HV_{theo}(f_i)}{\sqrt{\sum_{i=1}^{N} log_{10}HV_{obs}(f_i)^2 \sum_{i=1}^{N} log_{10}HV_{theo}(f_i)^2}}, \tag{3.8}$$

As the misfit function for joint inversion F, two misfit functions are combined by using a weighting coefficient w as follows;

$$F = wF_{SP} + (1 - w)F_{HV}. \tag{3.9}$$

Since the value of w is a matter of choice, we also investigate the effects of the choice of w as well as that of β.

In order to search a wide model space without the effect of initial models, we employ genetic algorithm (GA) (*Goldberg*, 1989; *Sen and Stoffa*, 1995) with elite selection and dynamic mutation (*Yamanaka and Ishida*, 1996) as an inversion method. When ZLCC takes negative values for poorly correlated data, the corresponding F_{HV} takes negative values. To avoid this problem, ZLCC with negative values are automatically replaced with very small positive values in GA inversion. Theoretical dispersion curves and a Rayleigh wave ellipticity are computed by the compound matrix method (*Saito*, 1988; *Saito and Kabasawa*, 1993; *Ikeda and Matsuoka*, 2013).

3.3 Application to field data

In this section, we apply the proposed joint inversion method to field data acquired during the 2012 Newcastle and Sydney SPAC surveys (*Asten et al.*, 2013; *Volti et al.*, 2013). Microtremor array measurements were conducted at 23 sites in the city of Newcastle and 2 sites in Sydney. The comprehensive results of the microtremor survey by the direct fitting of SPAC curves using GEOPSY software package (www.geopsy.org) and the software developed by *Asten* (2006) are summarized in *Volti et al.* (2013). *Asten et al.* (2013) also reported on uncertainties due to local sources from adjacent road traffic and the effectiveness of the combined use of both SPAC and HVSR methods to resolve bedrock using same dataset. We analyzed three dataset (BRD02, HAM03 and WIK01) acquired in the city of Newcastle.

3.3.1 Data processing

Each array station used a Kelunji Echo recorder with a single Lenartz LE-3Dlite 1 Hz 3-component seismometer as a receiver. The sampling rate was 100 Hz and the data length for each array was about 1 hour. Three-component microtremors are

observed by 2 types of triangle arrays using 7 seismometers (Figure 3.1). Figure 3.2 shows an example of set up on a single station.

First we generated 100 datasets from the observed microtremor data. Each dataset is about 30 sec with 30 % overlap and tapered with a 5 % cosine function. SPAC curves are computed by the average of 100 datasets for each receiver spacing x. SPAC curves derived from azimuthal averages of more than 3 pairs of coherencies are then used in the subsequent inversion. HVSR curves are computed by the average of estimated curves from 100 datasets from 3 component data for the central seismometer. Konno-Ohmachi smoothing functions with $b = 30$ for BRD02 and 40 for HAM03 and WIK01 (*Konno and Ohmachi*, 1998) were applied to observed HVSR curves.

3.3.2 BRD02

Figure 3.3 shows the observed SPAC curves and the HVSR curve for site BRD02 which used the triangle array described in Figure 3.1a. A sharp peak is observed in the HVSR curve at about 1.9 Hz indicating a strong velocity contrast between sedimentary layers and bedrock. The magenta line in Figure 3.3c is the set of values of β estimated by the three-component SPAC method. After we obtained the dispersion curve of Rayleigh waves by the ESPAC method from vertical component of microtremors, the values of β were estimated based on the method described in *Boxberger et al.* (2011). Values of β at frequencies below the peak of the HVSR curve cannot be extracted because Love and Rayleigh wave dispersion curves don't show reasonable values in this range. For the purpose of the inversion, the value of β at the lowest available frequency is assumed to apply at lower frequencies.

It can be seen that the observed SPAC curves at low frequencies don't have the shapes of the Bessel function. We can recognize two different reduction patterns of SPAC curves. One is the reduction of coherencies depending on receiver spacings. Generally, the longer receiver spacing is, the better coherencies can be estimated at

low frequencies. The other is the loss of coherencies below 1.9 Hz corresponding to the peak frequency of the HVSR curve, as pointed out by *Scherbaum et al.* (2003) and *Parolai et al.* (2005). Thus, the lowest useful frequencies of SPAC curves used in inversion are defined as the frequencies without any decrease of coherencies higher than 2.1 Hz. The highest frequency of SPAC curves used in inversion was determined where the phase velocities estimated by the ESPAC method show reasonable values. As the frequency range of the HVSR curve in inversion, both flanks of the peak frequency are used to give a better constrain the peak frequency (*Hobiger et al.*, 2013).

The next step is to estimate S-wave velocity structures by joint inversion of SPAC curves together with HVSR curves, using in turn three different constant values of β, and the frequency-variable value of β obtained as in the previous step. In inversion, 5-layer structures are assumed. Table 3.1 shows the search range of thicknesses and S-wave velocities for each layer. The S-wave velocity at an infinite half space was fixed as 2000 m/s. P-wave velocities and densities were determined from S-wave velocities by empirical equations (*Kitsunezaki et al.*, 1990; *Ludwig et al.*, 1970). The S-wave velocities and thickness for each layer are digitized as 7 bit binary strings. The number of the population and generations are 100 and 200, respectively. In order to avoid convergence dependent on initial populations, we carried out 6 trials with randomly seeded initial populations.

Figure 3.4 shows the minimum misfit functions of SPAC and HVSR curves for different values of β and w. The values of ZLCC are also described in Figure 3.4b. By including HVSR curves in the joint inversion, we observe a clear improvement of the values of F_{HV} and ZLCC for values $w \leq 0.7$. We have determined $w = 0.5$ as the optimal value for BRD02 because it keeps enough weighting for both misfit functions. It should be noted that the misfit functions are less dependent on the values of β.

Figure 3.5 shows the inverted velocity models for $w = 1.0$ and $w = 0.5$ with

β = 1.0, 0.7 and 0.4 and frequency-dependent, respectively. Color indicates the differences from the minimum misfit function. When only SPAC curves are considered in inversion (Figure 3.5a), there is an ambiguity in inverting velocity contrast at near 20 m. Moreover, there is no indication of bedrock because of a lack of SPAC curves at low frequencies. On the other hand, including HVSR curves in joint inversion generates clear velocity contrasts at about 23 m (Figures 3.5b-e) the depth of which is consistent with the result of the seismic cone penetrometer (SCPT) (*Volti et al.*, 2013). Although the S-wave velocities for the 3rd layer (from about 20 to 30 m) is not well constrained and differs in the value of β, the existence of high S-wave velocity layers at depths deeper than 35 m is suggested by joint inversion.

We prefer to describe an ensemble of accepted models (within 5 % for the velocity model with the minimum misfit function) but velocity models with minimum misfit functions are also analyzed. Figure 3.6 shows the comparison of observed SPAC and HVSR curves with theoretical curves for velocity models with the minimum misfit values (magenta lines in Figure 3.5). Although the theoretical HVSR curve is poorly resolved when only SPAC curves are considered in inversion, the peak position and the shape of HVSR curves are well retrieved by including HVSR curves in joint inversion (Figure 3.6c).

The observed SPAC curves broadly agree with theoretical curves for all cases. At low frequencies, however, the observed SPAC curve for x = 99.9 m is more consistent with theoretical SPAC curves obtained by joint inversion than when only SPAC curves are considered (Figure 3.6b). The opposite result is observed for the SPAC curve corresponding to x = 68.0 m (Figure 3.6a). It is considered that at low frequencies, the theoretical SPAC curves by joint inversion are more reasonable because SPAC curves with longer receiver spacings are more stable at lower frequencies. It should be emphasized that the results of joint inversion are relatively insensitive to the values of β.

3.3.3 HAM03

The results for HAM03 are similar to those for BRD02 and are summarized in the appendix D.

3.3.4 WIK01

Figure 3.7 shows the observed SPAC and HVSR curves and the estimated values of β obtained by the three-component SPAC method for site WIK01. The triangle array described in Figure 3.1a was used. The observed HVSR curve has a peak at 1.35 Hz. The observed SPAC curves slightly decrease near the peak frequency of the HVSR curve. In contrast to the results for BRD02 and HAM03, however, SPAC curves show good coherencies down to about 0.65 Hz which is well below the peak frequency of the HVSR curve. Therefore, the lowest frequencies of SPAC curves used in the inversion are determined to be 0.65 Hz. The estimated values of β at low frequencies are larger than those for BRD02 and HAM03.

As a second step we applied joint inversion for different values of β and w. Table 3.2 shows the search range of model parameters for WIK01. ZLCC are significantly improved when values $w \leq 0.5$ are used in joint inversion (Figure 3.8). In contrast to the case when the weighting value $w = 1.0$, the misfit functions for SPAC curves show about 40 % increase when using values $w \leq 0.5$, indicating the discrepancy between inverting SPAC and HVSR curves .

Figure 3.9 shows the velocity models obtained from joint inversion. Inverted velocity models by considering only SPAC curves, show ambiguity in estimating velocity contrasts at depths from 30 to 40 m (Figure 3.9a). However, S-wave velocities at deeper depths are well constrained without the use of the HVSR curve because the lowest frequency of SPAC curves used in the inversion is enough to constrain deeper velocity structures. Inclusion of HVSR curves in joint inversion generates apparent velocity contrasts at about 31 m, which is consistent with the result of SCPT (*Volti*

et al., 2013). When we consider only SPAC curves, there is no indication of the existence of high S-wave velocity layers. However, the results of joint inversion indicate existing transition layers at depths from 30 to 50 m and high S-wave velocity layers at depth deeper than 50 m.

Figure 3.10 shows the comparison of theoretical SPAC and HVSR curves with the observed curves. Theoretical SPAC curves at higher than 2.0 Hz are consistent with observed curves. Theoretical SPAC curves for $w = 1.0$ are more consistent with the observed values below 2.0 Hz, whereas the observed HVSR curve are well retrieved by joint inversion.

3.4 Discussion

3.4.1 Exclusion of SPAC curves at low frequencies in inversions

For WIK01, we have observed the discrepancy between inverting SPAC curves below the peak frequency of the HVSR curve and HVSR curves. The observed SPAC curves show small decreases of coherencies at near the peak frequency of the HVSR curve. These decreases might be caused by low amplitudes of vertical component of microtremors at the peak of the HVSR curve. To overcome this problem, we exclude observed SPAC data below 1.6 Hz. We also note that use of β estimated by the three-component SPAC method is restricted to frequencies above 1.6 Hz. Below 1.6 Hz, we assume a constant value $\beta = 0.5$.

Figure 3.11 shows the misfit functions for WIK01 when we remove SPAC curves at low frequencies. For values $w \leq 0.7$, ZLCC take high values above 0.95 indicating convergence of inverting HVSR curves. In this case, increments of the misfit functions of SPAC curves are about 15 % compared to the case when the weighting value w =1.0.

When only SPAC curves are considered in the inversion (Figure 3.12a), an ambi-

guity of inverting S-wave velocities at depths deeper than 30 m is increased because the lowest frequencies of SPAC curves are higher than those without the removal of SPAC curves (Figure 3.9a). The strong velocity contrasts at about 33 m are well emphasized in this case. The thick transition layers in Figure 3.9 might be artificial ones because they become thinner in inverted models whereas the S-wave velocities for the 3rd layer differs in the value of β.

Figure 3.13 shows the comparison of the observed SPAC and HVSR curves with the theoretical curves. By excluding low frequency data, the difference between theoretical SPAC curves for $w = 1.0$ and those for joint inversion can be interpreted as not just a discrepancy between inverting SPAC and HVSR curves but low coherencies of SPAC curves depending on receiver spacing as in BRD02 (Figure 3.6) because the observed SPAC curve with longer receiver spacing ($x = 99.9$ m) is consistent with theoretical curves from joint inversion at low frequencies.

From these examples we recommend exclusion of SPAC data when there is a discrepancy between SPAC curves at low frequencies below a peak frequency of a HVSR curve, and the corresponding HVSR curves.

3.4.2 Joint inversion using absolute values of HVSR

In order to investigate advantages of the use of ZLCC in evaluating HVSR curves in joint inversion, we also applied joint inversion of SPAC curves with HVSR curves, in which fitted HVSR curves are evaluated by root mean squares error (RMSE) computed on logarithmic scales. This is an approach similar to that of *Hobiger et al.* (2013) who used a neighborhood algorithm for the inversion. Here, we focus on the difference of misfit functions depending on the choice of β and w.

Figures 3.14 and 3.15 show the misfit functions of joint inversion using RMSE for BRD02 and WIK01, respectively. For WIK01, we used excluded SPAC curves below 1.6 Hz. For values $w \leq 0.9$ for BRD02, and $w \leq 0.7$ for WIK01, the misfit

functions for HVSR curves are significantly improved. However, when the values of β are 1.0, applying further smaller values of w makes the misfit functions for SPAC curves considerably worse. This result indicates that finding optimal values of w is difficult when larger values of β (e.g., 1.0) are applied with the use of RMSE in evaluating HVSR curves compared to the case with the use of ZLCC (Figures 3.4 and 3.11).

3.4.3 Bias of ESPAC method

We demonstrate a bias introduced by the intermediate step of conversion from SPAC curves to phase velocities prior to inversion, by comparing dispersion curves estimated by the ESPAC method with the theoretical dispersion curves for the previous above inversion. Theoretical dispersion curves for velocity models with minimum misfit functions when $w = 1.0$ and $w = 0.5$ and the values of β estimated from the three-component SPAC method are used.

Figure 3.16 shows the result of BRD02 and WIK01 with the removal of SPAC curves at low frequencies. The estimated phase velocities by the ESPAC method agree with theoretical ones when only SPAC curves are considered in inversion ($w = 1.0$) for both sites. As long as we compare the results in phase velocity domain, the mismatches between observed phase velocities and theoretical ones by joint inversion are considered as a discrepancy between observed phase velocities and HVSR curves. However, if we compare observed data in SPAC curves as in Figures 3.6a and b or Figures 3.13a and b, we notice that low coherencies depending on receiver spacings also have an effect on these mismatches. Since SPAC curves for vertical component data also take low values near the peak of HVSR curves, careful comparison of observed SPAC and HVSR curves with inverted values are recommended to avoid the bias introduced SPAC data at low frequencies.

3.5 Conclusions

In this paper, we investigated the effect of Love wave contribution in joint inversion of SPAC and HVSR curves to construct S-wave velocities down to bedrock. We used ZLCC as the misfit function of HVSR curves to assists in minimizing the noise effect of wave modes other than Rayleigh waves.

We have applied the proposed joint inversion for field data acquired at Newcastle, Australia. For some data sets a two-step process is possible whereby firstly the frequency-dependent values of Rayleigh to Love wave contribution β are extracted from the three-component SPAC method, with subsequent joint inversion of SPAC and HVSR data. However, the frequency ranges of estimated β are generally restricted to frequencies above the peak frequency of the HVSR curves. An added limitation of this approach is that the use of three-component seismometers might be difficult in some conditions. We have therefore evaluated the joint inversion method using assumed constant values of β.

Inclusion of HVSR curves in joint inversion provides some level of constraint on estimates of the depth of velocity contrasts between sedimentary layers and high S-wave velocity layers in the basement. Results are robust with respect to the choice of β so a priori knowledge of β, or successful extraction of a frequency-dependent β from preliminary ESPAC analysis, does not have a significant influence on the depth of velocity contrasts in the joint inversion outcome. However, the velocity contrasts between sedimentary layers and basements are not well constrained by the joint inversion and differ for differing choices of β.

When there is a discrepancy between observed and modelled SPAC curves at frequencies below the peak frequency of HVSR curves (e.g., WIK01), it is worth excluding SPAC data at low frequencies because they are unstable near the peak of HVSR curves at some conditions. In such a situation the observed HVSR curve provides the necessary low-frequency data for a successful joint inversion. We find

that when ZLCC is used in joint inversion, the misfit functions for SPAC curves are less affected by the choice of the values of β, compared to the case when RMSE are used in evaluating HVSR curves. To further investigate the advantage of ZLCC, additional quantitative studies using synthetic-noise microtremors will be necessary.

We also demonstrated existence of a bias caused by conversion of SPAC curves to phase velocities by the ESPAC method, especially evident at low frequencies. This bias has the potential to significantly affect construction of S-wave velocities and depth at or near bedrock in the inversion process. Comparison of observed SPAC curves with theoretical SPAC curves assists in recognition if such bias occurs.

Table 3.1: Search range of thickness and S-wave velocity in the joint inversion for BRD02 and HAM03.

Layer No.	$Thickness_{min}(m)$	$Thickness_{max}(m)$	$Vs_{min}(m/s)$	$Vs_{max}(m/s)$
1	5	15	100	250
2	5	25	150	300
3	5	30	300	1000
4	20	100	500	2000
5	∞	∞	2000	2000

Table 3.2: Search range of thickness and S-wave velocity in the joint inversion for WIK01.

Layer No.	$Thickness_{min}(m)$	$Thickness_{max}(m)$	$Vs_{min}(m/s)$	$Vs_{max}(m/s)$
1	5	20	100	250
2	5	30	150	300
3	5	50	350	1000
4	30	150	400	2000
5	∞	∞	2000	2000

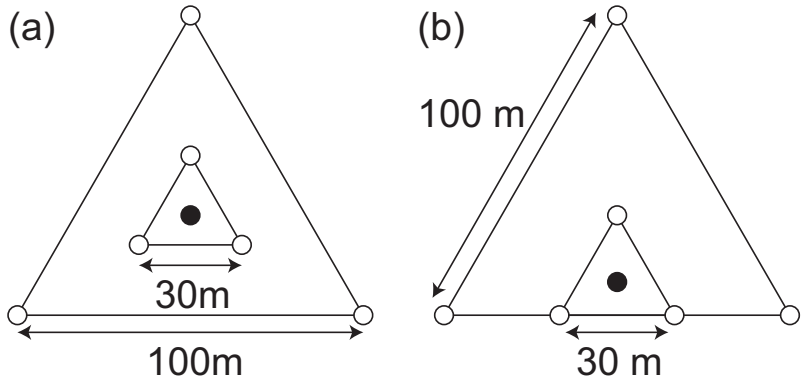

Figure 3.1: Array shapes used in the survey for (a) BRD02 and WIK01 and (b) HAM03. Black circles are central receivers used for computing HVSR curves.

Figure 3.2: Set up on a single station. The three-component seismometer is covered with the bucket.

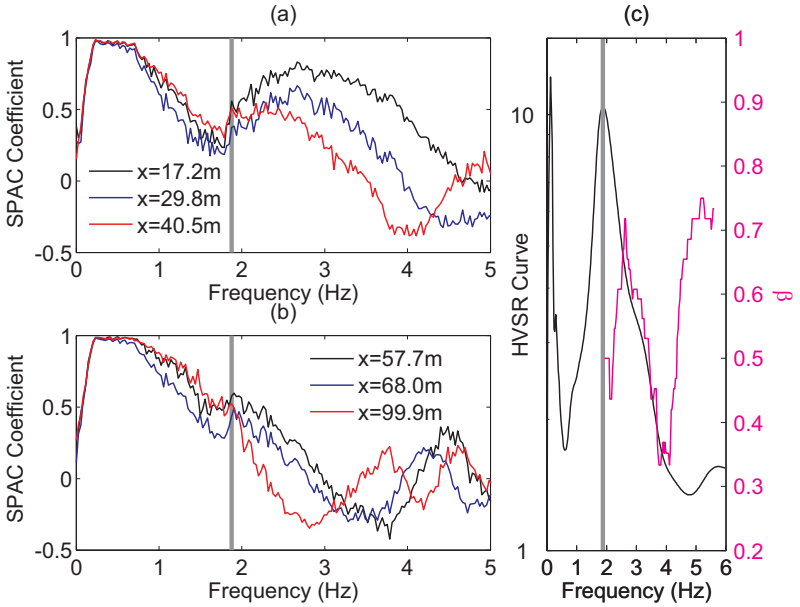

Figure 3.3: The observed SPAC curves for BRD02 corresponding to (a) $x = 17.2$, 29.8 and 40.5 m and (b) $x = 57.7$, 68.0 and 99.9 m. (c) The observed HVSR curve for BRD02. Gray lines are the peak frequency of the observed HVSR curve. The magenta line is the values of β estimated by the three-component SPAC method.

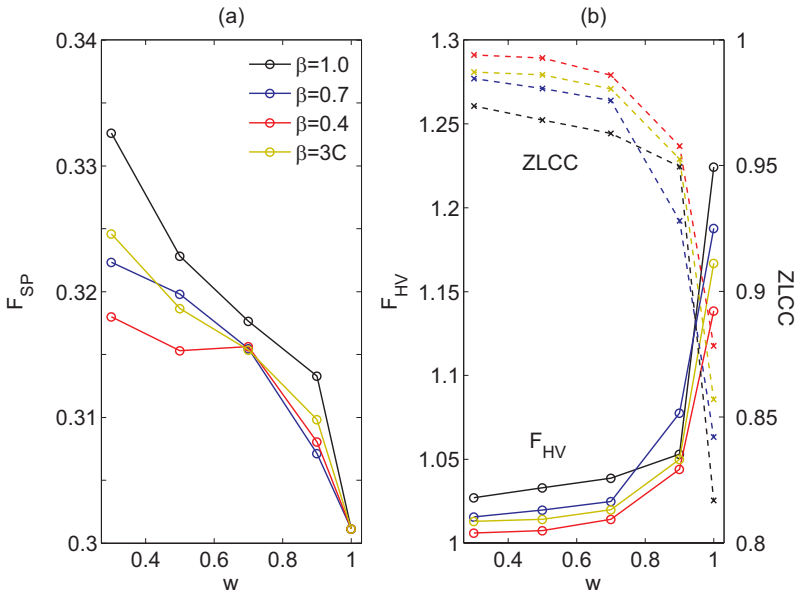

Figure 3.4: Misfit functions for (a) SPAC curves and (b) HVSR curves corresponding to BRD02. ZLCC are also described as dashed lines. 3C means the case when the values of β are estimated from the three-component method refer Figure 3.3c.

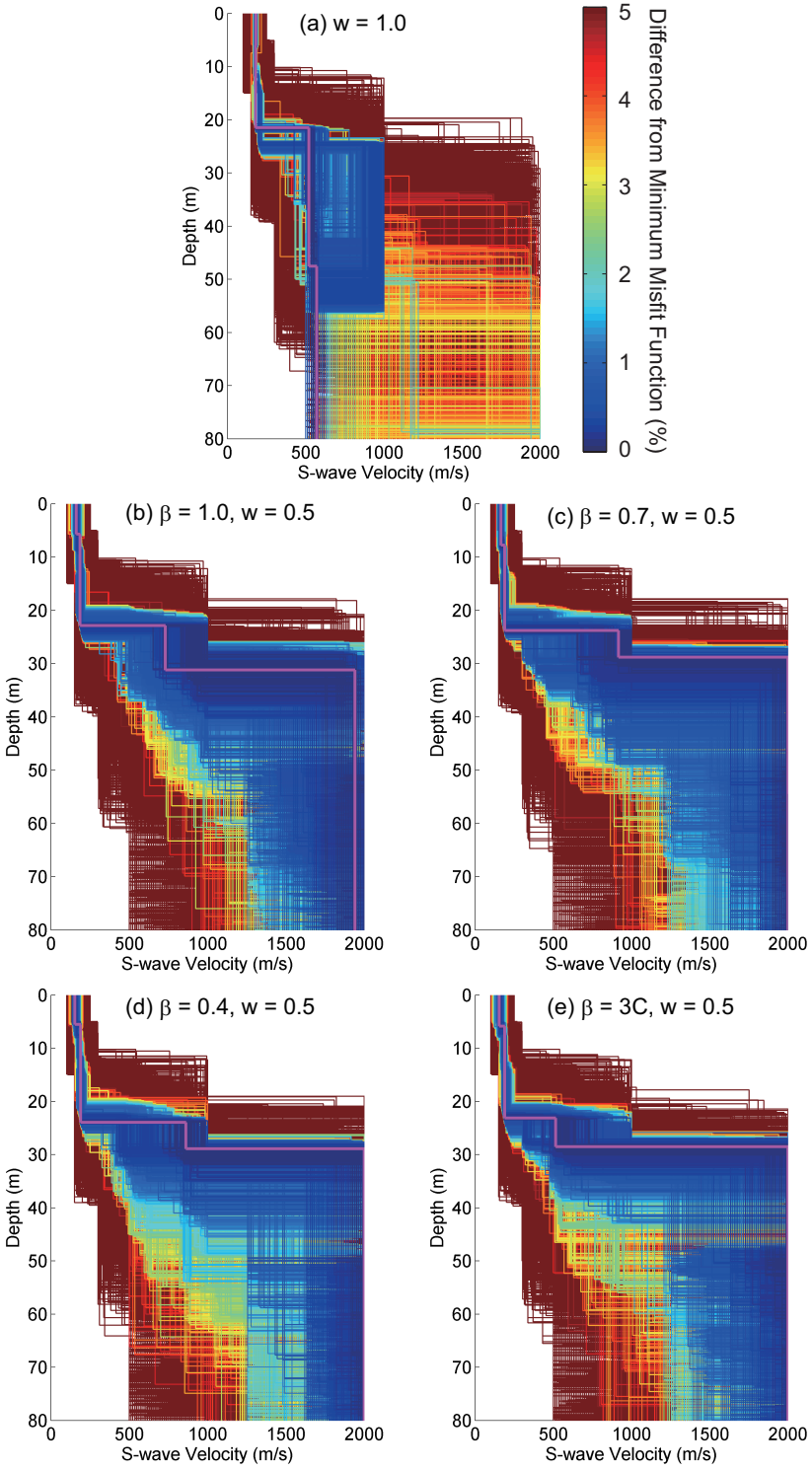

Figure 3.5: Inverted velocity models by joint inversion for BRD02 when (a) $w = 1.0$, (b) (e) $w = 0.5$ with $\beta = 1.0$, 0.7, 0.4 and 3C, respectively. Magenta lines are the velocity models with minimum misfit functions for each inversion.

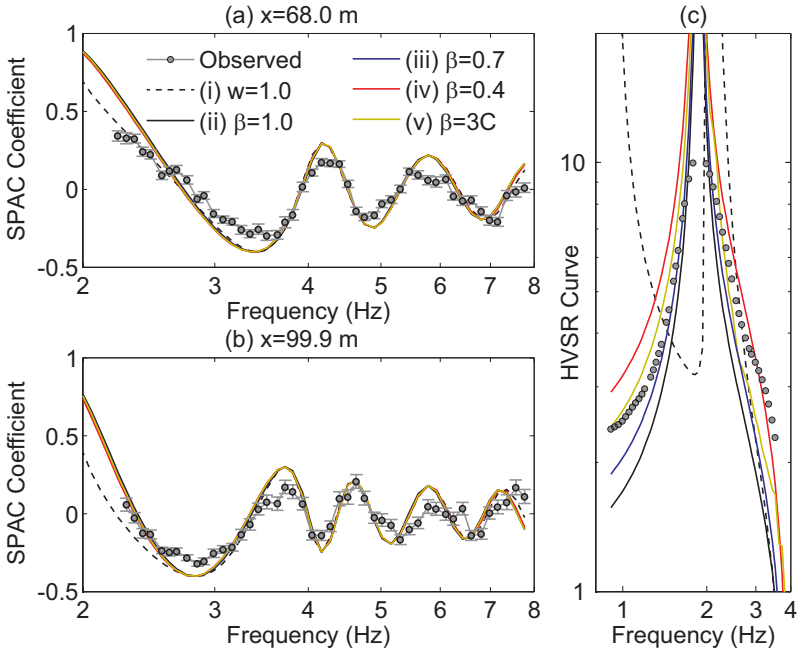

Figure 3.6: Comparison of theoretical SPAC curves for the inverted velocity models with minimum misfit functions corresponding to (a) $x = 68.0$ and (b) 99.9 m and (c) HVSR curves with observed curves for BRD02 when (i) $w = 1.0$, (ii)-(v) $w = 0.5$ with $\beta = 1.0$, 0.7, 0.4 and 3C, respectively. Standard errors of SPAC curves are described in (a) and (b).

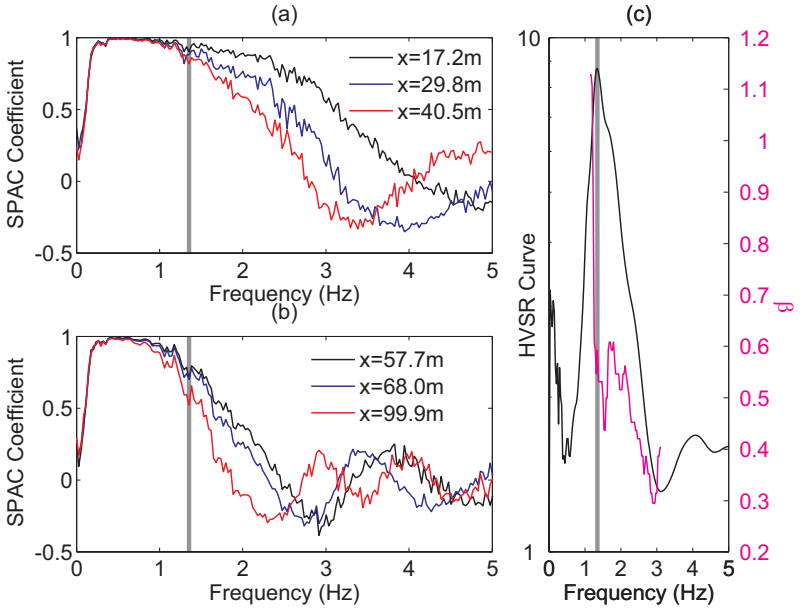

Figure 3.7: The observed SPAC curves for WIK01 corresponding to (a) $x = 17.2$, 29.8 and 40.5 m and (b) $x = 57.7$, 68.0 and 99.9 m. (c) The observed HVSR curve for WIK01. Gray lines are the peak frequency of the observed HVSR curve. The magenta line is the values of β estimated by the three-component SPAC method.

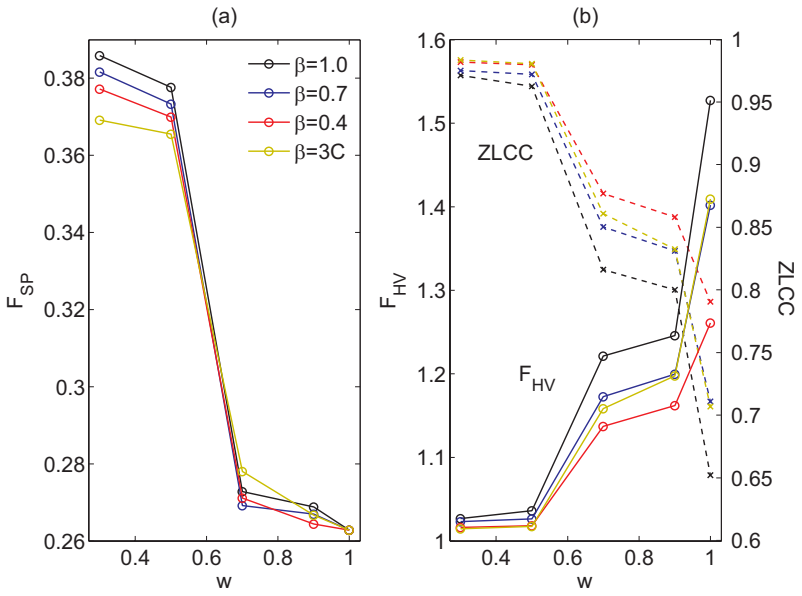

Figure 3.8: Misfit functions for (a) SPAC curves and (b) HVSR curves corresponding to WIK01. ZLCC are also described as dashed lines.

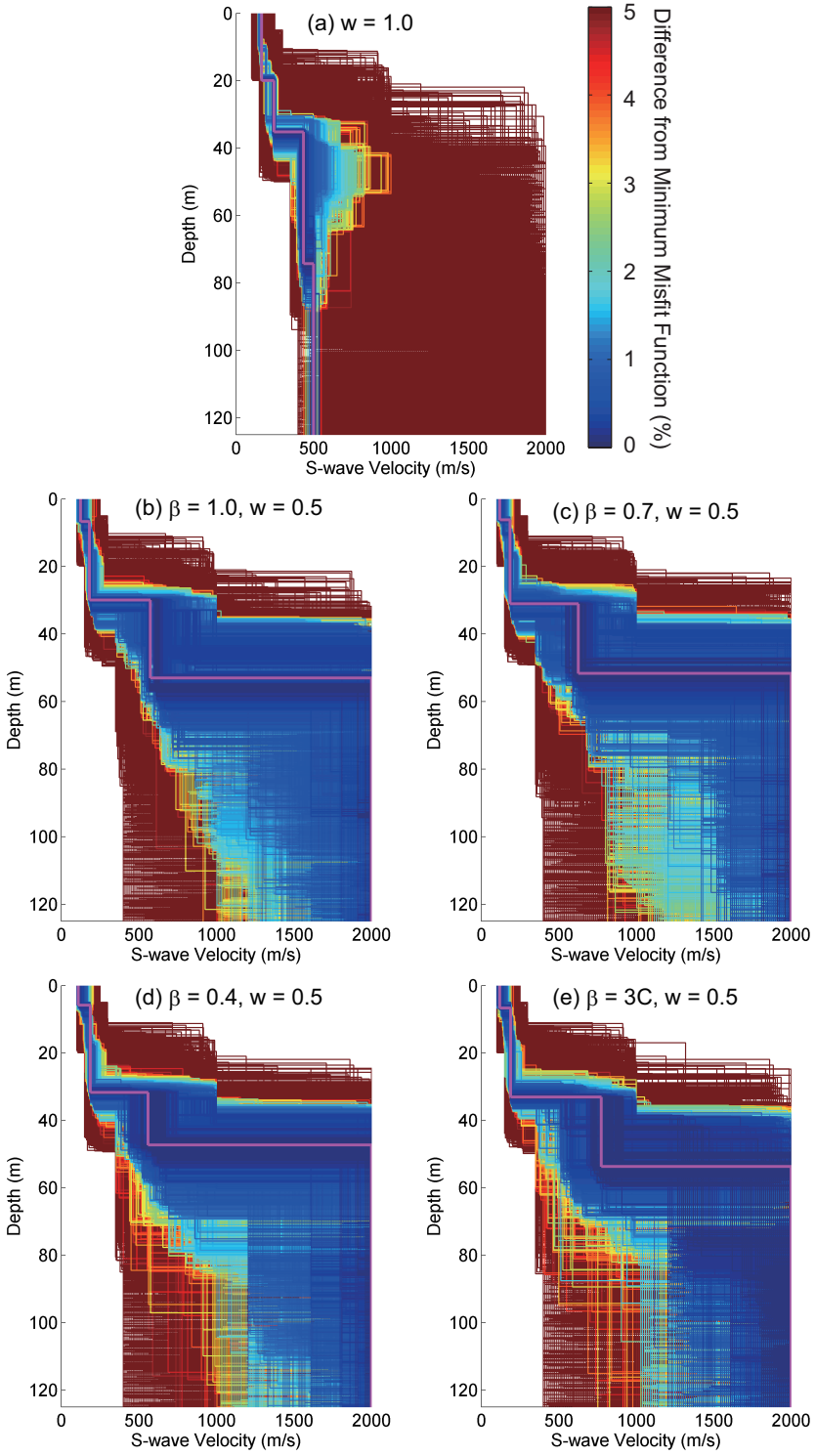

Figure 3.9: Inverted velocity models by joint inversion for WIK01 when (a) $w = 1.0$, (b)-(e) $w = 0.5$ with $\beta = 1.0$, 0.7, 0.4 and 3C, respectively. Magenta lines are the velocity models with minimum misfit functions for each inversion.

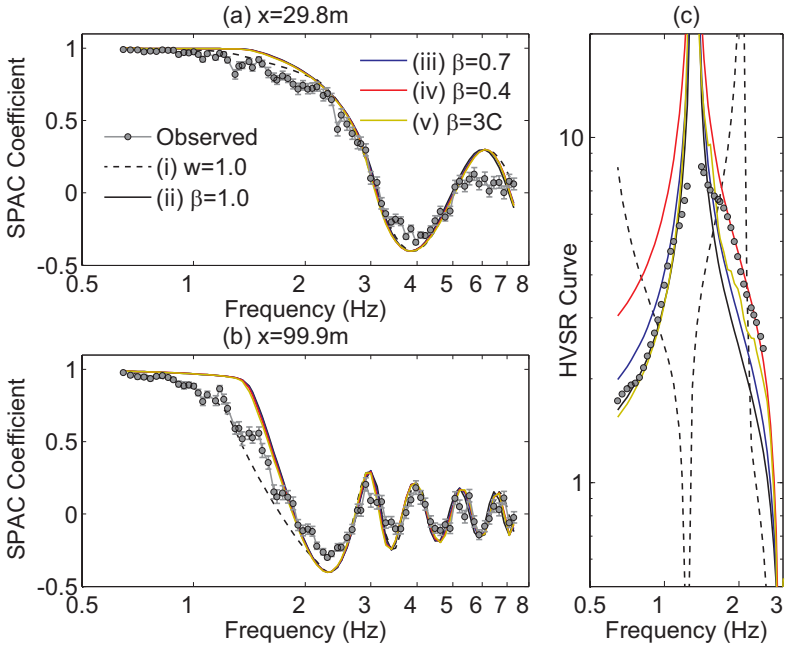

Figure 3.10: Comparison of theoretical SPAC curves for the inverted velocity models with minimum misfit functions corresponding to (a) $x = 29.8$ and (b) 99.9 m and (c) HVSR curves with observed curves for WIK01 when (i) $w = 1.0$, (ii)-(v) $w = 0.5$ with $\beta = 1.0$, 0.7, 0.4 and 3C, respectively. Standard errors of SPAC curves are described in (a) and (b).

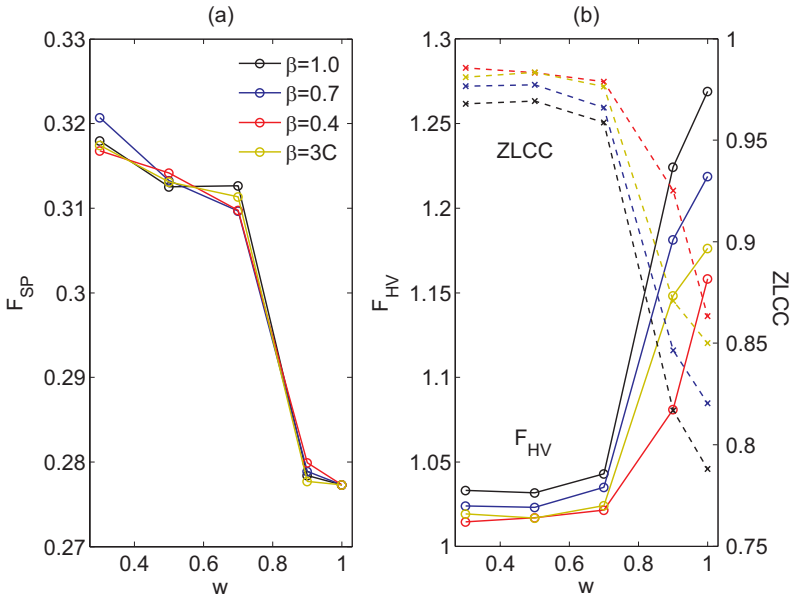

Figure 3.11: Misfit functions for (a) SPAC curves and (b) HVSR curves corresponding to WIK01 with the exclusion of SPAC data at low frequencies <1.6 Hz. ZLCC are also described as dashed lines.

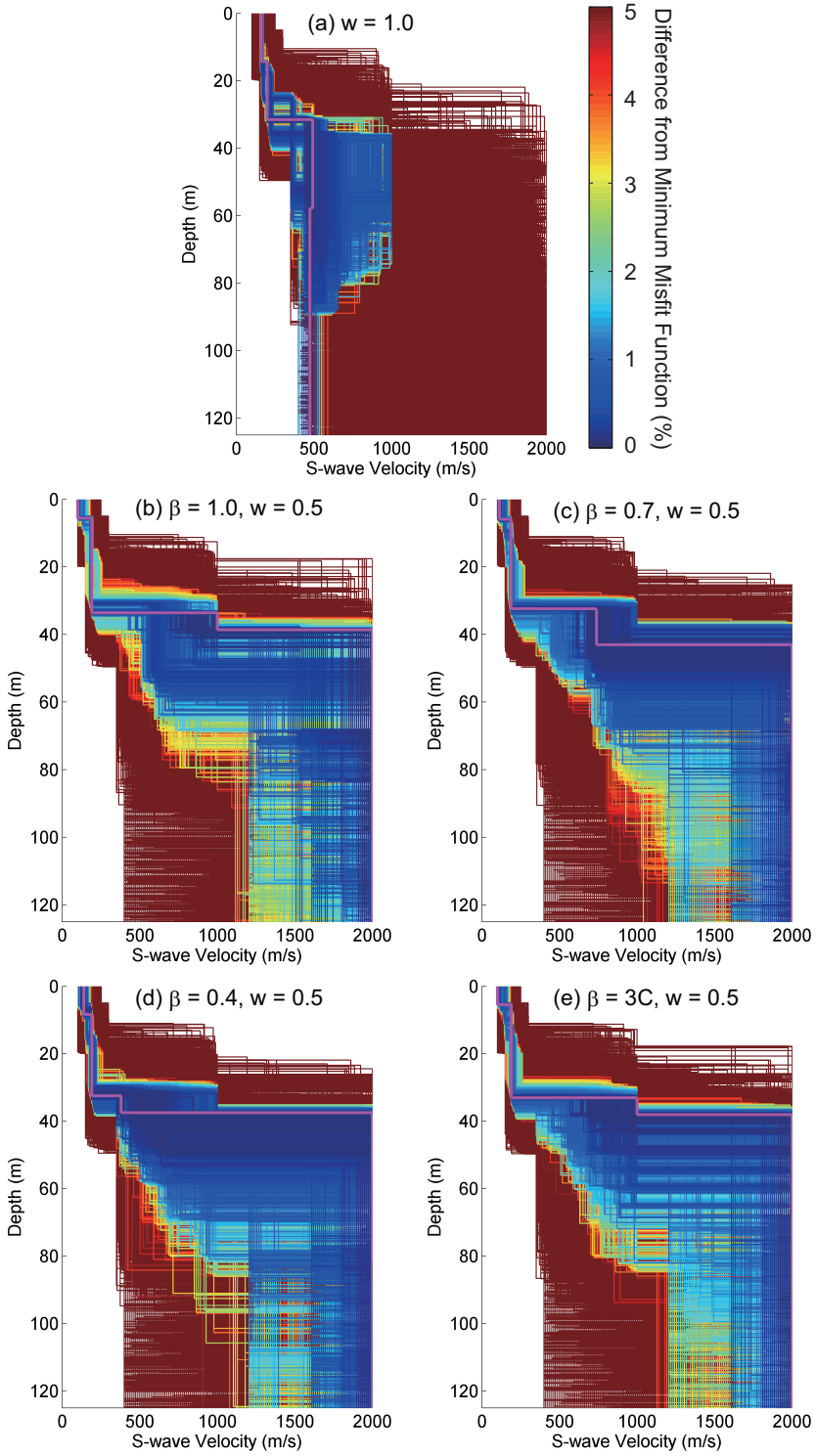

Figure 3.12: Inverted velocity models by joint inversion for WIK01 with the exclusion of SPAC data at low frequencies <1.6 Hz when (a) $w = 1.0$, (b)-(e) $w = 0.5$ with $\beta = 1.0$, 0.7, 0.4 and 3C, respectively. Magenta lines are the velocity models with minimum misfit functions for each inversion.

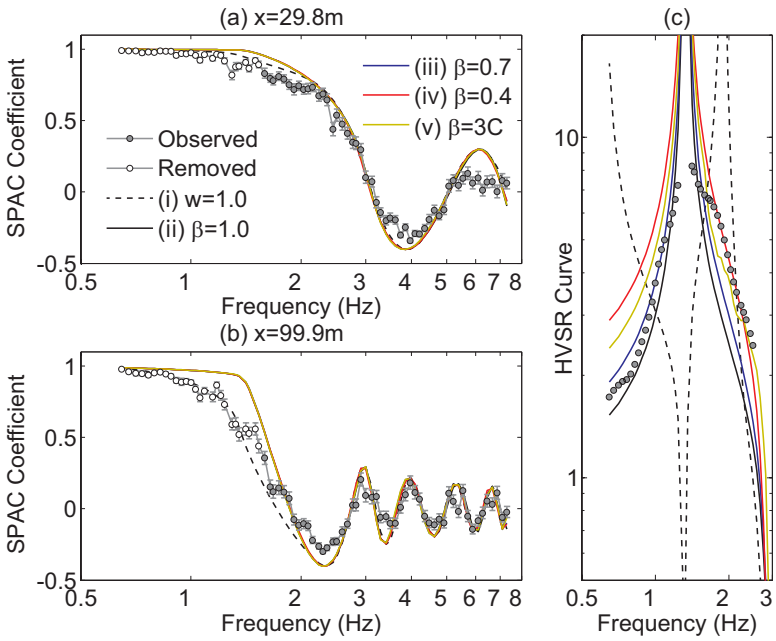

Figure 3.13: Comparison of theoretical SPAC curves for the inverted velocity models with minimum misfit functions corresponding to (a) $x = 29.8$ and (b) 99.9 m and (c) HVSR curves with observed curves for WIK01 with the exclusion of SPAC data at low frequencies <1.6 Hz when (i) $w = 1.0$, (ii)-(v) $w = 0.5$ with $\beta = 1.0$, 0.7, 0.4 and 3C, respectively. Standard errors of SPAC curves are described in (a) and (b).

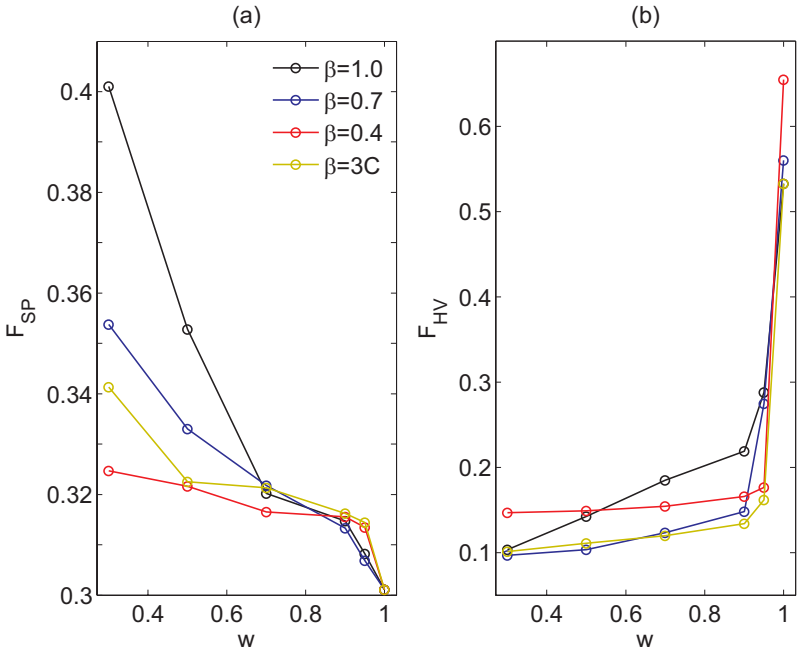

Figure 3.14: Misfit functions for (a) SPAC curves and (b) HVSR curves corresponding to BRD02 when RMSE are used in evaluating HVSR curves.

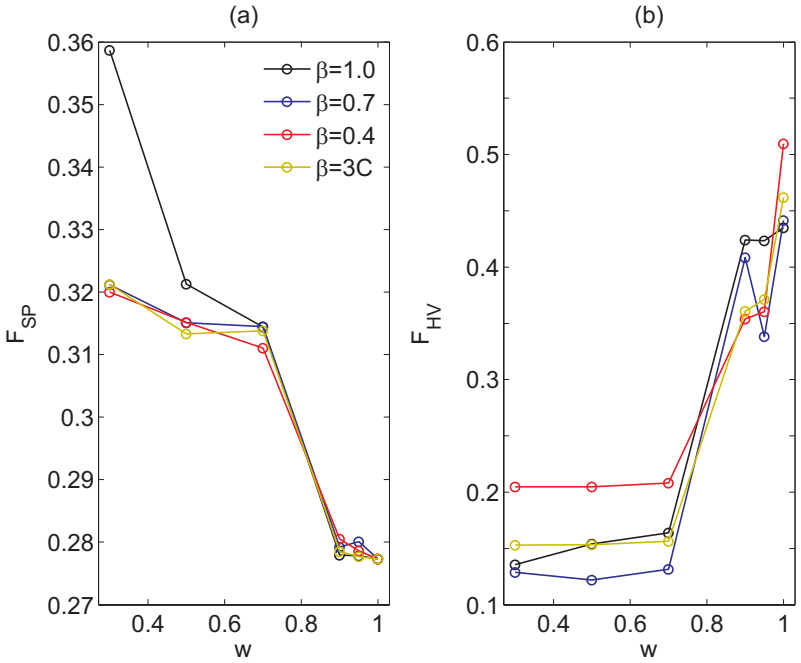

Figure 3.15: Misfit functions for (a) SPAC curves and (b) HVSR curves corresponding to WIK01 with the exclusion of SPAC data at low frequencies <1.6 Hz when RMSE are used in evaluating HVSR curves.

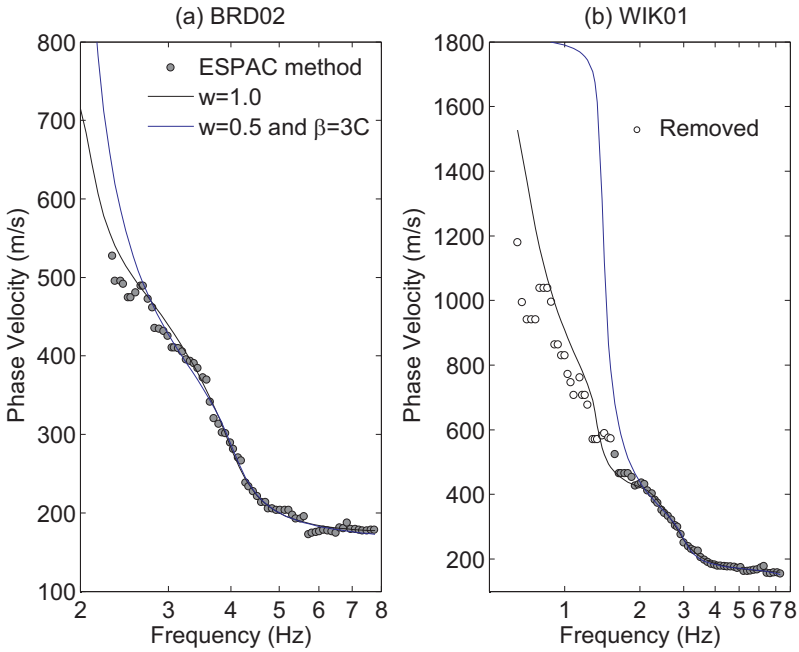

Figure 3.16: Comparison of dispersion curves estimated by the ESPAC method with theoretical dispersion curves by joint inversion when $w = 1.0$ and $w = 0.5$ with $\beta = 3$C for (a) BRD02 and (b) WIK01 with the removal of SPAC curves at low frequencies.

CHAPTER IV

Multimode inversion with amplitude response of surface waves in the spatial autocorrelation method

4.1 Introduction

The microtremor method (*Okada*, 2003) has been applied to the estimation of S-wave velocity structures by using surface waves (e.g. *Okada*, 2003; *Bonnefoy-Claudet et al.*, 2006b). The method has been used mainly for geotechnical site characterization (e.g. *Tokimatsu*, 1997; *Roberts and Asten*, 2004; *Richwalski et al.*, 2007). Since the method is non-destructive and needs no active sources, it is inexpensive and easy to apply in various environments. The spatial autocorrelation (SPAC) method (*Aki*, 1957, 1965) and the frequency-wavenumber (f-k) method (*Capon*, 1969) are the two main approaches for estimating the dispersion curves of surface waves from microtremor data. Recently, *Cho et al.* (2004, 2006) developed the centerless circular array (CCA) method which uses a miniature circular array. Analysis using refraction microtremors (ReMi) (*Louie*, 2001) and time domain analysis (*Chávez-García and Luzón*, 2005) has also been proposed. In this paper, we focus on the SPAC method, whose effectiveness has been demonstrated at various sites, and discuss how to perform a stable inversion with higher modes of surface waves included in microtremors.

The SPAC method can extract the phase velocities of surface waves from microtremor array observations. The S-wave velocity structure is then estimated from an inversion of the phase velocities. Surface waves have different modes of propagation. The mode which has lowest velocity is called fundamental mode, whereas the modes which propagate faster than the fundamental mode are called higher modes. Higher modes play an important role if a stiff layer overlies a soft layer or is embedded in soft layers (*Gucunski and Woods*, 1992; *Tokimatsu et al.*, 1992b). *Xia et al.* (2003) showed that consideration of higher modes improves the resolution of the inversion and makes its sensitivity deep. However, observed microtremors have been analyzed on the assumption that the fundamental component is predominant in the SPAC method, although some studies have shown that the effect of higher modes included in microtremors is not negligible (e.g. *Tokimatsu*, 1997; *Ohori et al.*, 2002; *Foti*, 2005; *Feng et al.*, 2005; *Asten and Roberts*, 2006). If higher modes of surface waves are predominant in the observed microtremors, analysis without any considerations of higher modes would make it difficult to determine a unique velocity model. Thus, a method that considers higher modes in the SPAC method is required.

Aki (1957) proposed an implementation of the SPAC method when a wave is composed of partial waves with different phase velocities. The proposal regards observed spatial autocorrelation (SPAC) coefficients as a superposition of each mode component weighted by its power fraction. By applying this idea to higher modes, several multi-mode analysis methods in the SPAC method have been proposed. *Asten* (1976, 2001) proposed an analysis method that separates each mode component by solving the phase velocities and energy fractions of the two modes from the observed data. *Asten et al.* (2004) and *Asten and Roberts* (2006) also proposed a method to recognize higher modes in direct-fitting method of SPAC coefficients (*Asten et al.*, 2002, 2004), which is called multi-mode SPAC (MMSPAC). *Asten and Roberts* (2006) demonstrated the effectiveness of MMSPAC, although they failed to identify higher

mode propagation in a simulated data analysis.

Another multi-mode analysis method was proposed by *Tokimatsu et al.* (1992a,b); *Tokimatsu* (1997). If the phase velocities of each mode cannot be separated, the observed phase velocities may not be explained by only one mode. These velocities are called apparent or effective velocities (*Socco et al.*, 2010) or fallacious estimates of phase velocities (*Yokoi*, 2010). The approach is to evaluate numerically the theoretical effective phase velocities corresponding to the observed ones by using the energy fractions of each mode from the amplitude response (*Harkrider*, 1964, 1970) using a given subsurface model. For inversion, this evaluated effective phase velocities are compared with corresponding to the observed phase velocities. This multi-mode method is superior to the former one in that the phase velocities and energy fractions of each mode do not have to be extracted from the observed microtremors, which makes it easier to increase the number of modes in an inversion. Furthermore, this advantage contributes to the avoidance of mode misidentification, which sometimes causes notable error in the results (e.g. *Zhang and Chan*, 2003; *O'Neill and Matsuoka*, 2005). *Ohori et al.* (2002) and *Obuchi et al.* (2004) applied this approach to the SPAC method and performed a successful analysis. In addition, *Yokoi* (2010) derived the power partition ratio of each mode in the SPAC and CCA methods by using the theory of seismic interferometry, and showed better inversion performance with dual-mode inversion than with single mode.

When higher modes are considered, the effective phase velocities are functions of the receiver separation distance in addition to the frequency, whereas the phase velocities of each mode are functions only of the frequency. This implies that the effect of the receiver separation distance has to be considered when applying the extended spatial autocorrelation (ESPAC) method (*Ling and Okada*, 1993; *Okada*, 2003), which is more robust than the SPAC method and determines a phase velocity from the observed SPAC coefficients obtained from all possible pairs of receivers. However,

a method for analyzing the theoretical effective phase velocities corresponding to the ones estimated by the ESPAC method has not yet been established. Moreover, multi-mode analysis using amplitude response has not been applied to the direct-fitting method of SPAC coefficients. As we will discuss later, multi-mode analysis using amplitude response in the direct-fitting method is much simpler than in the ESPAC method.

In this paper, we propose two analysis methods that consider the effect of higher modes and multiple receiver separation distances in the SPAC method using amplitude response. One is to calculate the theoretical effective phase velocities corresponding to the observed phase velocities from the ESPAC method. The other is to compare the observed SPAC coefficients with theoretical ones by a receiver separation distance when considering higher modes. We first simulated microtremors with a model in which higher modes predominate to conduct a quantitative evaluation of the proposed methods. We compared the observed dispersion curve and SPAC coefficients with theoretical ones. Then we estimated S-wave velocity models by inversions using the proposed methods. We also apply our methods to field data obtained in Tsukuba City, Japan.

4.2 Theory of the SPAC method

4.2.1 Fundamental mode

The basic theory of the SPAC method (*Okada*, 2003; *Asten*, 2006) is summarized as follows. Here we assume that microtremors are mainly composed of surface waves and that the fundamental mode of a surface wave is dominant. If microtremors are observed by a circle array with radius r (Figure 4.1), the complex coherencies COH between a central and a circumferential receiver can be defined as

$$COH(r, \omega, \theta, \phi) = exp[irkcos(\theta - \phi)], \tag{4.1}$$

where i is the imaginary number, ω is the angular frequency, k is the wavenumber, θ is the azimuthal angle, and ϕ is the azimuth of propagation of a single plane wave across the array. The azimuthal average of θ for the complex coherencies ρ yields SPAC coefficients,

$$\rho(r,\omega) = \frac{1}{2\pi}\int_0^{2\pi} exp[irkcos(\theta-\phi)]d\theta = J_0(rk) = J_0\left[\frac{\omega}{c(\omega)}r\right], \tag{4.2}$$

where J_0 is the Bessel function of the first kind of zero order. The azimuthal average of ϕ for complex coherencies also yields the same result, which indicates that a single pair of receivers is sufficient for plane waves coming from all directions. The phase velocities are estimated by fitting the observed SPAC coefficients to the Bessel function.

4.2.2 Extended spatial autocorrelation method

If we observe microtremors by using a circular array with radius r_0, SPAC coefficient of angular frequency ω_0 can be written as

$$\rho_{r_0,\omega_0} = J_0\left[\frac{\omega_0}{c(\omega_0)}r_0\right] = J_0(A), \tag{4.3}$$

where $A = \left[\frac{\omega_0}{c(\omega_0)}r_0\right]$ is constant. To estimate a unique phase velocity , it is necessary to decide upon a unique value of A from the observed SPAC coefficients. However, finding a unique A is difficult, especially near the minima and maxima of the Bessel function.

To overcome this difficulty, *Ling and Okada* (1993) and *Okada* (2003) proposed an analysis method called the extended spatial autocorrelation (ESPAC) method. If microtremors are observed by multiple receiver separations, the SPAC coefficient of

$\omega = \omega_0$ can be written as

$$\rho_{\omega_0}(r) = J_0\left[\frac{\omega_0}{c(\omega_0)}r\right] = J_0(Br), \tag{4.4}$$

where $B = \left[\frac{\omega_0}{c(\omega_0)}r_0\right]$ is constant. The optimum Bessel function can be found by using the least squares method. To increase the receiver separation distance r, the array observation does not always need to be repeated. As previously mentioned, if we assume that microtremors come from all directions, the observed SPAC coefficients go into the Bessel function without the azimuthal average of θ. Thus, possible pairs of an array can be used in the ESPAC method based on this assumption. *Bettig et al.* (2001) also extended the SPAC method in which arbitrarily shaped arrays can be used by averaging the SPAC coefficients within two circles.

4.2.3 Multimode analysis

Before we analyze microtremors that include higher modes of surface waves, we have to understand the description of the SPAC coefficients that consider higher modes. The SPAC coefficients that include partial waves with different velocities were derived by *Aki* (1957) and are defined as

$$\rho(r,\omega) = \sum_i \frac{P_i(\omega)}{P(\omega)} J_0\left[\frac{\omega}{c_i(\omega)}r\right], \tag{4.5}$$

$$P(\omega) = \sum_i P_i(\omega), \tag{4.6}$$

where P_i and c_i are the power and the velocity of ith component, respectively. Equation 4.5 shows that SPAC coefficients that include partial waves with different velocities can be described as the summation of each component weighted by its power fraction.

Harkrider (1964) derived the relative vertical displacement of the ith Rayleigh mode for a harmonic vertical point force, called the amplitude response (*Harkrider*, 1970). By extending Aki's method to higher modes of surface waves with amplitude response, *Tokimatsu et al.* (1992b) developed the multi-mode analysis method. *Tokimatsu et al.* (1992b) extracted the mode contribution that depends only on the frequency and regarded the value of its square as the power fraction in equation 4.5. It can be written as

$$\frac{P_i(\omega)}{P(\omega)} = \frac{c_i(\omega)A_i^2(\omega)}{\sum_i c_i(\omega)A_i^2(\omega)}, \tag{4.7}$$

where $A_i(\omega)$ is the amplitude response of ith mode. Note that in *Tokimatsu et al.* (1992a), *Tokimatsu et al.* (1992b), and *Tokimatsu* (1997) described the Bessel function in equation 4.5 by the cosine function, as *Tokimatsu et al.* (1992a,b) and *Tokimatsu* (1997) applied equation 4.7 to *f-k* analysis on the assumption of one-dimensional stochastic Rayleigh waves. We assume the power of each mode as equation 4.7 in the following discussion. *Yokoi* (2010) also derived the energy fractions of higher modes from seismic interferometry. The energy fractions by *Yokoi* (2010) are different from equation 4.7.

With this assumption, the theoretical SPAC coefficients (equation 4.5) can be calculated for a horizontally layered medium by using a theoretical dispersion curve and the amplitude response of each mode. In this study, we used DISPER80 (*Saito*, 1988), a computer program that calculates a theoretical dispersion curve and amplitude response. It is clear that if one mode of the surface waves is dominant, the observed phase velocities obtained from the SPAC method correspond to the dominant modes. However, if multi-mode components are predominant, the observed SPAC coefficients are described by the summation of the Bessel function of each mode weighted by its power fraction. As a result, the observed phase velocities cannot be explained by

the theoretical ones of only one mode, and they are called effective (apparent) phase velocities. When considering an inversion analysis, computation of the theoretical effective phase velocities for an assumed layered model is necessary.

Theoretical effective phase velocities can be calculated by the following procedure (*Obuchi et al.*, 2004). First, the root mean square error (RMSE) between the Bessel function and the theoretical SPAC coefficients is calculated by the following equation by changing the phase velocity $c(\omega)$:

$$RMSE(c,\omega) = \sqrt{\left[J_0\left(\frac{\omega}{c(\omega)}r\right) - \sum_i \frac{P_i(\omega)}{P(\omega)} J_0\left(\frac{\omega}{c_i(\omega)}r\right)\right]^2}, \tag{4.8}$$

Next, the velocity that minimizes RMSE in equation 4.8 can be considered to be the theoretical effective phase velocity $c_e(\omega)$ at angular frequency ω. These effective phase velocities correspond to the observed ones even if higher modes of surface waves are predominant.

However, it is necessary to modify this method to calculate the effective phase velocities when the ESPAC method is employed. Since the theoretical SPAC coefficients that consider higher modes are no longer described by the Bessel function, the effective phase velocities differ by a receiver separation distance. *Ohori et al.* (2002) compared observed phase velocities estimated from the ESPAC method with effective phase velocities. *Ohori et al.* (2002), however, used only the shortest receiver distance in the calculation of theoretical effective phase velocities. Thus, it is necessary to establish a method to calculate effective phase velocities that gives proper consideration to the receiver separation distances used in the ESPAC method.

Asten et al. (2002, 2004) proposed a method of fitting SPAC coefficients directly. In their method, S-wave velocity structures are directly inverted by comparing observed SPAC coefficients with theoretical ones. *Wathelet et al.* (2005) estimated S-wave velocity profiles from this method by introducing the neighborhood algorithm.

This method has the advantage that there is no need to estimate phase velocities from the observed SPAC coefficients. In spite of its simplicity, the method using the amplitude response has not been applied to the direct-fitting method yet.

Here, we propose two multi-mode analysis methods that use the amplitude response considering multiple receiver separation distances. One is to calculate theoretical effective phase velocities corresponding to the observed ones obtained by the ESPAC method. The other is to compare the observed SPAC coefficients with theoretical ones using the amplitude response. We will explain details of these methods in the next section.

4.3 Proposed multimode inversion methods

4.3.1 Method using theoretical effective phase velocities

We assume that higher modes are predominant in microtremors data and that the phase velocities are estimated by the ESPAC method. Theoretical effective phase velocities corresponding to the observed ones can be calculated by the following procedure. First, the RMSE between the Bessel function and the theoretical SPAC coefficients are calculated by the following equation by varying the phase velocity $c(\omega)$:

$$RMSE(c,\omega) = \sqrt{\frac{1}{N}\sum_{j}^{N}\left[J_0\left(\frac{\omega}{c(\omega)}r_j\right) - \sum_{i}\frac{P_i(\omega)}{P(\omega)}J_0\left(\frac{\omega}{c_i(\omega)}r_j\right)\right]^2}, \tag{4.9}$$

where r_j is the jth receiver separation distance in an array. Equation 4.9 differs from equation 4.8 in that the effect of multiple receiver separation distances is evaluated by the summation of the r_j. Next, the velocity that minimizes RMSE in equation 4.9 can be considered as the theoretical effective phase velocity $c_e(\omega)$ and corresponds to the observed one from the ESPAC method. If the effective phase velocities calculated

from equation 4.8 have some differences by a receiver separation distance, equation 4.9 would be important to implement a stable inversion in comparison with the method by *Ohori et al.* (2002), which uses the shortest receiver distance in the calculation of theoretical effective phase velocities. The dependence of effective phase velocities with a distance is discussed in appendix E. Here, we define the misfit function in an inversion as

$$Misfit = \sqrt{\frac{1}{M}\sum_{k}^{M}\left[c_{obs}(\omega_k) - c_e(\omega_k)\right]^2}, \tag{4.10}$$

where c_{obs} is the observed phase velocity obtained by the ESPAC method.

4.3.2 Method using theoretical SPAC coefficients

If we assume that the observed microtremors dominate the fundamental mode of surface waves, the misfit function in an inversion in the direct-fitting method by *Asten et al.* (2002, 2004) can be defined as

$$Misfit = \sqrt{\frac{1}{MN}\sum_{k}^{M}\sum_{j}^{N}\left[\rho_{obs}(r_j,\omega_k) - J_0\left(\frac{\omega_k}{c(\omega_k)}r_j\right)\right]^2}, \tag{4.11}$$

where ρ_{obs} is the observed SPAC coefficient. As *Okada* (2008) indicated, we can easily introduce their interpretation method to multi-modal analysis using amplitude response by equations 4.5-4.7. In this case, the misfit function can be defined as

$$Misfit = \sqrt{\frac{1}{MN}\sum_{k}^{M}\sum_{j}^{N}\left[\rho_{obs}(r_j,\omega_k) - \sum_{i}\frac{P_i(\omega_k)}{P(\omega_k)}J_0\left(\frac{\omega_k}{c_i(\omega_k)}r_j\right)\right]^2}. \tag{4.12}$$

4.3.3 Comparison of the two methods

Figure 4.2 shows a flowchart of the multi-mode analysis methods proposed in the previous section. The left side is for the analysis of observed data and the right side

is for forward modeling of an assumed medium. The final elastic model is decided upon by evaluating the errors between the observed and theoretical values (Figure 4.2, central panel). Here, we suppose that the ESPAC method is used in the estimation of the phase velocities. If an analysis method using effective phase velocities is employed, both observed and theoretical (effective) phase velocities will be approximately determined by the least squares fitting. In contrast, the direct-fitting method for comparing SPAC coefficients generates no such estimation errors (*Okada*, 2008). Because of this point, the direct-fitting method is superior to the method using effective phase velocities. It should be emphasized that neither proposed method needs to identify the mode of the observed phase velocities and SPAC coefficients.

In the ESPAC method, however, the least squares fitting of observed SPAC coefficients with different receiver separation distances to the Bessel function can reduce errors of the observed SPAC coefficients of each receiver separation distance. In addition, it is beneficial to estimate a dispersion curve even if we analyze microtremors by the direct-fitting of SPAC coefficients. It is known that the S-wave velocity structure can be roughly estimated from observed phase velocities by transforming 1.1 times phase velocities versus wavelength/$\alpha(\alpha = 2 - 4)$ to S-wave velocities versus depth (e.g. *Abbiss*, 1983; *Heisey et al.*, 1982). This S-wave velocity structure can be useful to determine an initial model or a search range of model parameters in an inversion if there is no prior information about observation area.

4.4 Synthetics test

To evaluate the effectiveness of the proposed methods, a numerical simulation study was conducted. It is well known that if the S-wave velocity decreases with increasing depth, higher modes of surface waves play a significant role at some frequencies (*Gucunski and Woods*, 1992; *Tokimatsu et al.*, 1992b). In the 4-layered model used for the simulation study, a high velocity layer is embedded in low-velocity

layers (Figure 4.3). Figure 4.4 shows the theoretical dispersion curves and power fractions up to the second higher mode. It can be seen that the first higher mode is predominant in the frequency range from 5 to 7.5 Hz. The first higher mode of surface waves would not be negligible in this frequency range. The anomalous predominance of first higher mode can be seen at about 2.5 Hz (Figure 4.4b). This anomaly is caused by the appearance of first higher mode with a high amplitude response at a cut-off frequency (Figure 4.4a), although the amplitude response of fundamental mode increases in this frequency range. The predominant higher modes in the low frequency range were studied by *Picozzi and Albarello* (2007). A similar feature can be seen in a field example. However, since we mainly use microtremors of the higher frequency range, the predominance of the first higher mode at about 2.5 Hz has little effect on our analysis.

Synthetic microtremors for a one-dimensional layered model have been successfully simulated by *Bonnefoy-Claudet et al.* (2006a), *Bonnefoy-Claudet et al.* (2004) and *Wathelet et al.* (2005). We simulated microtremors by the following procedure. The Discrete Wave-number Integral (DWI) method (*Bouchon and Aki*, 1977) was employed for the calculation of waveforms. The source was a vertical force with an 8 Hz Ricker wavelet. For the simplicity, constant and sufficiently large quality factors (Q=10000) are given for each layer in order to ignore anelastic attenuation. A triangular array with 10 receivers (Figure 4.5) was assumed in this simulation. One thousand sources were randomly distributed on the surface at radii from 500 to 1000 m from the central receiver of the array and the waveforms were calculated for each source independently. We assume that the wave propagates as a plane wave for the central receiver. Only the vertical component of the waveforms was used to estimate the Rayleigh wave dispersion. Simulated microtremors of about 30 s in duration were synthesized by superposing 50 waveforms randomly chosen from the 1000 waveforms. In this manner, 100 data sets were synthesized. Figure 4.6 shows an example of

simulated microtremors from one data set.

Next, we applied the proposed methods to the simulated data. The SPAC coefficients were obtained by averaging the azimuthal average of complex coherencies of 100 data sets with a cosine taper in time domain. Figure 4.7a shows the observed SPAC coefficients for $r = 25$ and 50 m. In addition, the theoretical SPAC coefficients of the superposed modes and theoretical ones up to the first higher mode are shown. The observed SPAC coefficients are in good agreement with the theoretical ones of the superposed modes even if the observed SPAC coefficients are between the fundamental and first higher mode.

By the ESPAC method, the phase velocities were estimated from observed SPAC coefficients of 9 different receiver separation distances (Figure 4.7b). The frequency range of the dispersion curve is determined by the following relation between the wavelength λ and the receiver separation distance r :

$$2r_{min} < \lambda < 4r_{max}, \tag{4.13}$$

where λ is the wavelength of the observed phase velocity, and r_{min} and r_{max} are the minimum and maximum receiver separation distance, respectively. The limit of the shortest wavelength is based on the spatial aliasing, whereas the longest one is determined empirically. The frequency range of SPAC coefficients used in an inversion is the same as that of the estimated phase velocities. Although the observed dispersion curve cannot be separated into dispersion curves for each mode in the frequency range from 5 to 7.5 Hz, the effective phase velocities calculated from equation 4.9 are consistent with the observed ones. It can be seen that both proposed methods are effective for multi-mode analyses that consider multiple receiver separation distances.

S-wave velocity profiles were estimated by inversions in which the proposed methods were introduced into a forward modeling. A genetic algorithm (GA) (e.g. *Gold-*

berg, 1989) with elite selection and dynamic mutation (*Yamanaka and Ishida*, 1996) was employed as the inversion method. The unknown parameters were the S-wave velocity and thickness of each layer, since empirical equations (*Ludwig et al.*, 1970; *Kitsunezaki et al.*, 1990) were used to obtain the P-wave velocity and density from the S-wave velocity. The reference S-wave velocity model used in the inversion was constructed only from the observed dispersion curve. The depth and S-wave velocity (Vs) of the reference model are determined by the following wavelength transformation (*Heisey et al.*, 1982):

$$Depth = \frac{1}{3}\lambda_{obs}, \tag{4.14}$$

$$V_s = 1.1 \times c_{obs}. \tag{4.15}$$

A 6-layered model was assumed in the inversion. The search range of the S-wave velocity and thickness was ±50 % for the reference model. The number of generations and the population were 200 and 100, respectively. Twenty trials were performed with the random seeds of an initial population. The final inverted model was constructed by averaging the S-wave velocity and thickness for each layer over 20 trials. Theoretical dispersion curves and power fractions were calculated up to the third higher mode in a forward modeling.

Figure 4.8 shows the average values of the misfit functions and the standard deviations for each generation. The misfit functions of the last 150 generations show little decrease and the standard derivation of the last generation is quite small, which indicate convergence of the GA inversions. Since objective functions and their dimensions of both methods are different, it is difficult to compare the values of standard deviations. However, standard deviations of the inverted S-wave velocity models can be compared because the dimensions of inverted models are same. The S-wave velocity

profiles estimated from an inversion that introduces two kinds of proposed forward modeling are shown in Figures 4.9 and 4.10. The final inverted models and their standard deviations are quite similar. The reversal of the S-wave velocity is well retrieved by either multi-mode inversion analysis. However, the standard deviations near the infinite half-space are relatively large. This is because the observed phase velocities or SPAC coefficients do not have sufficient sensitivity to deep structure due to a lack of estimated values at lower frequencies.

Figure 4.11 compared the inverted velocity models using only the fundamental mode component with those using multimode components. The reversal of S-wave velocities was overestimated by inversion using only the fundamental mode in both inversion methods.

4.5 Field example

We also applied the proposed methods to field data. The survey site is located in Tsukuba City, Japan. Geophones with a natural frequency of 2 Hz were used as receivers. The array shape was similar to that shown in Figure 4.5, and the largest aperture of the array was 30 m. The sampling time was 2 ms and each data set consists of 8192 samples. Finally, 300 data sets of about 80 min were obtained. Figure 4.12 shows an example of observed microtremors. P- and S-wave velocities were obtained at this site by PS-logging (*Suzuki and Takahashi*, 1999). Figure 4.13 shows the theoretical dispersion curves and power fractions up to the second higher mode constructed from PS-logging data. It can be seen that the power fraction of the first higher mode is predominant near 7.5 Hz. Moreover, the second higher mode has some influence at high frequencies.

The SPAC coefficients and dispersion curve were obtained from 300 data sets in the same way as the synthetic test. Figure 4.14a shows the observed SPAC coefficients for $r = 15$ and 30 m calculated from microtremor data. The theoretical SPAC coefficients

of the superposed modes and theoretical ones up to the second higher mode are also shown. Figure 4.14b shows the observed phase velocities from the ESPAC method for which the frequency range was determined by equation 4.13. Despite being within this frequency range, phase velocities could not be obtained for frequencies higher than 13.2 Hz because they did not show significant dispersion. In the frequency range from 5 to 10 Hz where the observed SPAC coefficients and phase velocities lie between the fundamental and first higher mode, the observed values are in good agreement with the theoretical ones considering higher modes. However, there are discrepancies between observed and theoretical values below 4 Hz. Figure 4.14a shows that the observed SPAC coefficient agreed with theoretical one becomes slightly lower with the increase of a receiver separation distance, which indicates the wavelength dependence of these discrepancies. The phase velocities at lower than 4 Hz are also included in the second and third reliable regions of 4 regions named as 'acceptable' and 'critical' according to the classification by *Cornou et al.* (2006). Thus, the discrepancies below 4 Hz would be generated from instability of estimated wavelengths.

The S-wave velocity profiles were estimated by inversions. The procedure and parameters of the inversions were the same as in the simulation study. Figure 4.15 shows the average values of the misfit functions for each generation. The S-wave velocity profiles estimated from inversions by two proposed methods of forward modeling are shown in Figures 4.16 and 4.17. The standard deviations of inverted models using effective phase velocities are much higher than those using SPAC coefficients. The final S-wave velocity model by an inversion using effective phase velocities is poorly resolved. It is considered this failure is caused by the discrepancies in the observed phase velocities below 4 Hz. Although the inversion using SPAC coefficients is also effected on the misfit below 4 Hz, the S-wave velocity consistent with logging data can be inverted.

Figure 4.18 shows the comparison of the inverted velocity models using only the

fundamental mode with those using multimode components. Compared to logging data, the reversal of S-wave velocities obtained by inversion using only the fundamental mode is unrealistic.

Then, we considered giving a constraint in the inversion using effective phase velocities in order to improve the S-wave velocity estimation. Since the discrepancies of observed phase velocities below 4 Hz are considerably related with an infinite half-space of inverted S-wave velocity, we constrained the velocity of an infinite half-space to 700 m/s and the depth to 50 m as prior information in an inversion. Figure 4.19 shows the result of the inversion by effective phase velocities when prior information is introduced. It can be seen that the S-wave velocity structure is better resolved. From this result, we suggest the objective function using SPAC coefficients (equation 4.12) is robust than that using effective phase velocities (equation 4.10) in the point that the former can give a better weighting for low frequencies when observed values have significant errors.

4.6 Conclusions

In this study, we proposed two multi-mode analyses in the SPAC method using amplitude response of surface waves. The use of amplitude response is superior in that there is no need to identify the observed modes, and therefore mode misidentification is avoided. Practical application point of view, this point becomes important since it may solve an uncertainty problem by a lack of experimental knowledge of engineers. The first method is to calculate the theoretical effective phase velocities corresponding to the estimated ones by the ESPAC method. The second method is to fit SPAC coefficients directly. The latter approach is simpler than the former one.

To conduct quantitative verification, we simulated microtremors with predominant higher modes of surface waves. Although the estimated phase velocities from the ESPAC method were between theoretical phase velocities of fundamental mode

and first higher mode at some frequencies, the theoretical effective phase velocities were consistent with the estimated ones. The observed SPAC coefficients were also consistent with the theoretical ones. These methods were included in the forward modeling of a GA inversion. The reversal layer of a S-wave velocity, which usually plays an important role in higher modes, was successfully inverted by both proposed methods although it was overestimated by inversion using only the fundamental mode.

In addition, we applied the proposed methods to field data in which higher modes were considered to be predominant from PS logging data. The S-wave velocity estimated by an inversion using SPAC coefficients is well consistent with that from logging data. On the other hand, the inverted model using effective phase velocities was poorly resolved. Introduction of prior information about the infinite half-space layer, however, improved the result of the inversion. When we apply inversion using only the fundamental mode, the unrealistic reversal of S-wave velocities was estimated.

The simulation study and field example demonstrated that results from our proposed methods are mostly in good agreement with the observed phase velocities and SPAC coefficients. However, these methods have to be applied carefully to an inversion analysis without any prior information. If the observed values have low quality for crucial S-wave velocities when applying the multi-mode analysis (e.g., below 4 Hz in Figure 4.14), the inverted models may be trapped in the local minimum as in Figure 4.16. Meanwhile, the S-wave velocity structure was successfully estimated by an inversion using SPAC coefficients without any constraints for the reference model. Because of this, we suggest that the multi-mode inversion using SPAC coefficients has a better weighting for low frequencies when observed values have significant errors and therefore, it is more robust than an inversion using effective phase velocities. To verify the effectiveness of the proposed methods, the observed microtremors need to be applied to various areas where borehole data are available for a quantitative evaluation.

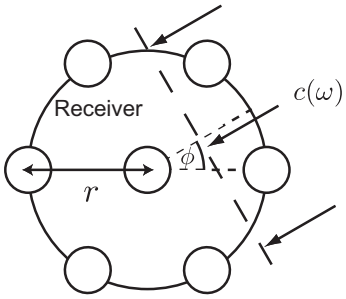

Figure 4.1: Geometry of a receiver array and an incident plane wave.

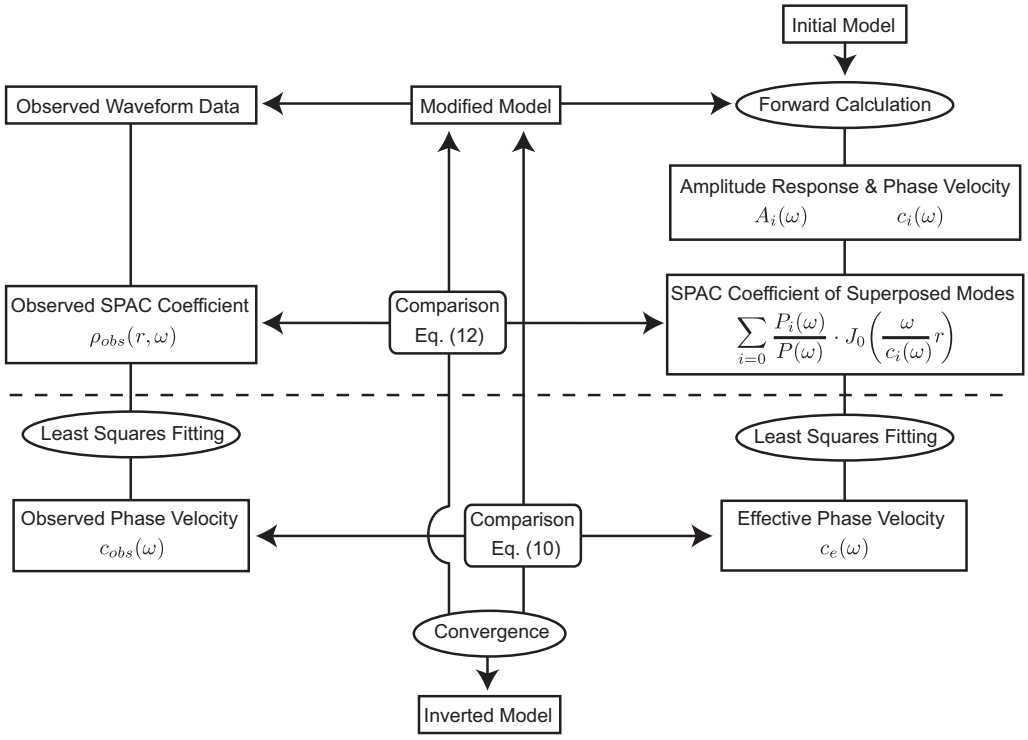

Figure 4.2: Flowchart of proposed microtremor analyses that consider higher modes and multiple receiver separation distances.

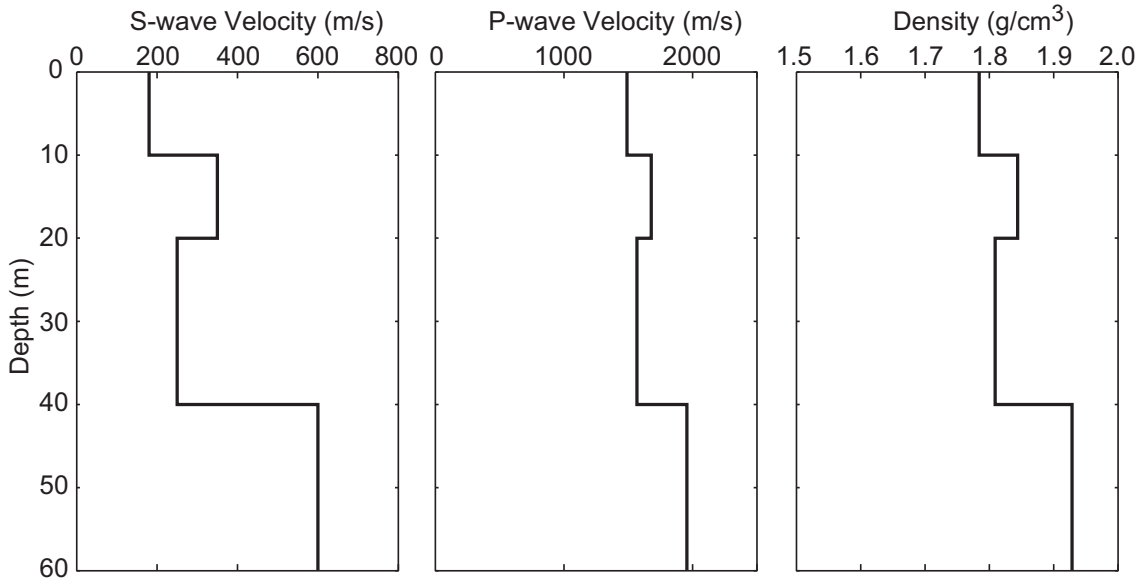

Figure 4.3: Simulated 4-layered model.

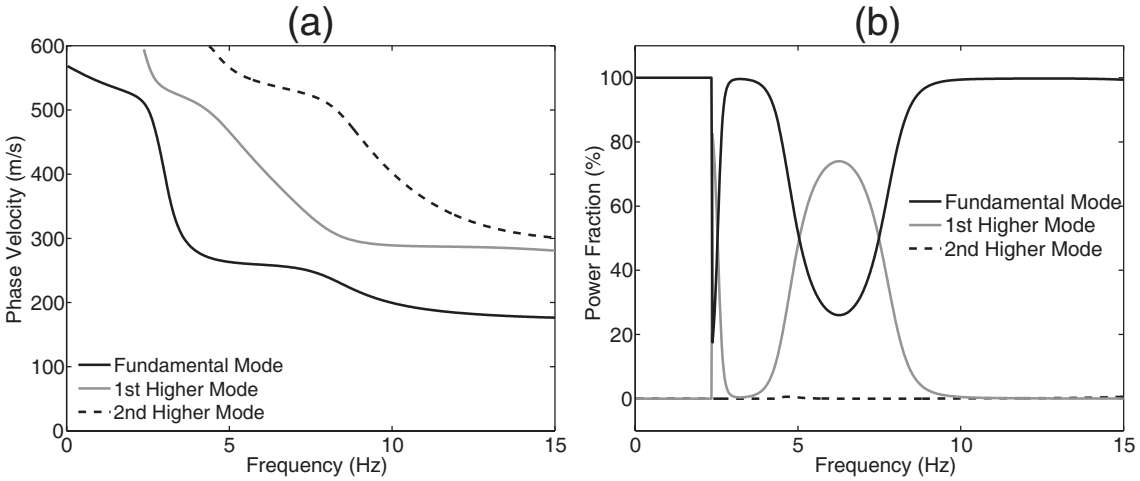

Figure 4.4: (a) Theoretical dispersion curves and (b) power fractions up to second higher modes for simulated model (Figure 4.3).

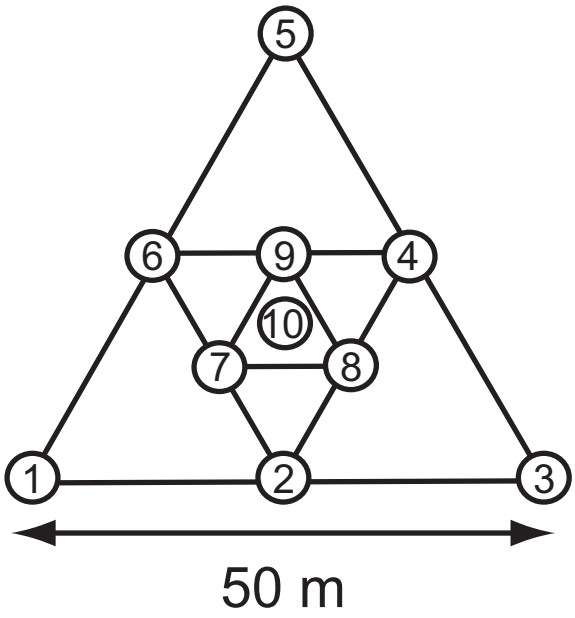

Figure 4.5: Assumed array shape.

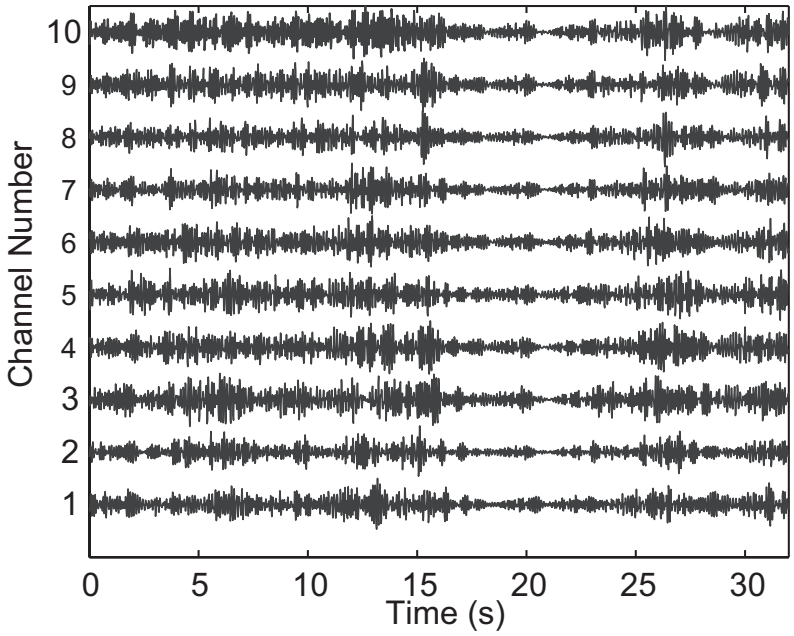

Figure 4.6: Simulated microtremors from one data set. The receiver number corresponds to Figure 4.5.

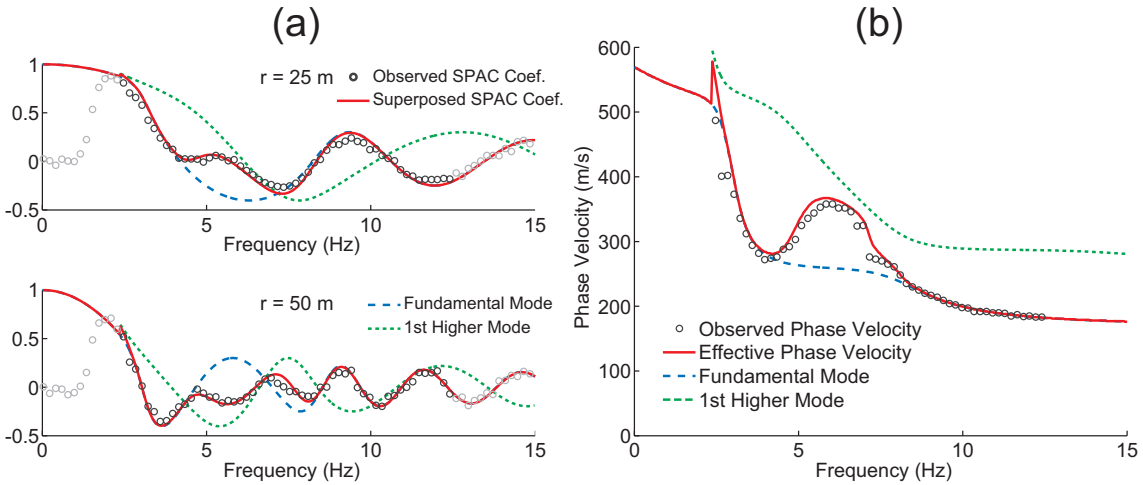

Figure 4.7: Comparison of the observed SPAC coefficients with theoretical ones (red lines) corresponding to $r = 25$ and 50 m. Only the black circles among the observed SPAC coefficients were used in an inversion. (b) Comparison of the observed phase velocities (black circles) from the ESPAC method with theoretical effective phase velocities (red line).

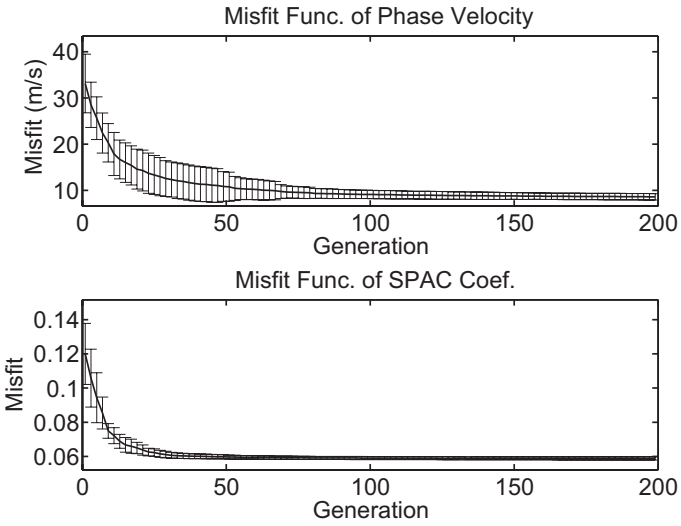

Figure 4.8: The average of the misfit functions in each generation for simulated data. The error bars show the standard deviations.

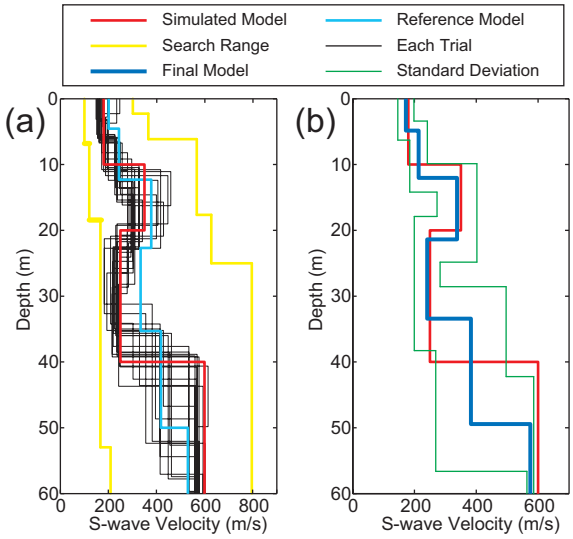

Figure 4.9: Results of inversions using effective phase velocities. (a) Simulated model (red), reference model constructed by equations 4.14 and 4.15 (cyan), inverted models for each trial (black), and the search range in for the GA inversion (yellow). (b) Final inverted model (blue) obtained by averaging the S-wave velocities and thicknesses for each layer over 20 trials and their standard deviations (green).

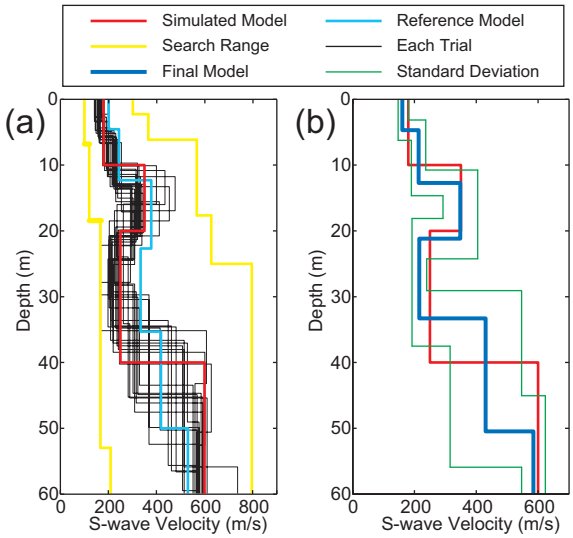

Figure 4.10: Results of inversions using SPAC coefficients. (a) Simulated model (red), reference model constructed by equations 4.14 and 4.15 (cyan), inverted models for each trial (black), and the search range for the GA inversion (yellow). (b) Final inverted model (blue) obtained by averaging the S-wave velocities and thicknesses for each layer over 20 trials and their standard deviations (green).

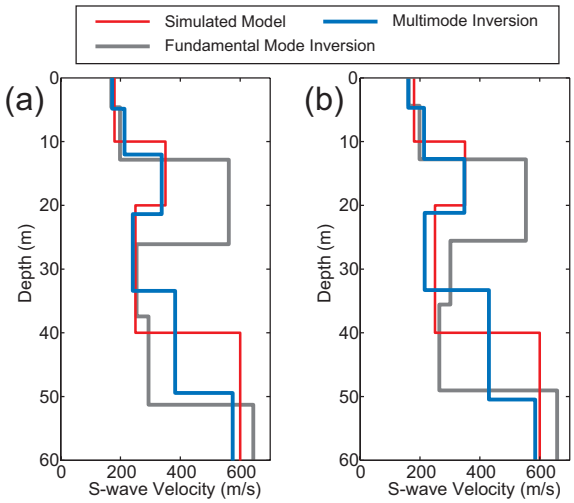

Figure 4.11: Comparison of inverted velocity models using multimode components with those using only the fundamental mode component for (a) effective phase velocities and (b) SPAC coefficients.

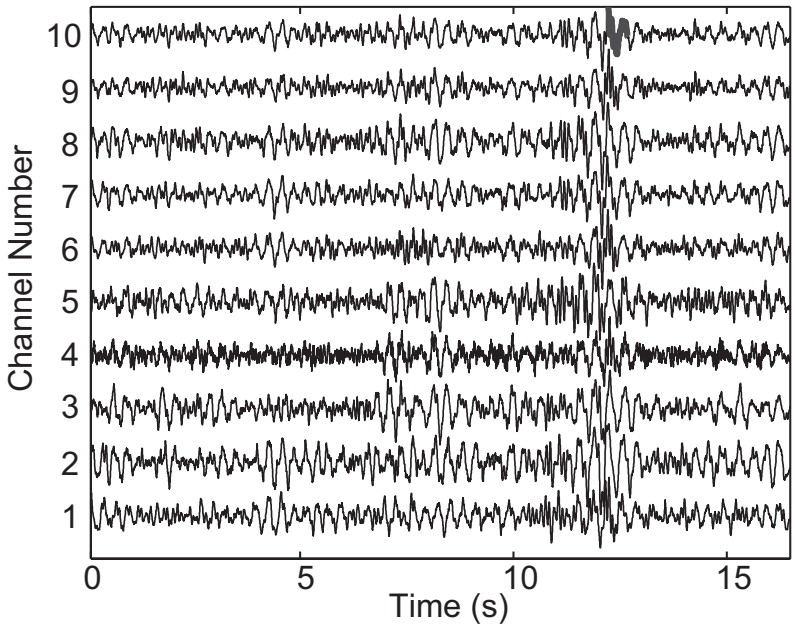

Figure 4.12: Observed microtremors from one data set. The receiver number corresponds to Figure 4.5.

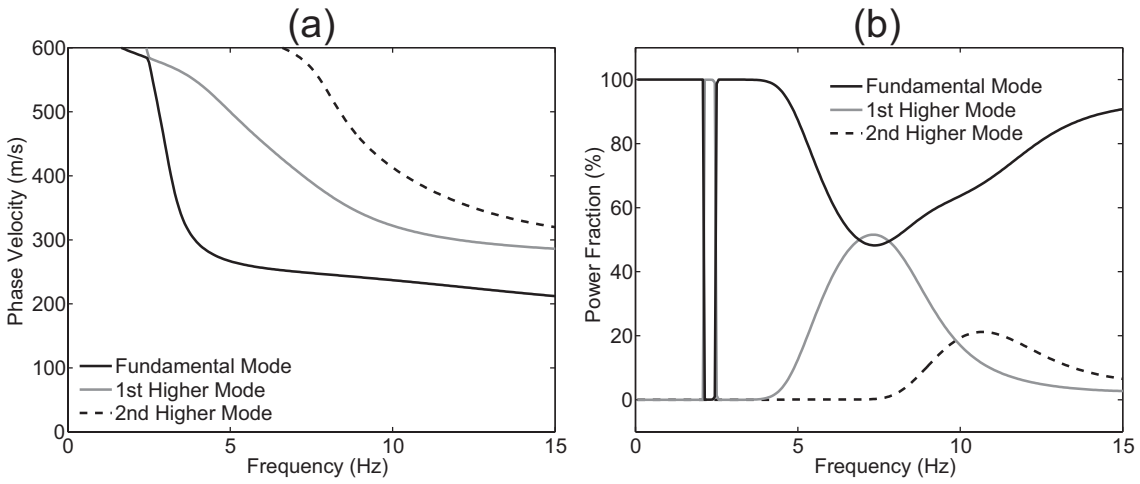

Figure 4.13: (a) Theoretical dispersion curves and (b) power fractions up to second higher modes for a layered model constructed by PS logging data.

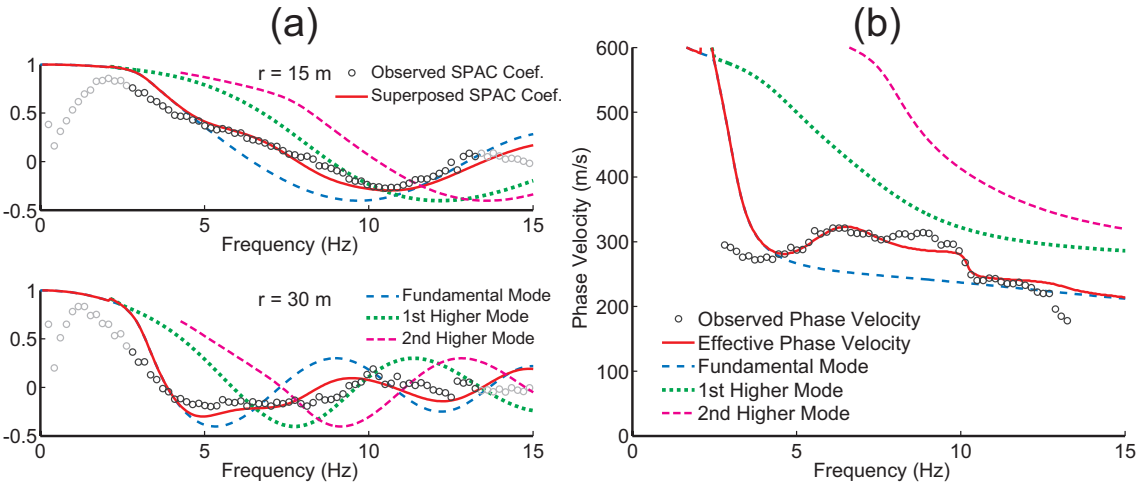

Figure 4.14: (a) Comparison of observed SPAC coefficients with theoretical ones (red lines) corresponding to $r = 15$ and 30 m. Only the black circles among the observed SPAC coefficients were used in an inversion. (b) Comparison of the observed phase velocities (black circles) from the ESPAC method with theoretical effective phase velocities (red line).

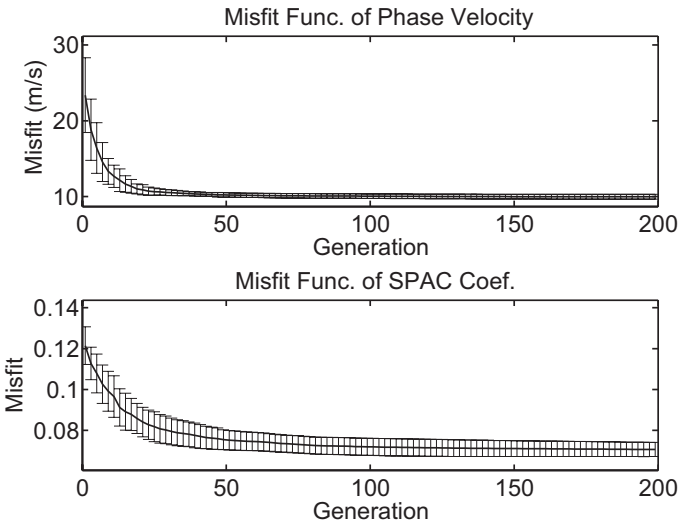

Figure 4.15: The average of the misfit functions in each generation for field data. The error bars shows the standard deviations.

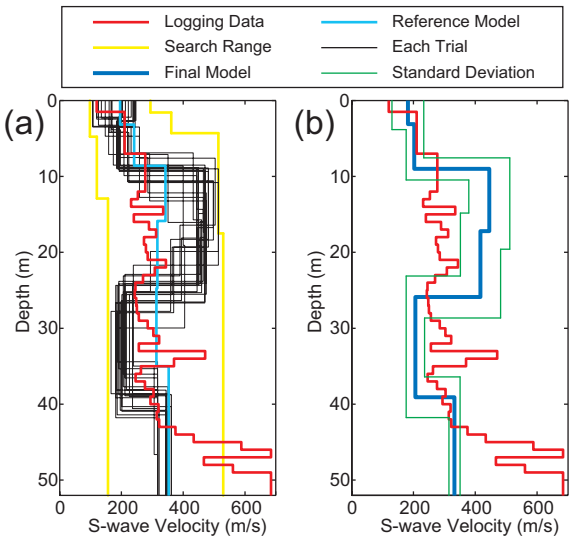

Figure 4.16: Results of inversions using effective phase velocities. (a) Logging data (red), reference model constructed by equations 4.14 and 4.15 (cyan), inverted model for each trial (black), and the search range for the GA inversion (yellow). (b) Final inverted model obtained by averaging the S-wave velocities and thicknesses for each layer over 20 trials (blue) and their standard deviations (green).

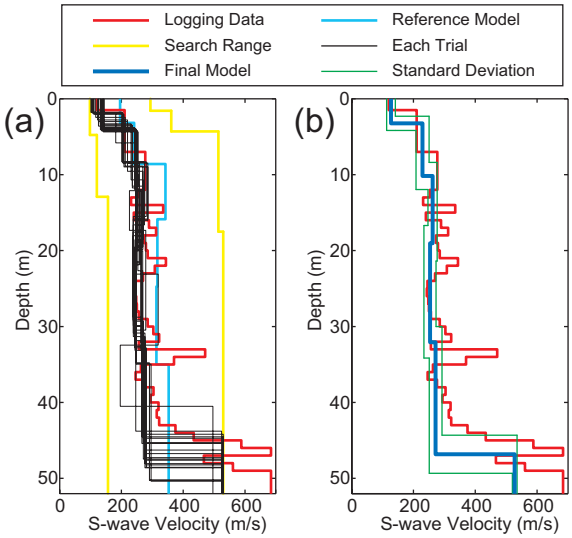

Figure 4.17: Results of inversions using SPAC coefficients. (a) Logging data (red), reference model constructed by equations 4.14 and 4.15 (cyan), inverted models for each trial (black), and the search range for the GA inversion (yellow). (b) Final inverted model (blue) obtained by averaging the S-wave velocities and thicknesses for each layer over 20 trials and their standard deviations (green).

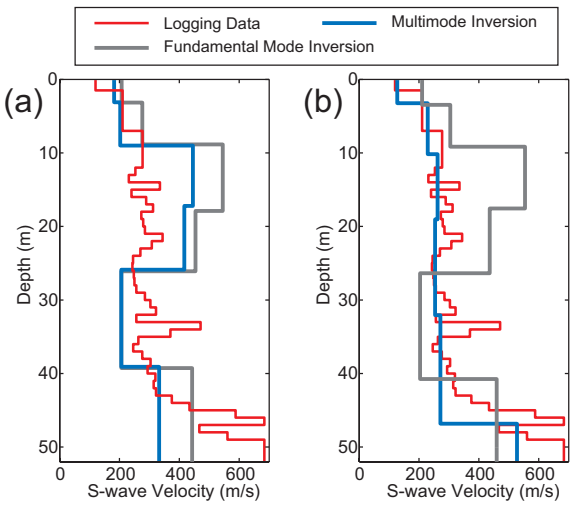

Figure 4.18: Comparison of inverted velocity models using multimode components with those using only the fundamental mode component for (a) effective phase velocities and (b) SPAC coefficients.

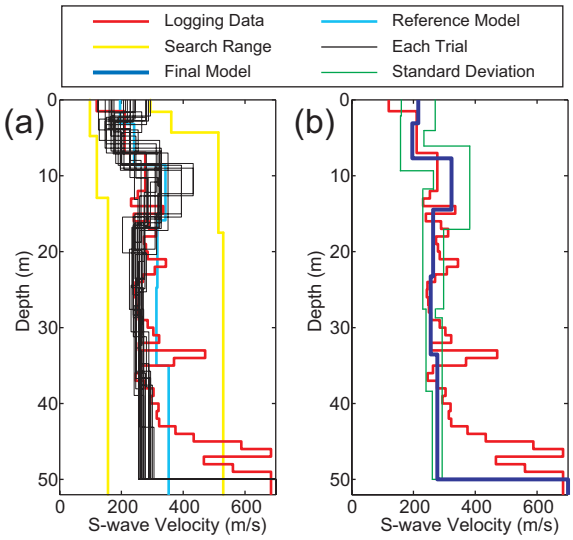

Figure 4.19: Results of inversions using effective phase velocities. The S-wave velocity and the depth of the infinite half-space were fixed at 700 m/s and 50 m, respectively. (a) Logging data (red), reference model constructed by equations 4.14 and 4.15 (cyan), inverted models for each trial (black), and the search range for the GA inversion (yellow). (b) Final inverted model (blue) obtained by averaging the S-wave velocities and thicknesses for each layer of 20 trials and their standard deviations (green).

CHAPTER V

Separating mixing modes by the multichannel analysis of surface waves with deconvolution analysis

5.1 Introduction

The surface wave method has been widely applied as a non-destructive means for obtaining S-wave velocity structures (e.g. *Miller et al.*, 1999; *Ryden and Lowe*, 2004; *Lin et al.*, 2004; *Foti et al.*, 2009; *Socco et al.*, 2010; *Tsuji et al.*, 2012). The surface wave method utilizes the dispersion characteristics of surface waves. *Nazarian et al.* (1983) have introduced the spectral analysis of surface waves method (SASW) in which dispersion curves of surface waves are estimated from a pair of receivers. The accuracy of dispersion curves estimates is improved by analysis of multichannel seismic data with the multichannel analysis of surface waves (MASW) method (*Park et al.*, 1998, 1999a) or the *f-k* method (*Foti*, 2000, 2005). Because surface waves are most sensitive to S-wave velocities, S-wave velocity structures can be estimated by inversion of dispersion curves (e.g. *Xia et al.*, 1999).

Surface waves have different propagation velocities at different frequencies. The propagation mode with the slowest propagation velocity is the fundamental mode, and the other modes are referred to as higher modes. The fundamental mode of

surface waves is usually the focus of a surface wave analysis. However, higher modes of surface waves cannot be ignored when a low-velocity layer is embedded between soft layers (e.g. *Tokimatsu et al.*, 1992b; *Lu et al.*, 2007; *Tsuji et al.*, 2012). In inversion analysis, inclusion of higher surface wave modes improves the resolution of S-wave velocity estimations, the result being an increase of the investigation depth (e.g. *Xia et al.*, 2003; *Luo et al.*, 2007).

One of the difficulties associated with multimode analysis of surface waves is the separation of multimode signals. The receivers must be spread out over a long distance to clearly separate multimode surface waves (*Bergamo et al.*, 2012; *Ikeda et al.*, 2013b), and a large number of receivers is required to suppress noise effects. However, such field observations are sometimes difficult to conduct because of financial or topographical restrictions. Even if the component of each mode is clearly separated, there is still difficulty in identifying the observed mode number. Consequently, the mode misidentification generates substantial errors in inversion (e.g. *Zhang and Chan*, 2003; *Maraschini et al.*, 2010).

To overcome these problems, a number of authors have developed multimode inversion techniques that do not require mode identification. For example, *Tokimatsu et al.* (1992b), *Tsuji et al.* (2012), and *Ikeda et al.* (2012) have applied multimode inversion techniques for inverting mixed modes that take into consideration the theoretical amplitude of multimode surface waves. To consider the effects of leaky modes and body waves, *Forbriger* (2003) and *O'Neill and Matsuoka* (2005) have applied full-waveform inversion without any mode identification, although such analysis requires much computational time. *Maraschini et al.* (2010) and *Maraschini and Foti* (2010) have also proposed a new misfit function in multimode inversion based on the Haskell-Thomson matrix method.

In contrast, very few studies have focused on the retrieval of multimode surface waves from observed seismic data. *Luo et al.* (2009) have proposed a high-resolution

linear Radon transform for separating and reconstructing multimode surface waves. Deconvolution techniques have also been applied to the estimation of dispersion images to emphasize the peaks corresponding to particular surface wave modes. *Nishida et al.* (2008) and *Picozzi et al.* (2010) have applied deconvolution to ambient noise data, and *Maupin* (2011) has applied deconvolution to teleseismic data. However, there has not been a clear awareness of the advantage of applying deconvolution. Futhermore, the deconvolution technique has not been applied to dispersion images constructed from surface seismic data for near-surface S-wave velocity estimation.

In this study, we introduced the deconvolution technique into the MASW to separate mixing modes in dispersion images. This technique is based on the fact that estimated dispersion images can be described by convolution of true spectra with the array smoothing function (ASF) discussed by *Boiero and Socco* (2011). For multimode surface data, we change the MASW computational procedure to obtain a description in the proximity of the summation of the convolution for each mode component. We have used both simulated and field data to demonstrate the effectiveness of the proposed technique.

5.2 Method

5.2.1 Multichannel analysis of surface waves

In this section, we review the multichannel analysis of surface waves (MASW) proposed by *Park et al.* (1998, 1999a). Dispersion images in the wavenumber (phase velocity) versus frequency domain can be obtained from multichannel seismic data with the MASW method. First, a Fourier transform is used to transform observed seismic data in the time domain into the frequency domain. Based on the description by *Tokimatsu et al.* (1992b), if we assume that seismic data are composed of the fundamental mode of surface waves, observed data can be described in the frequency

domain as follows:

$$F(f,x) = \frac{1}{\sqrt{x}} A(f) e^{-ik_0 x}, \tag{5.1}$$

where f is the frequency, x is the offset from the source, k_0 is the wavenumber for the fundamental mode of surface waves, and $A(f)$ is a term that depends on frequency. For simplicity, we have neglected in equation 5.1 anelastic attenuation, the time-dependent term and the constant value, which is independent of the frequency and offset. Seismic data in the frequency domain are then normalized with respect to absolute values and integrated over receivers with a phase shift. Use of absolute values of integrated data allows dispersion images U to be described as follows:

$$U(f,k) = \left| \int_{-\infty}^{\infty} \frac{F(f,x)}{|F(f,x)|} e^{ikx} dx \right|. \tag{5.2}$$

Wavenumbers or phase velocities with local maximum values in U can be defined as predominant surface wave modes.

5.2.2 Convolution equation of dispersion images using the ASF

Observed dispersion images are described by convolution of true spectra with the ASF, as demonstrated in the case of the *f-k* method by *Boiero and Socco* (2011) and in the case of the CMP cross-correlation method by *Ikeda et al.* (2013b). The dispersion images in equation 5.2 have impulses at wavenumbers corresponding to the fundamental mode of surface waves because dispersion images become delta functions in which the wavenumber is shifted to k_0. Because seismic data are observed by a finite number of receivers, equation 5.2 should be rendered by using a summation as

follows:

$$U(f,k) = \left| \sum_{j}^{N} \frac{F(f,x_j)}{|F(f,x_j)|} e^{ikx_j} \right| = \left| \sum_{j}^{N} e^{i(k-k_0)x_j} \right|, \tag{5.3}$$

where N is the number of receivers used in data acquisition. The dispersion images described by equation 5.3 become absolute values of the sinc function with a peak at k_0. Thus, we can describe equation 5.3 as follows:

$$U(f,k) = |ASF(k)| * P_0(f,k), \tag{5.4}$$

$$ASF(k) = \sum_{j}^{N} e^{ikx_j}, \tag{5.5}$$

where ASF is the array smoothing function and P_0 is the theoretical spectrum for the fundamental mode of surface waves. Thus, dispersion images observed with MASW can be described by convolution of theoretical spectra with the ASF (Figure 5.1). The ASF can be obtained for any wavenumber by using an offset x.

Figure 5.2 shows three examples of absolute values of the ASF for 24 receivers with a receiver interval of 1 m, 48 receivers with a receiver interval of 1 m, and 24 receivers with a receiver interval of 2 m. It is apparent that the ASF is a periodic function because of a spatial aliasing associated with the receiver interval. The shorter the receiver interval is, the longer the period of the ASF is. Moreover, the ASF has more distinct peaks the longer the distance between minimum and maximum offsets (spread length).

5.2.3 Deconvolution of dispersion images

Because observed dispersion images can be described by convolution, true spectra can be estimated by applying deconvolution with the ASF. By applying a Fourier

transform in the wavenumber k domain, theoretical spectra in the transformed k' domain can be described as a deconvolution:

$$P_0(f,k') = \frac{U(f,k')}{|ASF(k')|}. \tag{5.6}$$

For stability of division in equation 5.6, deconvolution is applied with a stabilization parameter ϵ.

$$P_0(f,k') = \frac{U(f,k')\overline{ASF(k')}}{|ASF(k')|\overline{|ASF(k')|} + \epsilon}, \tag{5.7}$$

where the overbar signifies the complex conjugate. Note that when we apply deconvolution by using equation 5.7, we normalize the ASF in the k' domain in equation 5.7 with respect to its maximum absolute value.

5.2.4 Modified MASW for multimode surface wave data

We now consider the application of the MASW and deconvolution to a case of seismic data that includes higher modes of surface waves. Based on the description by *Tokimatsu et al.* (1992b), multimode surface wave data are described as follows:

$$F(f,x) = \frac{1}{\sqrt{x}} \sum_{m=0} A_m(f) e^{-ik_m x}, \tag{5.8}$$

where k_m and A_m are the m^{th} mode component of the wavenumber and a term that depends on frequency, respectively. For simplicity, we neglect anelastic attenuation in equation 5.8. Substituting equation 5.8 into equation 5.3, we obtain,

$$U(f,k) = \left| \sum_m A_m(f) \sum_j^N \frac{1}{|\sum_m A_m(f) e^{-ik_m x_j}|} e^{i(k-k_m)x_j} \right|, \tag{5.9}$$

The value of $|\sum_m A_m(f)e^{-ik_m x_j}|$ in equation 5.9 depends on x_j. This term generates errors when retrieving delta functions for each mode component by deconvolution with ASF in equation 5.7. To reduce this effect, we modify the definition of dispersion images U in equation 5.3 by multiplying the square root of x by F as follows:

$$\begin{aligned} U(f,k) &= \left| \sum_j^N \sqrt{x_j} F(f,x_j) e^{ikx_j} \right| = \left| \sum_m A_m(f) \sum_j^N e^{i(k-k_m)x_j} \right| \\ &= \left\{ \left(\sum_m A_m(f) \sum_j^N e^{i(k-k_m)x_j} \right) \left(\sum_m A_m(f) \sum_j^N e^{-i(k-k_m)x_j} \right) \right\}^{0.5} \\ &= \left\{ \sum_m A_m(f)^2 \left| \sum_j^N e^{i(k-k_m)x_j} \right|^2 \right. \\ &\quad \left. + 2 \sum_m \sum_{n(\neq m)} A_m(f) A_n(f) \sum_j^N \sum_p^N cos\left[(k-k_m)\, x_j - (k-k_n)\, x_p \right] \right\}^{0.5} \end{aligned} \tag{5.10}$$

In this paper, as a matter of convenience, this procedure will be characterized as the modified MASW. If only a single mode of surface waves is dominant and anelastic attenuation is neglected, the result is equivalent to the definition of the MASW in equation 5.3. If we assume that the second term in the last line of equation 5.10 can be neglected, dispersion images can be described by summation of the convolution of the ASF with the theoretical spectrum of each mode component as follows:

$$U(f,k) = \sum_m A_m(f) \left| \sum_j^N e^{i(k-k_m)x_j} \right| = \sum_m |ASF(k)| * P_m(f,k), \tag{5.11}$$

where P_m is the theoretical spectrum of the m^{th} mode component of surface waves. Deconvolution would therefore be applicable to analysis of seismic data, including higher modes of surface waves, to separate mixing mode components.

5.3 Simulation study

In this section, we demonstrate the proposed methods by using numerically synthesized data, with or without consideration of anelastic attenuation. The simulated four-layer model is slightly modified from case 3 in *Tokimatsu et al.* (1992b) (Table 5.1) and includes a low-velocity layer. The presence of a low-velocity layer makes the first higher mode of surface waves predominant. We employed the discrete wavenumber integral method of *Bouchon and Aki* (1977) to calculate the vertical component of synthetic waveforms. The source was a vertical force with a 15 Hz Ricker wavelet. We put the source at a depth of 1 m below the surface. We used 48 receivers, the receiver interval between receivers being 1 m. The minimum offset was 2 m. The corresponding ASF is depicted in Figure 5.2b. The duration of the synthesized seismogram was 2 s.

5.3.1 Elastic modeling

First, we ignored anelastic attenuation by setting the quality factor to 1000 for all layers. Figure 5.3 shows the dispersion curve images estimated from simulated waveforms by the MASW and the modified MASW. It is apparent that the fundamental mode is dominant at most frequencies in both dispersion images. The first higher mode at frequencies higher than 30 Hz is also more clearly identified by using the modified MASW. Although the fundamental mode and the first higher mode are predominant at frequencies of 5-10 Hz, the fundamental mode can be more clearly identified in the dispersion image produced by the modified MASW. At about 10 Hz, we observe the smooth mode transition from the first higher mode to the fundamental mode (Figures 5.3c and 5.3d). If low frequency components at frequencies lower than 7 Hz are insufficient, we might misinterpret the first higher mode at frequencies of 5-10 Hz as the fundamental mode.

We then used equation 5.7 to apply deconvolution to the dispersion images. Fig-

ures 5.4 and 5.5 depict the results of deconvolution for dispersion images estimated by the MASW and the modified MASW, respectively. In both cases, the peaks corresponding to predominant modes are enhanced by the deconvolution technique compared to the dispersion images without deconvolution (Figure 5.4). However, the peak positions are in most cases similar to those without deconvolution when a single mode component of surface waves is dominant, as *Maupin* (2011) has pointed out.

Figures 5.4d and 5.5d show slices of the deconvolved images at 10 Hz where there is a mode transition from the first higher mode to the fundamental mode. Applying deconvolution to the dispersion image estimated from the modified MASW clearly separates two mixing modes at 10 Hz (Figure 5.5d). Separating two modes from one peak contributes to not only improving phase velocity estimations but also identifying mode transition at corresponding frequencies. On the other hand, identifying the secondary peak is not easy in the deconvolved image from the MASW (Figure 5.4d). Values of 0.01-0.05 for ϵ are enough to retrieve two mixing modes at 10 Hz.

5.3.2 Anelastic modeling

We neglected the effects of anelastic attenuation in the previous section because they are complicated for multimode data. In reality, however, anelastic attenuation might play an important role in the analysis of multimode components of surface waves. We therefore, applied the proposed method to numerically simulated data that included the effects of anelastic attenuation. The parameters for the simulated model were the same as those in Table 5.1. The quality factors for each layer are given in Table 5.2.

Figure 5.6 shows the dispersion images estimated with the MASW and the modified MASW. We also observe the smooth mode transition at 10 Hz. At this frequency, the peak for the modified MASW exists at the midpoint between the fundamental mode and the first higher mode (Figure 5.6d) whereas the dispersion image for the

MASW is contaminated probably due to the effect of the hidden fundamental mode (Fig. 5.6c). The dispersion image from the modified MASW does not have clear side lobes near the peak positions at high frequencies. This is because dispersion images with the modified MASW are affected by anelastic attenuation whereas the normalization in the MASW (equation 5.3) can remove the effects of attenuation (*Park et al.*, 1999b; *Park*, 2011).

Figure 5.7 shows the results of applying deconvolution to the dispersion images. Two mode components are mixed at 10 Hz without deconvolution, but they can be successfully separated by applying the deconvolution technique with the modified MASW (Fig. 5.7d). Although two peaks are also generated from one peak by the deconvolution technique with the MASW, it is difficult to distinguish the secondary peak due to the other peaks.

5.4 Application to field data

We then applied the proposed methods to field data acquired at Uto city, Kumamoto Prefecture, Japan (*Watanabe et al.*, 2011). A sledge hammer was used as a source. Twenty-four geophones were placed at intervals of 1 m. The minimum offset was 2 m. The sampling time was 2 ms, and the number of sample was 1024. The corresponding ASF is depicted in Figure 5.2a.

Figure 5.8 shows the dispersion images estimated with the MASW and the modified MASW. The fundamental mode of surface waves at frequencies lower than 7 Hz is observed in these images. Owing to this mode, we can interpret the dispersion curve at frequencies of 7-15 Hz as that for the first higher mode. This first higher mode might be related to reversal of S-wave velocities. It is considered that the fundamental mode and the first higher mode are mixed at about 15 Hz. At frequencies higher than 15 Hz, a single mode component is dominant. More continuous peaks can be identified with the modified MASW. The dispersion image estimated from the

modified MASW does not have clear side lobes at high frequencies, the indication being that observed seismic data are affected by anelastic attenuation, as was the case in the simulation study.

Figure 5.9 shows the result of applying deconvolution to dispersion images produced with the MASW and modified MASW. At 15.1 Hz, the two peaks were generated from one peak by deconvolution analysis with the modified MASW whereas the peak position of the secondary peak is modified by deconvolution analysis with the MASW (Figs. 5.9b and 5.9e). The two modes for the MASW and the modified MASW are good consistent with each other. At 15.6 Hz, the secondary peak is not retrieved in the deconvolved image with the MASW (Fig. 5.9c). On the other hand, two peaks were generated by deconvolution analysis with the modified MASW (Fig. 5.9f).

5.5 Conclusions

To separate mixing multimode surface waves from dispersion images, we proposed a deconvolution technique for dispersion images. We also changed the MASW computational procedure for retrieving multimode signals in dispersion images.

We applied the deconvolution technique to dispersion images estimated from numerically synthetic data for the simulated model with a low-velocity layer. When two mode components were mixed together and appeared as only one peak in dispersion images, applying the deconvolution technique contributed to separation of the mixed mode peaks at the mode transition point. Although side lobes in dispersion images with the modified MASW are smeared by the effect of anelastic attenuation, higher modes of surface waves are more clearly recognized in the deconvolved images obtained from the modified MASW. Mixing modes were also separated from single peaks with the modified MASW from field data. This result indicates there is a mode transition point at this frequency.

In these examples, we could verify mode transition points estimated by separating mixing modes with deconvolution analysis because fundamental mode signals are observed at frequencies lower than the transition points. However, due to an insufficient source spectrum or poor performance of seismometers for low frequency signals, it might be difficult to retrieve low frequency components. In such conditions, separating mixing modes by the deconvolution analysis contributes to not only improving phase velocity estimations but also identifying mode transition points which are important to prevent mode misidentification.

Table 5.1: Parameter values used in the simulated model.

Layer Number	Thickness (m)	S-wave Velocity (m/s)	P-wave Velocity (m/s)	Density (g/cm^3)
1	3	80	300	1.8
2	7	180	1000	1.8
3	10	120	1400	1.8
4	∞	360	1400	1.8

Table 5.2: Values of quality factors used in anelastic modeling.

Layer Number	Qs	Qp
1	20	40
2	30	60
3	30	60
4	40	80

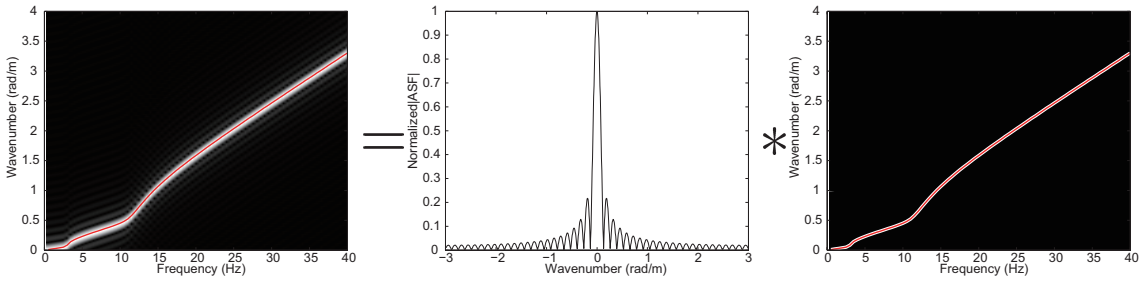

Figure 5.1: The dispersion image (left) obtained by convolution of the absolute values of the ASF with the theoretical spectrum. Red lines are theoretical dispersion curves.

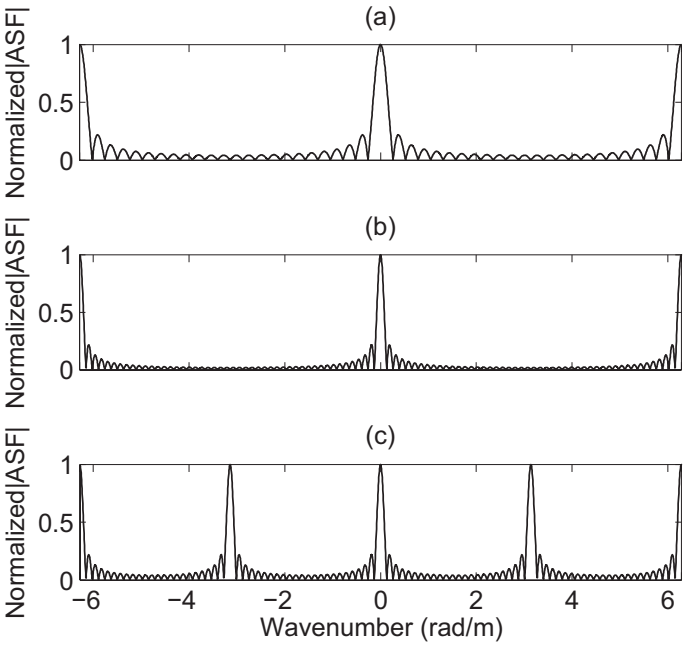

Figure 5.2: Absolute values of the ASF for (a) 24 receivers at intervals of 1 m, (b) 48 receivers at intervals of 1 m, and (c) 24 receivers at intervals of 2 m.

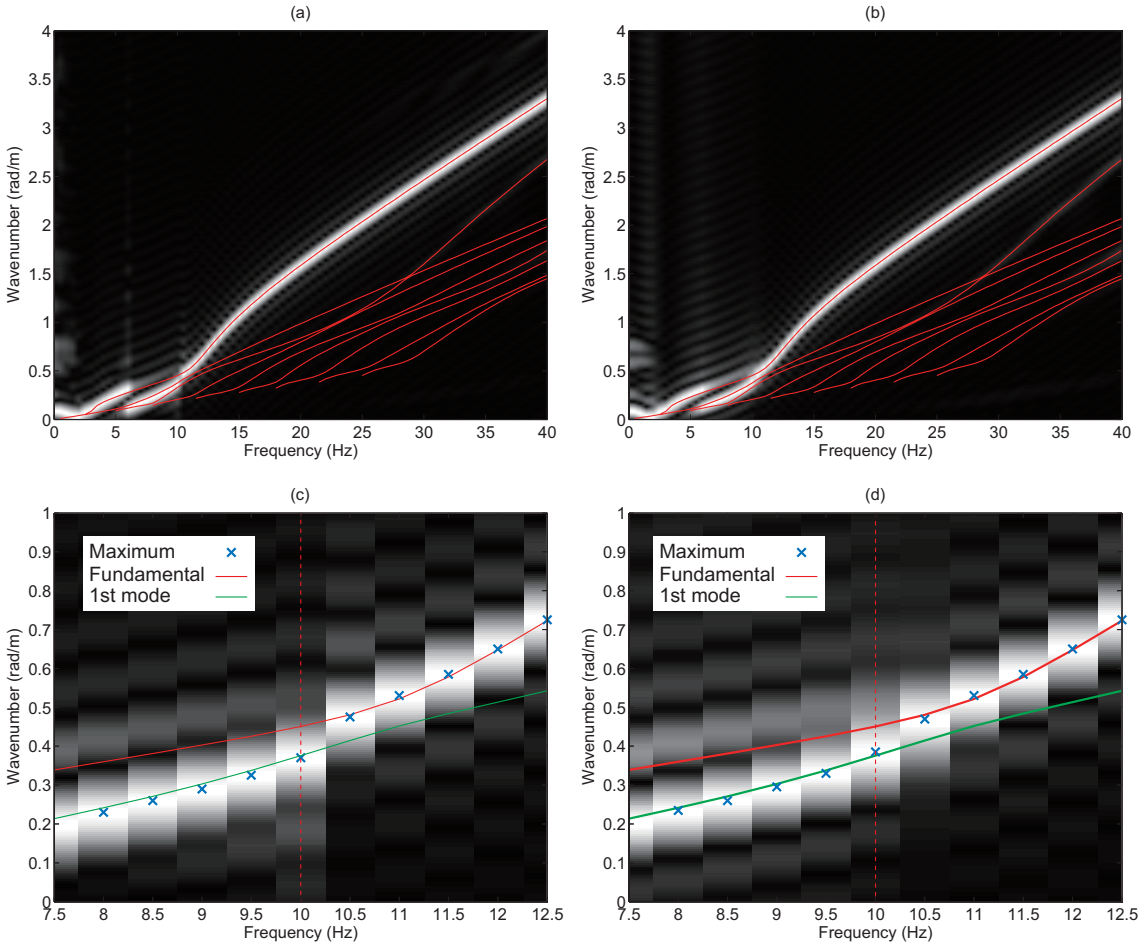

Figure 5.3: Dispersion images obtained from simulated data without consideration of anelastic attenuation, estimated by (a) the MASW and (b) the modified MASW, respectively. Red lines are theoretical dispersion curves up to the eighth higher mode. (c) and (d) are zoomed dispersion images for the MASW and the modified MASW, respectively.

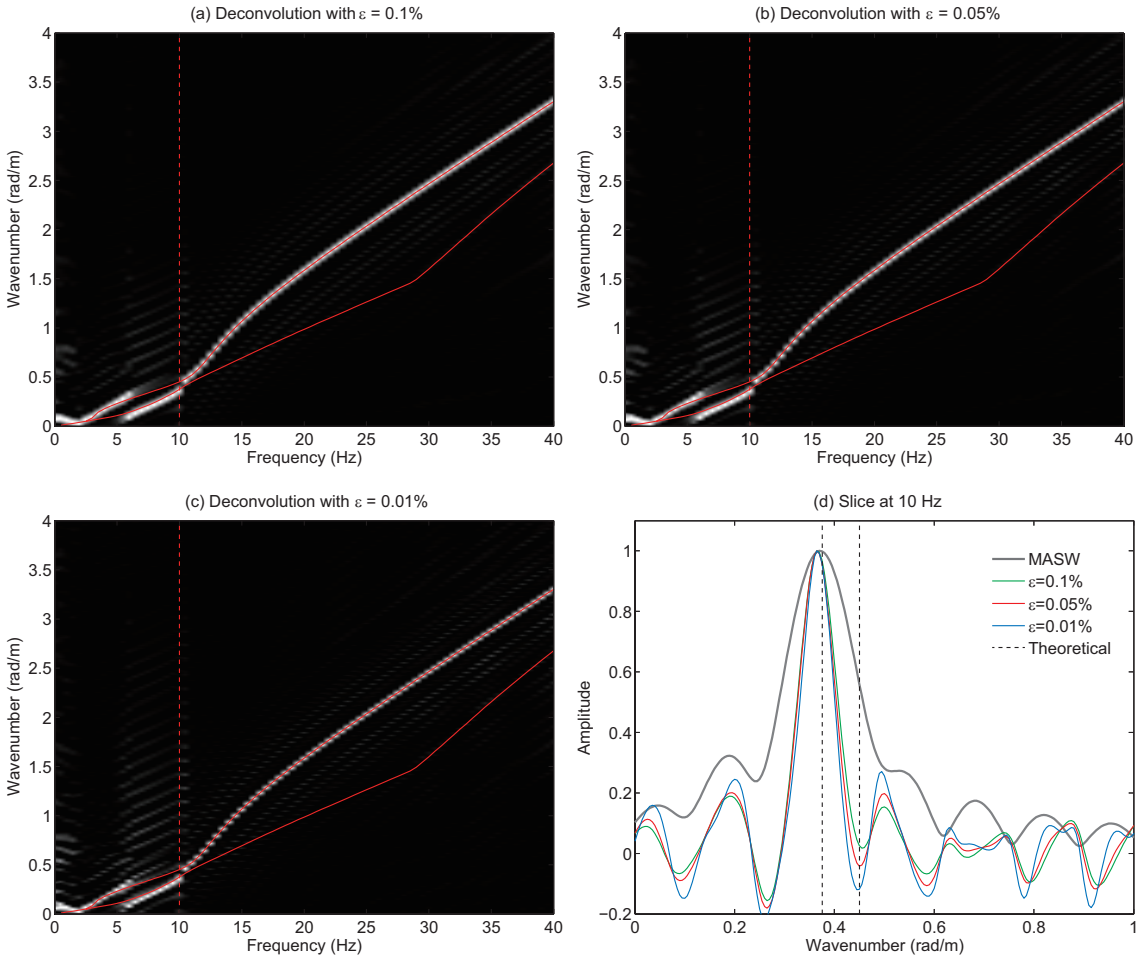

Figure 5.4: Deconvolved images constructed from the dispersion image in Figure 5.3a with the MASW with values of ϵ equal to (a) 0.1 (b) 0.05, and (c) 0.01. (d) A slice of deconvolved images at 10 Hz.

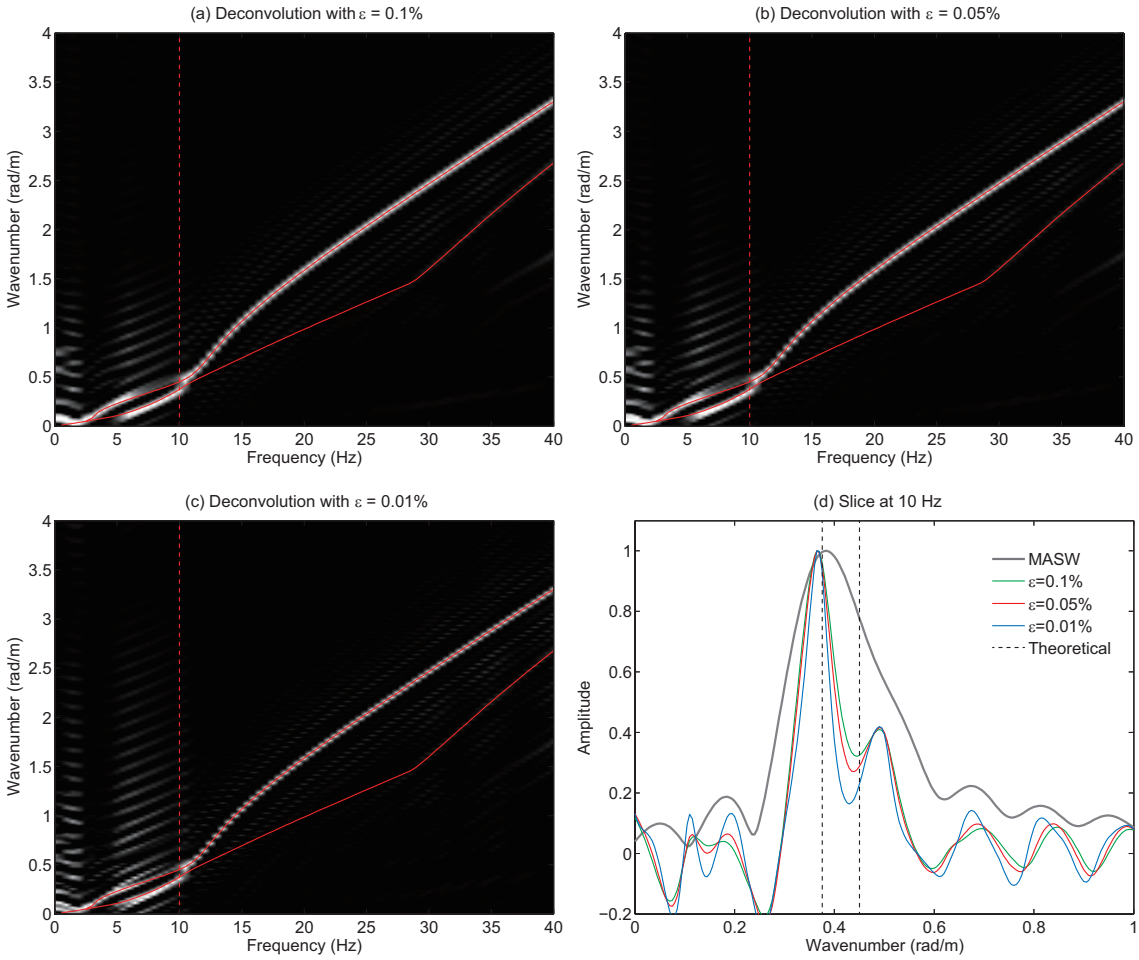

Figure 5.5: Deconvolved images constructed from the dispersion image in Figure 5.3b with the modified MASW with values of ϵ equal to (a) 0.1, (b) 0.05, and (c) 0.01. (d) A slice of the deconvolved images at 10 Hz.

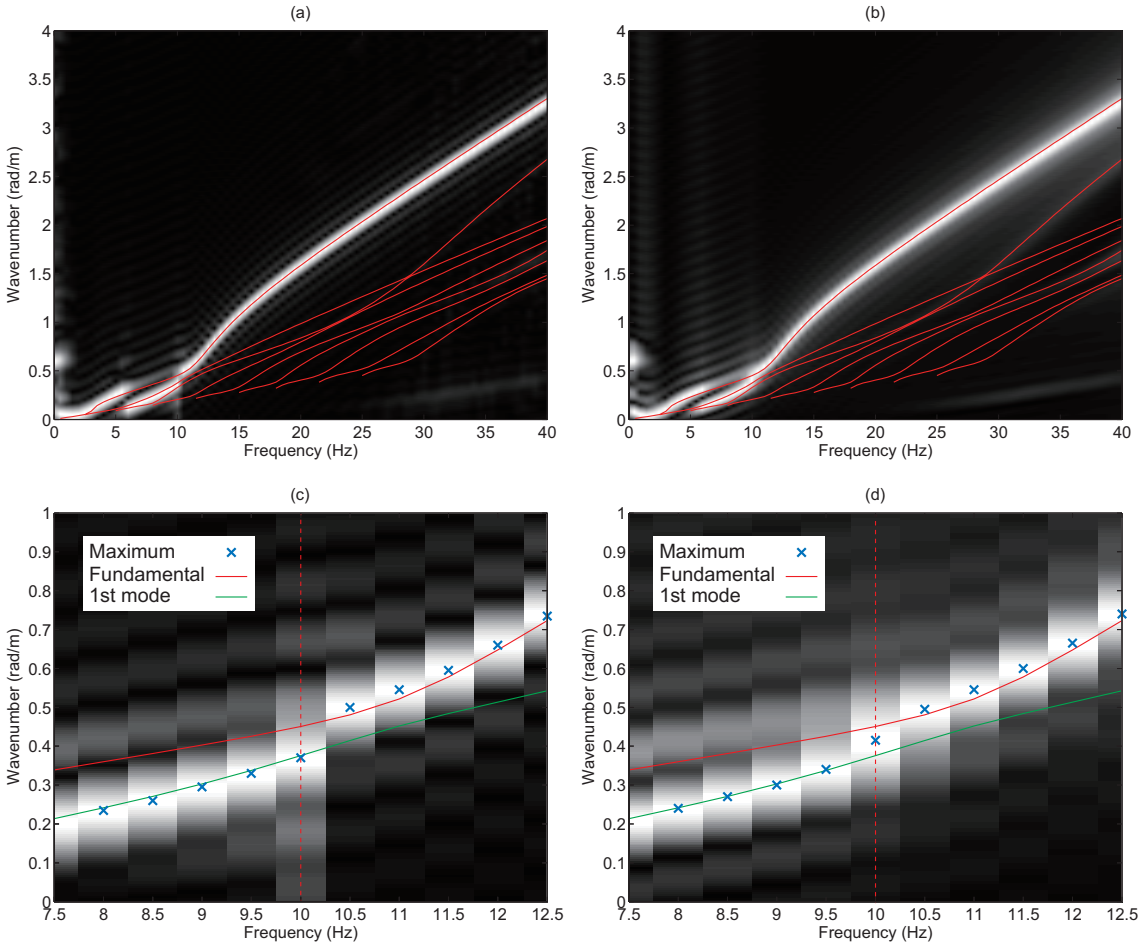

Figure 5.6: Dispersion images obtained from simulated data with anelastic attenuation as in Table 5.1, estimated with (a) the MASW and (b) the modified MASW. Red lines are theoretical dispersion curves up to the eighth higher mode. (c) and (d) are zoomed dispersion images for the MASW and the modified MASW, respectively.

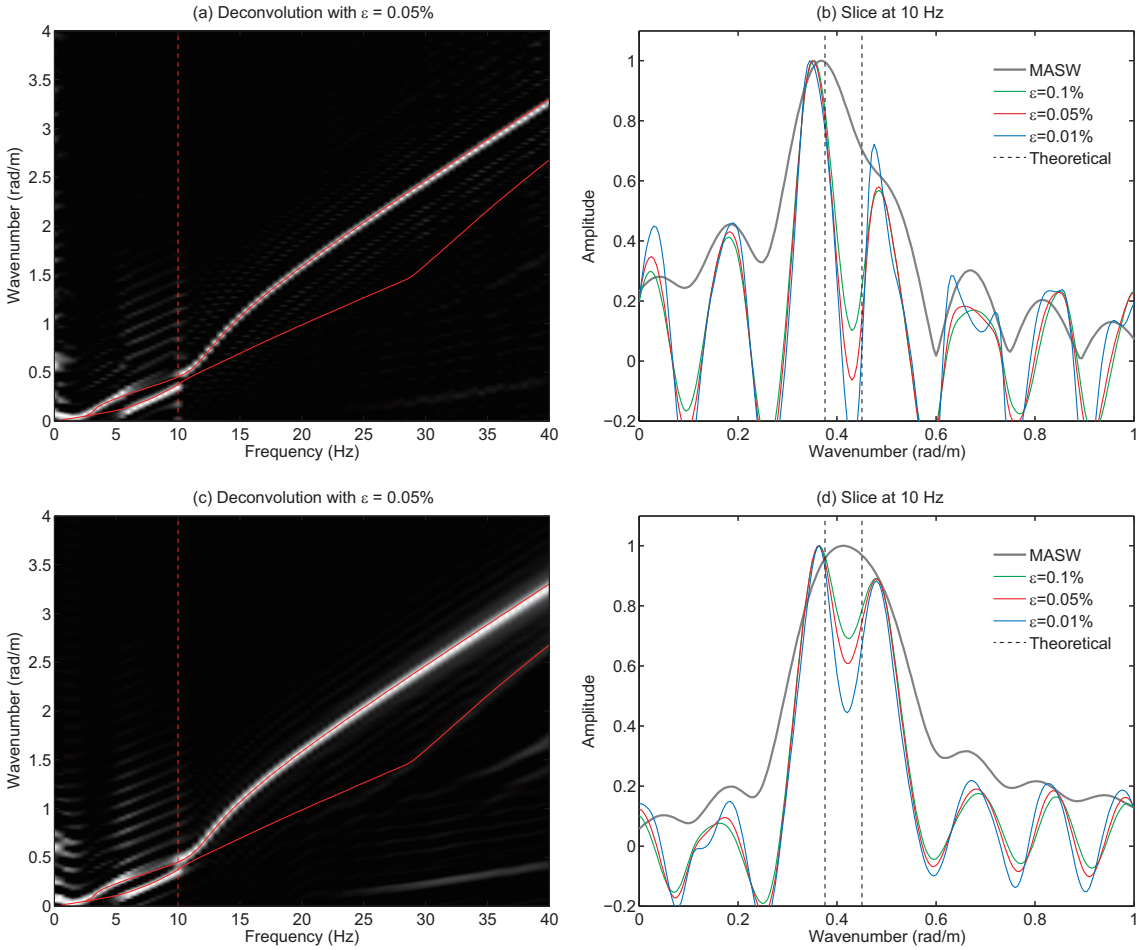

Figure 5.7: Deconvolved images constructed from the dispersion image in Figure 5.6a with the MASW [(a) and (b)] and in Figure 5.6b with the modified MASW [(c) and (d)].

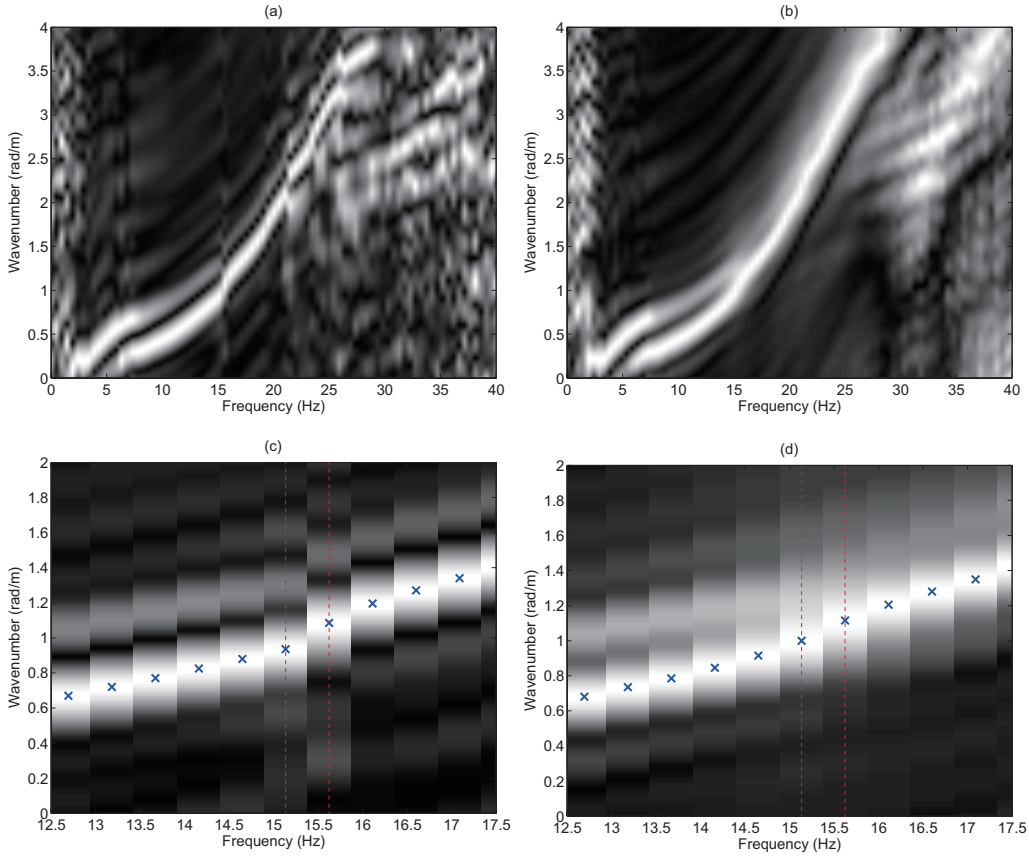

Figure 5.8: Dispersion images of field data estimated with (a) the MASW and (b) the modified MASW. (c) and (d) are zoomed dispersion images for the MASW and the modified MASW, respectively.

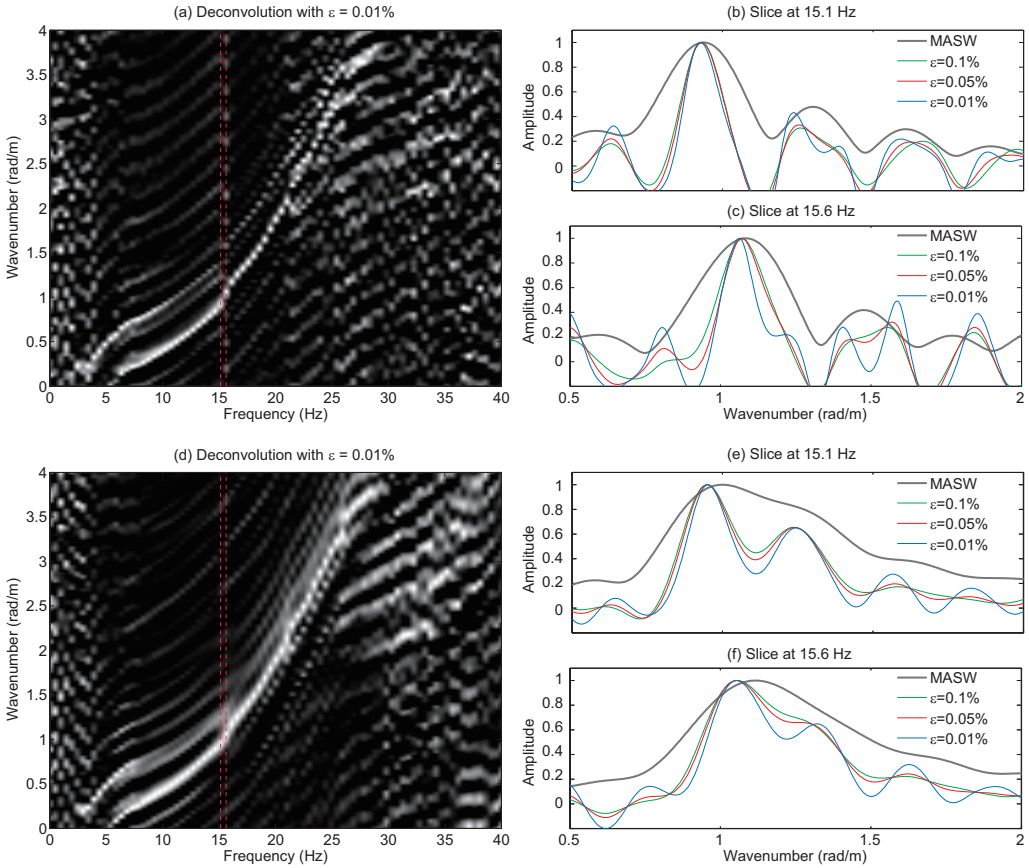

Figure 5.9: Deconvolved images constructed from the dispersion image in Figure 5.8a with the MASW [(a), (b), and (c)] and in Figure 5.8b with the modified MASW [(d) (e), and (f)].

CHAPTER VI

Characteristics of the horizontal component of Rayleigh waves in multimode analysis of surface waves

6.1 Introduction

The surface wave method is a widely applied non-destructive method for estimating subsurface S-wave velocity structures, for example, for mapping bedrock (*Miller et al.*, 1999), soil liquefaction potential (*Lin et al.*, 2004), pavement structures (*Ryden and Lowe*, 2004), and glaciers (*Tsuji et al.*, 2012), and for understanding fault geometry (*Ikeda et al.*, 2013b). *Socco et al.* (2010) provide a comprehensive review of the surface wave analysis technique. In onshore seismic reflection surveys, surface waves are usually considered to be noise and are therefore eliminated. However, once surface waves are identified by a surface wave analysis, they can be used for static corrections to near-surface structures (*Strobbia et al.*, 2010; *Askari et al.*, 2013) or removed from raw data (*Strobbia et al.*, 2011).

Surface waves have different propagation velocities at different frequencies. The propagation mode with the slowest propagation velocity is the fundamental mode, all other propagation modes are referred to as higher modes. Most surface wave analyses use, only the fundamental mode, but it is well known that higher modes

gain in importance if a stiff layer either overlies a soft layer or is embedded between soft layers (e.g. *Gucunski and Woods*, 1992; *Tokimatsu et al.*, 1992b; *Pan et al.*, 2013). The sensitivities of higher modes of surface waves differ from the fundamental mode sensitivity; when the wavelength is the same, higher mode data are more sensitive to S-wave velocities in deeper layers compared with fundamental mode data (*Xia et al.*, 2003; *Luo et al.*, 2007). Therefore, multimode analysis of surface waves can potentially improve the resolution of S-wave velocity estimations and allow the investigation depth to be increased.

Most studies obtain Rayleigh wave dispersion curves from the vertical component of P-SV waves. Very few studies have investigated the horizontal component of Rayleigh waves, which are included in the horizontal (radial) component of P-SV waves. Theoretically, Rayleigh wave dispersion curves for the horizontal component are the same as those for the vertical component. *Dal Moro and Ferigo* (2011) showed, however, that the higher modes of Rayleigh waves estimated from horizontal component data have a different energy distribution compared with those estimated from vertical component data. *Boaga et al.* (2013) also demonstrated that the use of the horizontal component of Rayleigh waves is effective in preventing mode misidentification. These results indicate that the horizontal component of Rayleigh waves plays an important role in multimode analysis of surface waves.

In this paper, we further investigate the characteristics of multimode Rayleigh waves in vertical and horizontal component data to clarify the advantages of using the horizontal component of Rayleigh waves. We conducted a numerical simulation study to reveal the effects of source type and source depth on multimode Rayleigh waves in layered models with and without a low-velocity layer. We then confirmed the findings of the simulation study by applying surface wave analysis to three-component seismic data acquired in Alberta, Canada.

6.2 Methods and results: Multimode Rayleigh waves in multicomponent data

We first conducted a numerical simulation study to reveal the characteristics of multimode Rayleigh waves in multicomponent data. We employed two kinds of layered models, Model A and Model B (Tables 6.1 and 6.2), in the simulation study. Anelastic attenuation was considered by assigning quality factors Q_p and Q_s to each layer. In Model A, P- and S-wave velocities increase with depth. In surface wave exploration, usually only vertical component seismic data are acquired by a vertical source at the surface. It is well known that with this kind of velocity model, the fundamental mode of surface waves is dominant at most frequencies in the data acquisition. In contrast, when a low-velocity layer is embedded among the layers as in Model B, higher modes of surface waves have large amplitudes in seismic data acquired in a near-surface seismic survey (e.g. *Tokimatsu et al.*, 1992b; *Pan et al.*, 2013). Here, we employed the discrete wavenumber integral method (*Bouchon and Aki*, 1977) to calculate synthetic waveforms for the simulated models. In the simulations, 48 receivers set from 18 to 300 m from the source at a spacing of 6 m were assumed. The source function was an 8-Hz Ricker wavelet, and the time duration was 8 s.

To estimate Rayleigh wave dispersion curves from the vertical and horizontal (radial) components of numerically synthesized waveforms, we performed a multichannel analysis of surface waves (MASW) (*Park et al.*, 1998, 1999a). In the MASW method, seismic data in the time-offset (t-x) domain are transformed into the frequency-offset (f-x) domain by a Fourier transform. The dispersion image in the velocity-frequency (c-f) domain is then obtained by stacking seismic data in the f-x domain over offset x with a phase shift.

6.2.1 Model A

6.2.1.1 Comparison of source types

We investigated the effects of source type on multimode Rayleigh waves in Model A by using a vertical force and an explosive source are used as sources. The vertical force simulates a sledge hammer, a vibrator, or an impactor used in a near-surface seismic survey, whereas the explosive source simulates a dynamite source used in a large-scale seismic reflection survey.

Figure 6.1 shows simulated waveforms and corresponding dispersion images estimated by MASW for vertical and horizontal component data when the vertical force was located 1 m below the surface. The theoretical dispersion curves shown in Figure 6.1 were computed by the compound matrix method (*Saito*, 1988; *Saito and Kabasawa*, 1993; *Ikeda and Matsuoka*, 2013). For easy visualization, phase velocities with maximum amplitude are plotted for each frequency. Note that the phase velocities with second or third maximum for each frequency can be used in an inversion analysis if they have a continuous dispersion trend. The wavelengths detectable by surface wave analysis depend mainly on the distance between the minimum and maximum offsets (spread length). In this study, we picked wavelengths up to twice as long as the spread length.

It is apparent that surface waves are dominant in the simulated data. The estimated dispersion curves are mostly consistent with the theoretical dispersion curve of the fundamental mode. The energy of the dispersion curve estimated from the horizontal component is shifted to the first higher mode at 2 Hz. Figure 6.2 shows theoretical Rayleigh wave ellipticities and the vertical and horizontal amplitude responses up to the third higher mode for a vertical force at the surface. The amplitude response of the fundamental mode is dominant in the vertical component. In the horizontal component, however, the amplitude response of the first higher mode

is dominant at about 2 Hz because the trough of the Rayleigh wave ellipticity for the fundamental mode at this frequency causes the amplitude of the fundamental mode in the horizontal component to be low. This result is consistent with the mode transition in the dispersion curve at 2 Hz in the horizontal component data.

Figure 6.3 shows simulated waveforms and estimated dispersion images for an explosive source buried at 1 m depth. Compared to the results for the vertical force, higher mode components have slightly larger amplitudes, although the fundamental mode is dominant in the vertical component data. In the horizontal component, the energy of the first higher mode is dominant over a wider frequency range than was the case with the vertical force, and the second higher mode is also dominant at about 5 Hz (Figure 6.3b).

6.2.1.2 Comparison of source depths

Explosive sources (e.g., dynamite) are usually buried under ground so that the explosive energy will be transferred to the geological formation. In our simulations, we therefore set explosive sources at depths of 8 and 15 m to evaluate the effect of source depth. Figures 6.4 and 6.5 show the simulated waveforms and estimated dispersion curves when the explosive sources were set at 8 and 15 m depth, respectively. In the vertical component data, the body waves had larger amplitudes at the greater source depth. Therefore, we muted the body waves in the vertical component data before applying MASW (red lines in Figures 6.4a and 6.5a). When the source was located at 8 m depth, a number of higher mode signals could be clearly identified in the horizontal component data at high frequencies, whereas the fundamental mode was dominant in the vertical component data. Higher mode signals were larger in both the horizontal and vertical components when the source was buried at 15 m depth. However, the modes and their frequency ranges extracted from the horizontal component data differed from those extracted from the vertical component data.

These results demonstrate that additional mode information can be extracted when horizontal component data are used along with vertical component data. Note that several observed phase velocities exceeded the maximum S-wave velocity of the simulated model (1500 m/s); these might be explained by guided P-waves (*Boiero et al.*, 2013).

6.2.2 Model B

6.2.2.1 Comparison of source types

Figure 6.6 shows simulated waveforms and estimated dispersion images for Model B when a vertical force was located at 1 m depth. Surface wave signals are dominant in the synthesized data. A smooth mode transition can be observed in the estimated dispersion curves of both components. These features are typical when a low-velocity layer is embedded among the layers (e.g. *Tokimatsu et al.*, 1992b; *Pan et al.*, 2013).. However, the dominant modes and transit frequencies in the horizontal component data differ slightly from those in the vertical component data. Figure 6.7 shows the theoretical Rayleigh wave ellipticities, and the vertical and horizontal amplitude responses for a vertical force at the surface. The mode transition of the vertical component data is consistent with that of the vertical amplitude response (Figure 6.7b). At about 2 Hz, the horizontal amplitude response of the fundamental mode suddenly decreases and the first higher mode becomes dominant, because of the trough in the Rayleigh wave ellipticity of the fundamental mode at this frequency (Figures 6.7a and 6.7d). Therefore, the fundamental mode vanishes at about 2 Hz in the horizontal component data. The mode transition in the dispersion image at 7.5 Hz also agrees with the horizontal amplitude response (Figure 6.7e).

Figure 6.8 shows simulated waveforms and estimated dispersion images when the explosive was set at 1 m depth. Although the transit frequencies are slightly different from the results obtained with the vertical force, similar mode transitions are

observed.

6.2.2.2 Comparison of source types

Figures 6.9 and 6.10 show simulated waveforms and estimated dispersion images when the explosive sources were set at 8 and 15 m depths, respectively. When the source was at 8 m depth, the dispersion image estimated from the vertical component data is similar to that estimated when the explosive source was at 1 m depth (Figure 6.8a). In contrast, in the horizontal component data, the dominant modes are shifted to higher order modes with high phase velocities. When the source location was at 15 m depth, we muted the strong body waves in the vertical component data (red line in Figure 6.10a). The modes extracted from the vertical component data are shifted to higher order modes but it is apparent that in horizontal component data the higher modes have larger amplitudes with higher phase velocities, compared to the vertical component data. Thus, additional mode information can also be extracted from the horizontal component data with Model B.

6.3 Field example

We next applied a surface wave analysis to field data and compared the extracted characteristics of the multicomponent Rayleigh waves inferred from the simulation study.

6.3.1 Data acquisition

The field data were originally acquired for monitoring P-wave velocity changes associated with steam-assisted gravity drainage in Alberta, Canada, by Japan Canada Oil Sands Limited in 2002 and 2006 (*Kato et al.*, 2008; *Nakayama et al.*, 2008). We applied a surface wave analysis to a shot gather of field data acquired in 2006. Figure 6.11 shows the position of the source and the configuration of the receivers around

the source. The receivers were three-component digital sensors incorporating micro-electro-mechanical systems technology. The sampling interval was 1 ms and the record length was 3 s. The dynamite source (0.l25 kg) was at 15 m depth. This source configuration is similar to that for Models A and B with an explosive source at 15 m depth (Figures 6.5 and 6.10) in the simulation study. Although the maximum offset between source and receivers was 815 m, we used only the receivers within 300 m from the source because of the 3-s record length.

6.3.2 Dispersion curve estimations

We assumed that this field had a horizontally layered structure, and estimated one dispersion image from the seismic data acquired by the two-dimensionally distributed receivers (Figure 6.11) to improve the signal-to-noise ratio by stacking multiple receivers in the MASW. We obtained the two horizontal components of the P-SV waves and SH waves by converting the coordinatse of the two horizontal components of north-south and east-west by considering the geometry between the source and receivers. The observed shot gathers and dispersion images estimated by MASW for the vertical and horizontal components of the P-SV waves are shown in Figure 6.11. No Love waves were observed in the dispersion image of the horizontal component of the SH waves (not shown) because SH waves are not produced by an explosive source. Two modes can be clearly observed in the vertical component data, whereas higher order modes can be observed in the horizontal component data.

Figure 6.13 shows the extracted dispersion curves of the two low-order modes for each component. Because of the continuity of the observed dispersion curves, the mode of the dispersion curve with higher phase velocities in the vertical component data should be identical to the mode with lower phase velocities in the horizontal component data. At low frequencies, the observed phase velocities include uncertainty because their wavelengths are between one and two times the spread length (orange

lines in Figure 6.13). The higher order mode extracted from the horizontal component data could not be extracted from the vertical component data. Thus, additional mode information was obtained by using the horizontal component data of the P-SV waves. These characteristics of vertical and horizontal component data of multimode Rayleigh waves agree with the Model A simulation performed with the same source configuration (i.e., an explosive source at 15 m depth) (Figure 6.5).

6.4 Discussion

The results of the simulation study and field example indicate that analysis of the horizontal component of the Rayleigh waves allows additional higher order mode information to be extracted when the explosive source is buried. Although the use of a buried explosive source and three-component receivers is not common in near-surface seismic surveys, it is possible to extract multimode Rayleigh waves from multicomponent data originally acquired for large-scale seismic reflection seismic surveys as shown in the previous section. Constructing near-surface velocity models by a surface wave analysis can help improve static corrections in seismic reflection surveys (*Strobbia et al.*, 2010; *Boiero et al.*, 2013; *Askari et al.*, 2013).

To assess the importance of extracting multimode Rayleigh waves from both vertical and horizontal component data when the explosive source is at 15 m depth, we investigated the sensitivity of multimode dispersion curves of the simulation models to S-wave velocity changes. We compared theoretical dispersion curves obtained by changing the S-wave velocities within a range of $\pm$ 10% in each layer. Figures 6.14 and 6.15 show the results of sensitivity analyses for Models A and B, respectively.

Only continuous phase velocities were extracted from the estimated dispersion images. With both models, higher modes of Rayleigh waves showed larger sensitivity to S-wave velocity changes, compared to the fundamental mode. With Model A, the dispersion curves of the first higher mode extracted from the horizontal component

data showed sensitivity to S-wave velocity changes in the first and third layers, although the phase velocities estimated from vertical component data showed a small sensitivity to velocity changes in the third layer. With Model B, phase velocities extracted from the vertical component data were mostly sensitive to S-wave velocity changes in the first and second layers. However, higher modes extracted from the horizontal component data showed sensitivity to velocity changes in the third layer as well as in the first and second layers.

These results demonstrate that multimode Rayleigh waves extracted from vertical and horizontal component data have the potential for improving S-wave velocity estimations. A number of authors have demonstrated that the use of multimode surface waves in inversions can improve S-wave velocity estimations (e.g. *Xia et al.*, 2003; *Luo et al.*, 2007). Although there is ambiguity in the numbering of the observed modes among studies, several inversion techniques can be efficiently applied without mode identification (e.g. *Forbriger*, 2003; *O'Neill et al.*, 2003; *Ryden and Park*, 2006; *Maraschini et al.*, 2010; *Socco et al.*, 2011; *Boiero et al.*, 2013). Higher modes extracted from both vertical and horizontal component data could thus be used to improve S-wave velocity estimations obtained by using appropriate multimode inversion techniques.

6.5 Conclusions

To examine the utility of horizontal component data of Rayleigh waves, which are usually neglected in surface wave analyses, we investigated the characteristics of both the horizontal and vertical components of multimode Rayleigh waves. The inferred characteristics of multimode Rayleigh waves suggest that the use of multimode Rayleigh waves for retrieving complex S-wave velocity structures should be encouraged.

First, we conducted a numerical simulation study by using layered models with and

without a low-velocity layer to examine the effects of source type and source depth on both components of multimode Rayleigh waves. When the source was located near the surface, the dispersion curves extracted from the horizontal component data differed from those of the vertical component data, but the difference is small except at low frequencies. However, in both simulation models, higher order modes were dominant, especially in horizontal component data, when the source depth of an explosive source was increased. The component characteristics obtained by the simulations were also observed in field data acquired by three-component receivers with a buried dynamite source. The both simulation and field studies demonstrated that additional mode information of Rayleigh waves can be extracted by the use of horizontal component data acquired by an explosive source at depth. Sensitivity analysis of S-wave velocity changes revealed that higher modes extracted from horizontal component data can potentially increase the sensitivity of the analysis for to layers for which the sensitivity of the vertical component data is small.

Data acquisition using an explosive source and three-component receivers is not common in surface seismic survey. However, there are many existing data sets from large-scale seismic reflection surveys that were acquired in this way. By using an appropriate multimode inversion technique, we can efficiently use the horizontal component of multimode Rayleigh waves when constructing near-surface S-wave velocity models for static corrections in analyses of seismic reflection data.

Table 6.1: Parameters of Model A.

Layer No.	Thickness (m)	S-wave Velocity (m/s)	P-wave Velocity (m/s)	Q_s	Q_p	Density (g/cm^3)
1	30	200	1000	20	40	1.6
2	50	350	1500	30	60	1.8
3	100	600	2000	50	100	2.0
4	∞	1500	3000	75	150	2.2

Table 6.2: Parameters of Model B.

Layer No.	Thickness (m)	S-wave Velocity (m/s)	P-wave Velocity (m/s)	Q_s	Q_p	Density (g/cm^3)
1	30	350	1500	30	60	1.8
2	20	200	1000	20	40	1.6
3	75	600	2000	50	100	2.0
4	∞	1500	3000	75	150	2.2

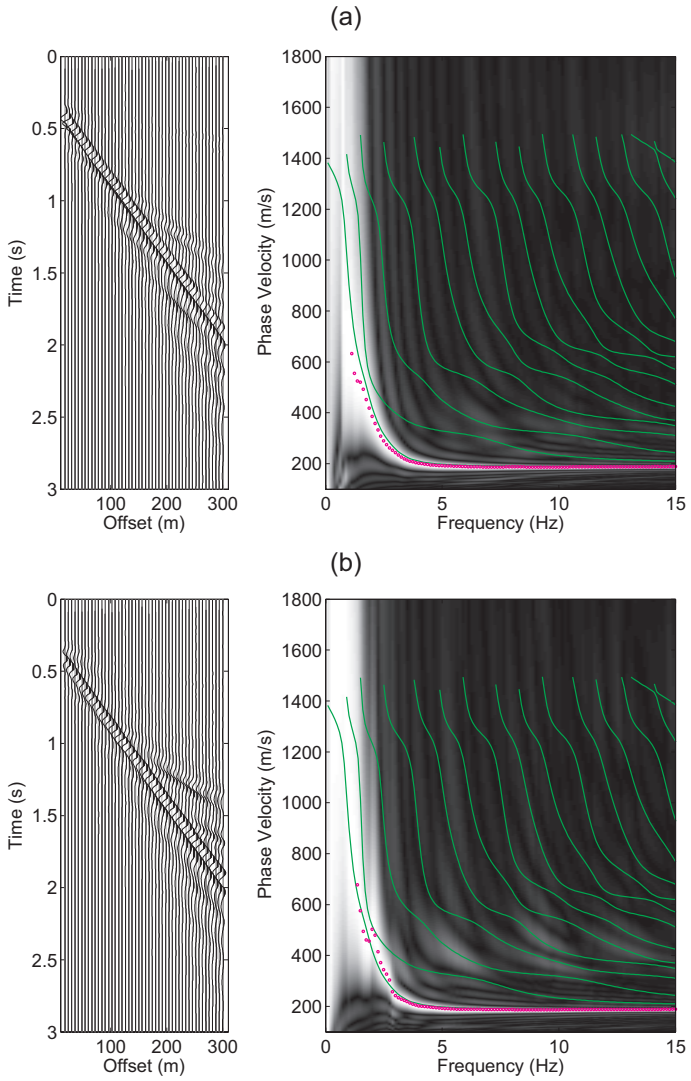

Figure 6.1: The 30-Hz low-pass-filtered synthesized waveforms and dispersion images for (a) vertical and (b) horizontal component data when the vertical force was located at 1 m depth in Model A. Magenta circles are phase velocities with maximum amplitude for each frequency, and green lines are theoretical dispersion curves.

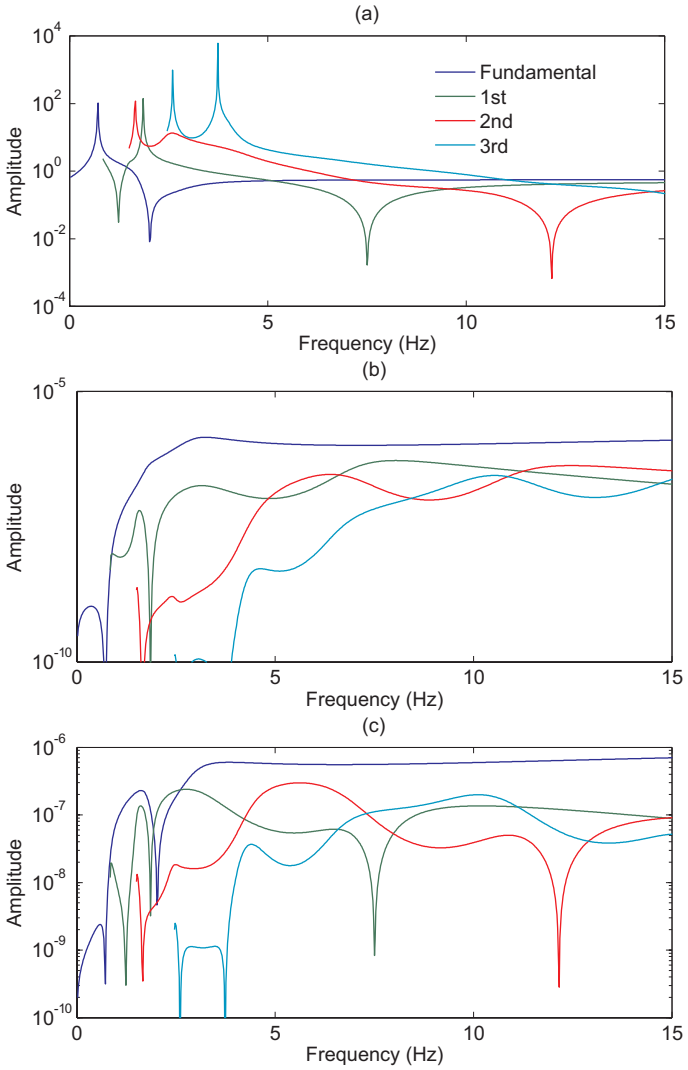

Figure 6.2: (a) Theoretical Rayleigh wave ellipticities and (b) vertical and (c) horizontal amplitude responses up to the third higher mode for Model A.

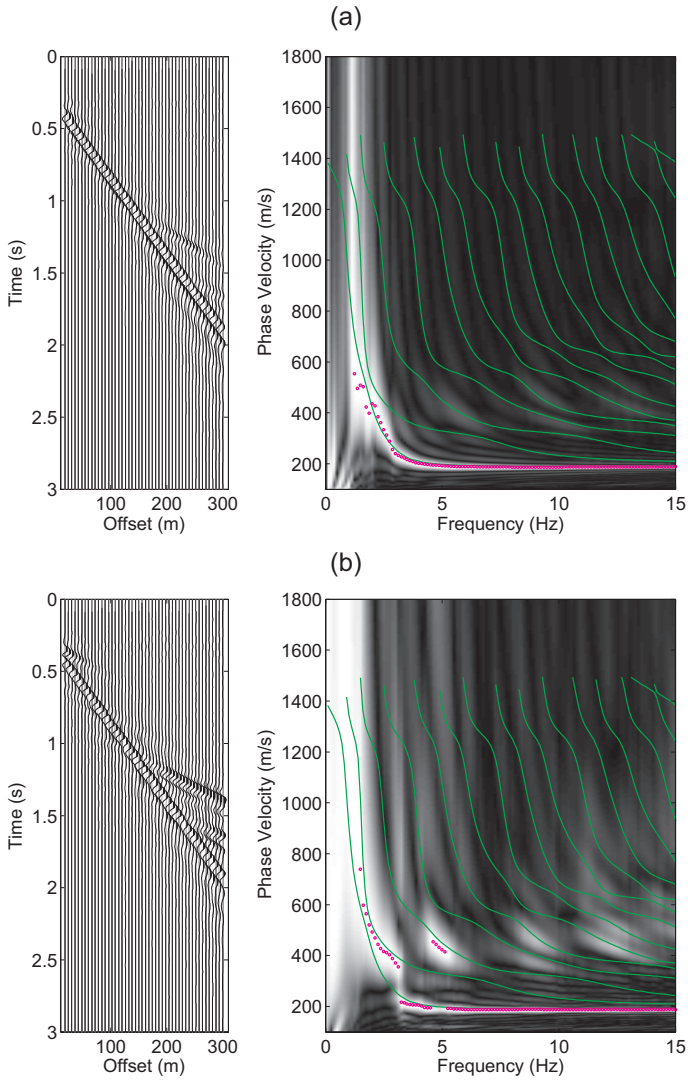

Figure 6.3: The 30-Hz low-pass-filtered synthesized waveforms and dispersion images for (a) vertical and (b) horizontal component data when the explosive source was located at 1 m depth in Model A. Magenta circles are phase velocities with maximum amplitude for each frequency and green lines are theoretical dispersion curves.

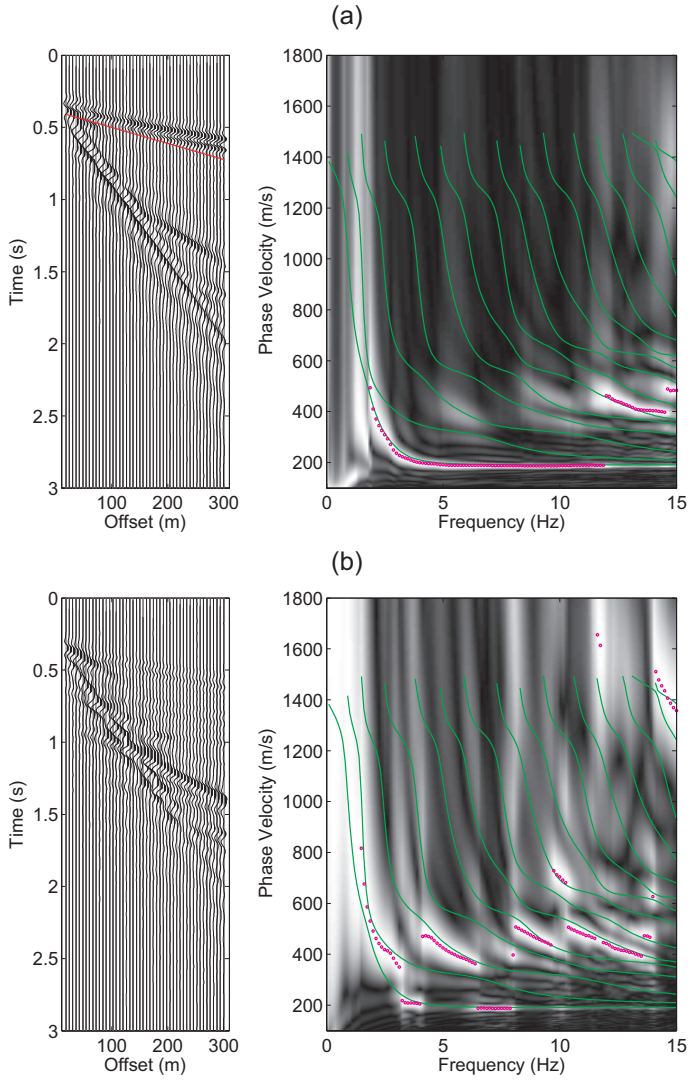

Figure 6.4: The 30-Hz low-pass-filtered synthesized waveforms and dispersion images for (a) vertical and (b) horizontal component data when the explosive source was located at 8 m depth in Model A. Body waves of the vertical component data are muted (red line). Magenta circles are phase velocities with maximum amplitude for each frequency, and green lines are theoretical dispersion curves.

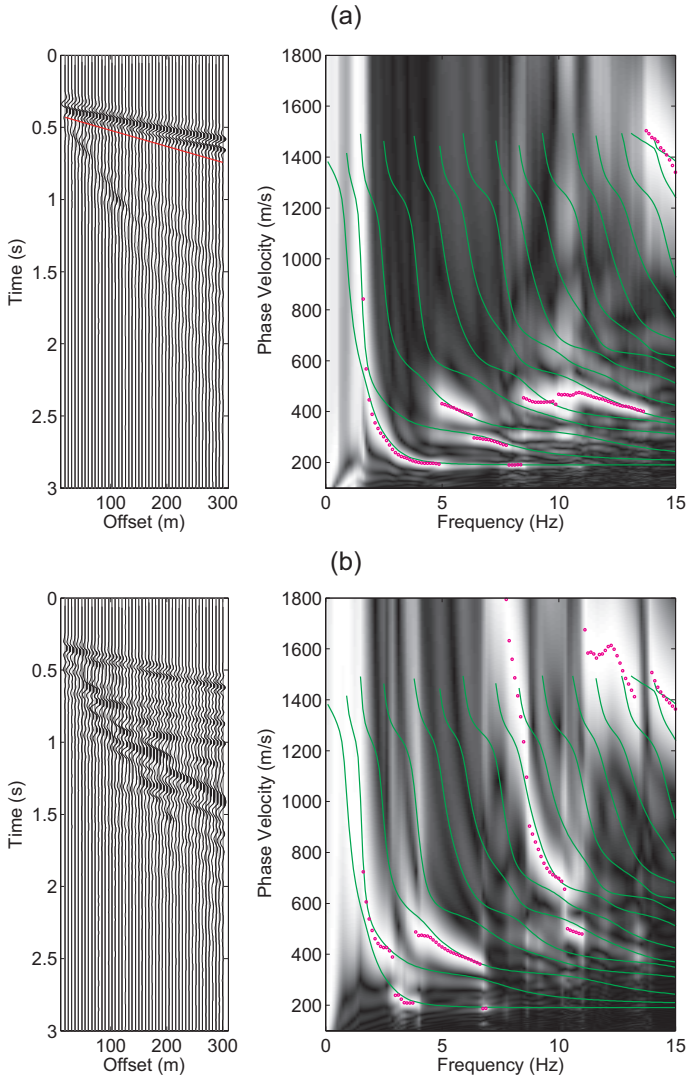

Figure 6.5: The 30-Hz low-pass-filtered synthesized waveforms and dispersion images for (a) vertical and (b) horizontal component data when the explosive source was located at 15 m depth in Model A. Body waves of the vertical component data are muted (red line). Magenta circles are phase velocities with maximum amplitude for each frequency, and green lines are theoretical dispersion curves.

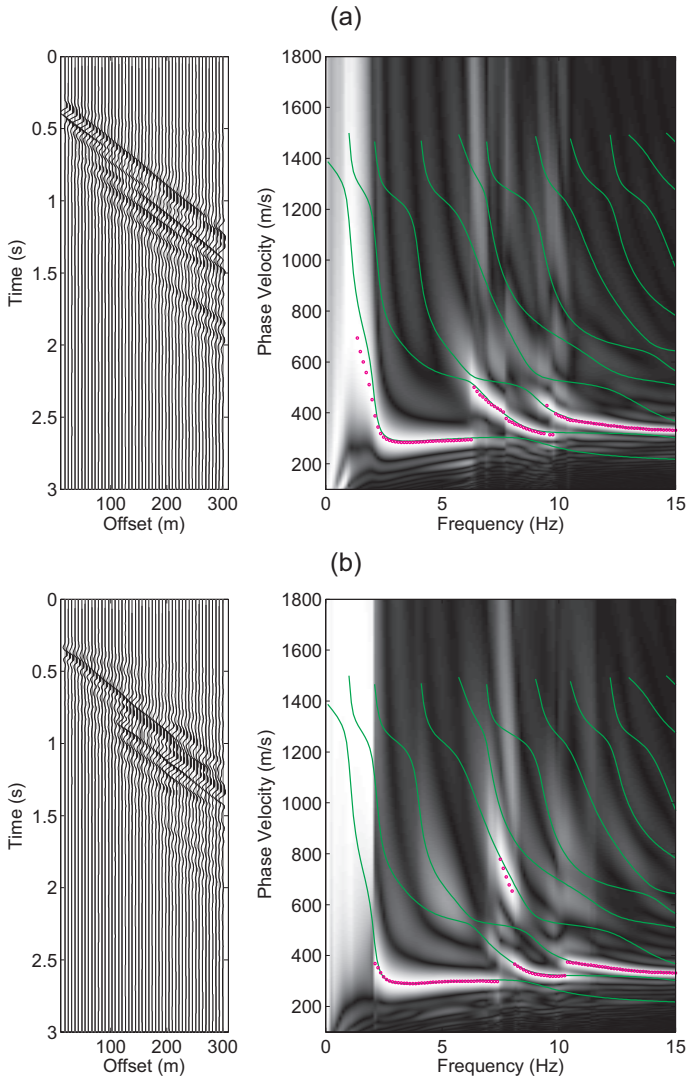

Figure 6.6: The 30-Hz low-pass-filtered synthesized waveforms and dispersion images for (a) vertical and (b) horizontal component data when the vertical force was located at 1 m depth in Model B. Magenta circles are phase velocities with maximum amplitude for each frequency and green lines are theoretical dispersion curves.

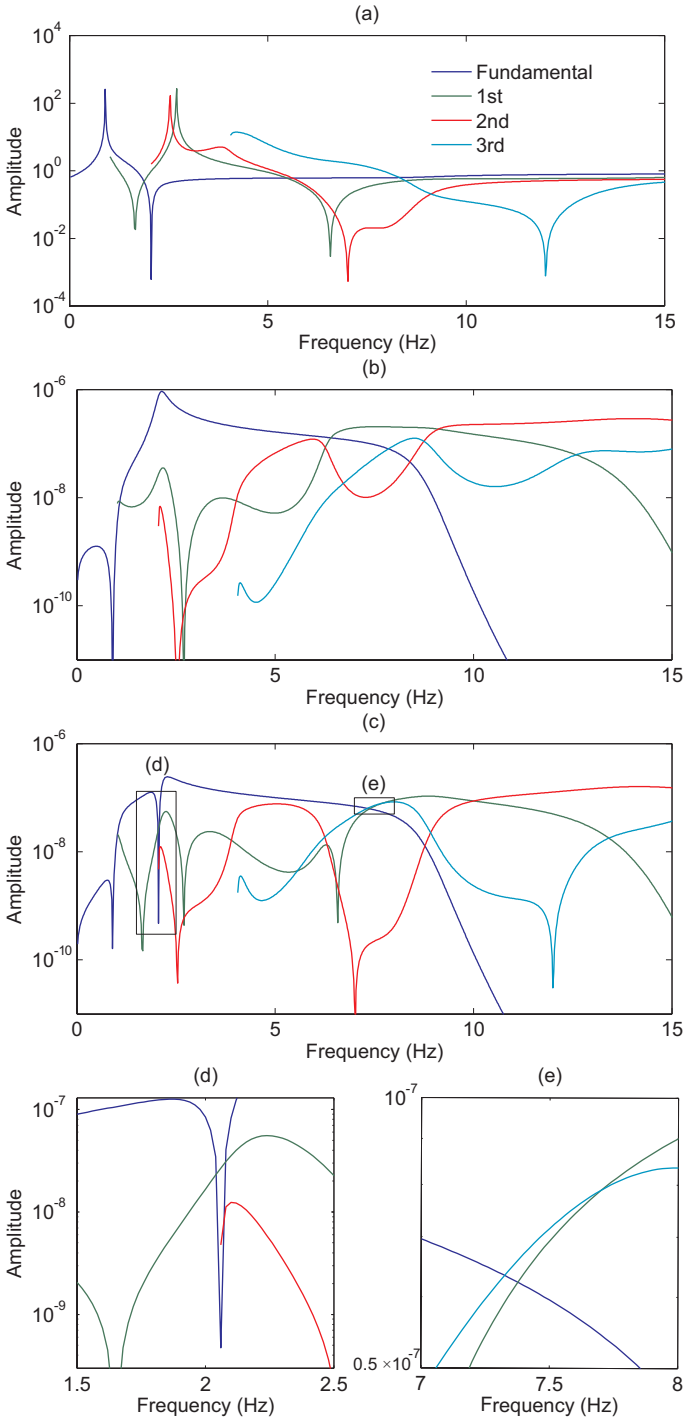

Figure 6.7: (a) Theoretical Rayleigh wave ellipticities and (b) vertical and (c) horizontal amplitude responses up to the third higher mode for Model B. (d) and (e) Enlarged view of the horizontal amplitude responses.

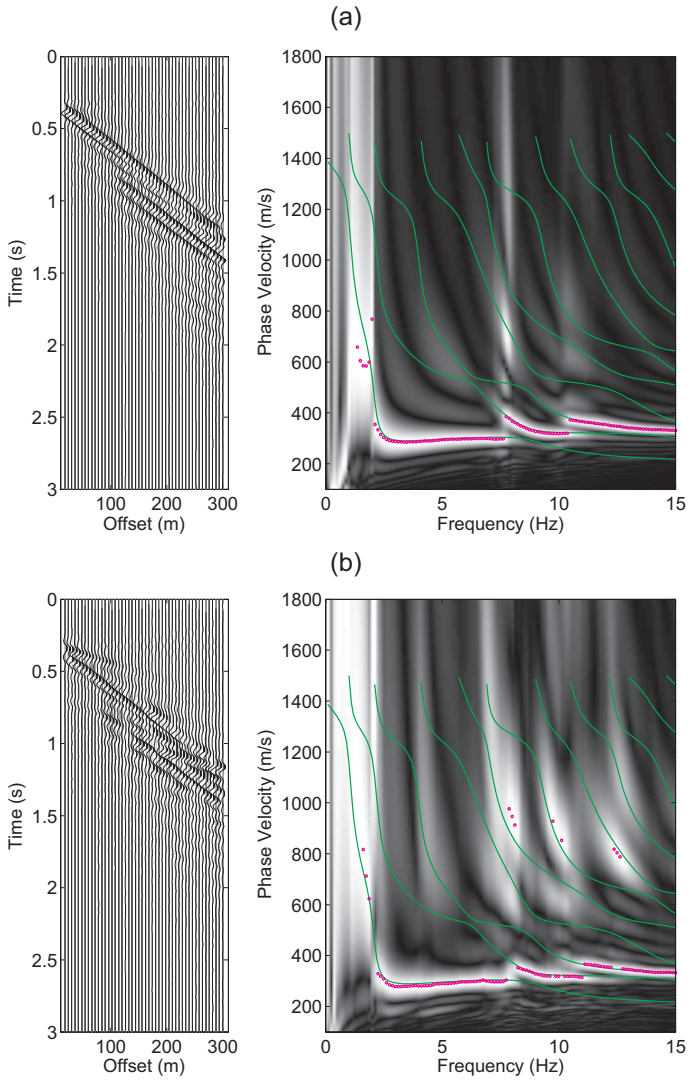

Figure 6.8: The 30-Hz low-pass-filtered synthesized waveforms and dispersion images for (a) vertical and (b) horizontal component data when the explosive source was located at 1 m depth in Model B. Magenta circles are phase velocities with maximum amplitude for each frequency and green lines are theoretical dispersion curves.

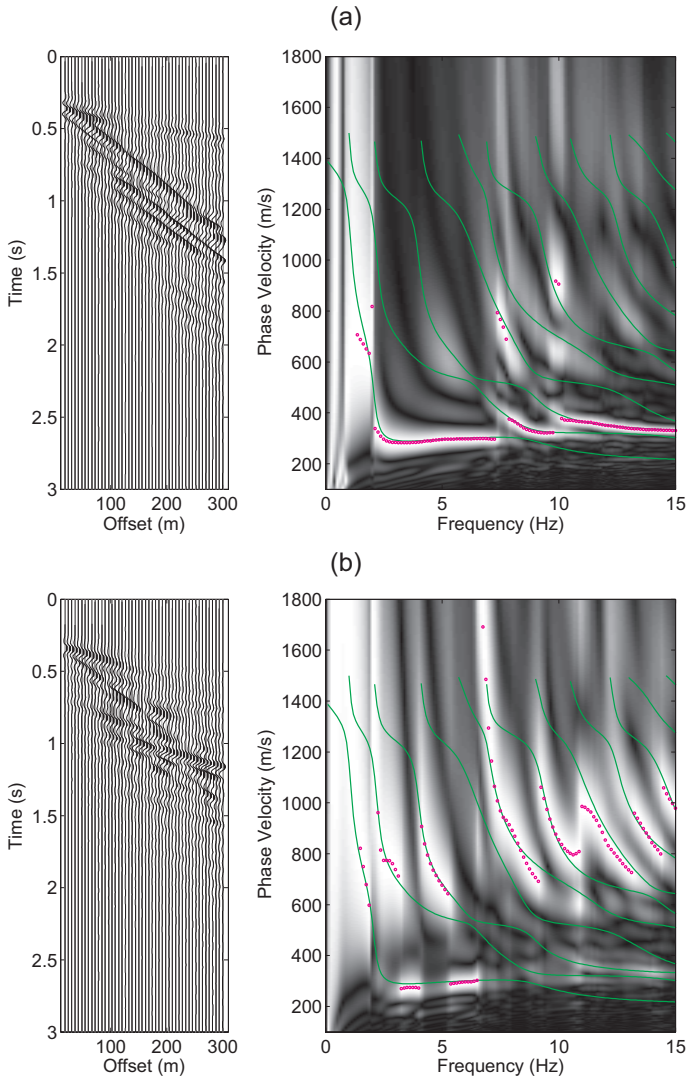

Figure 6.9: The 30-Hz low-pass-filtered synthesized waveforms and dispersion images for (a) vertical and (b) horizontal component data when the explosive source was located at 8 m depth in Model B. Magenta circles are phase velocities with maximum amplitude for each frequency and green lines are theoretical dispersion curves.

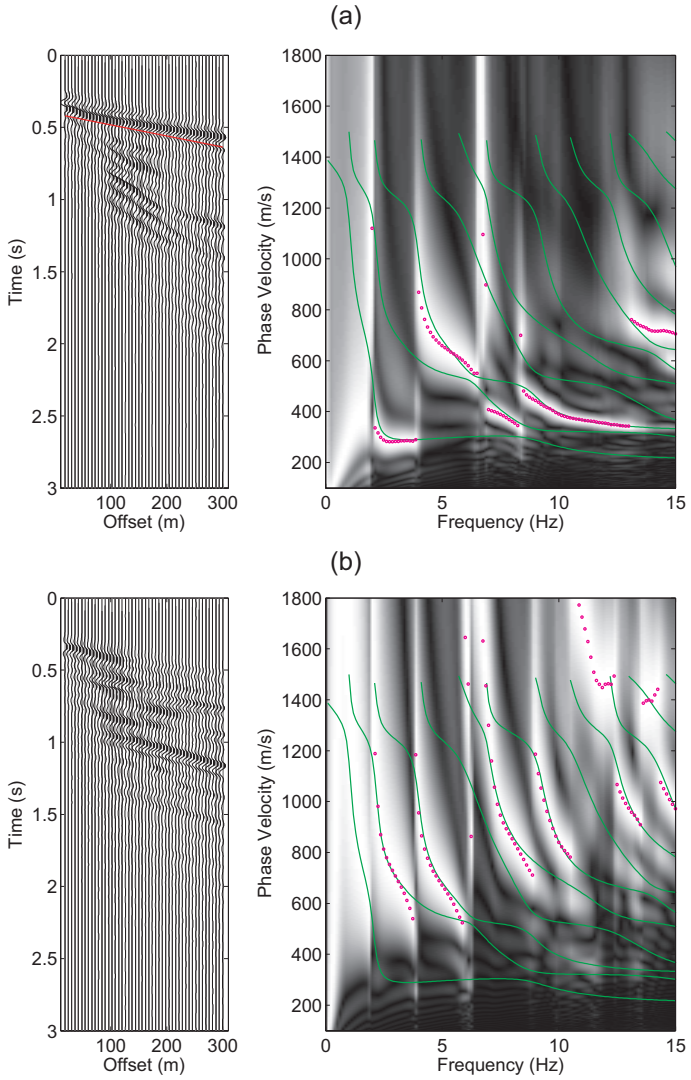

Figure 6.10: The 30-Hz low-pass-filtered synthesized waveforms and dispersion images for (a) vertical and (b) horizontal component data when the explosive source was located at 15 m depth in Model B. Body waves of the vertical component data are muted (red line). Magenta circles are phase velocities with maximum amplitude for each frequency, and green lines are theoretical dispersion curves.

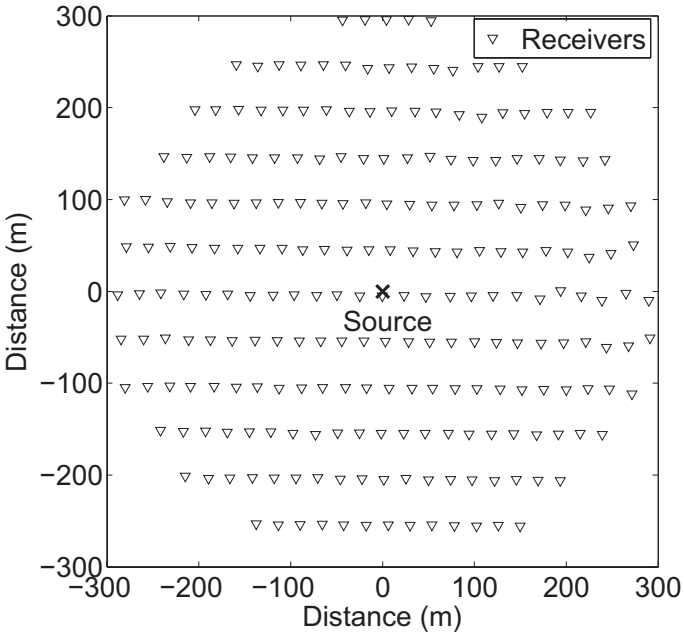

Figure 6.11: Positions of the source and the receivers used in the surface wave analysis.

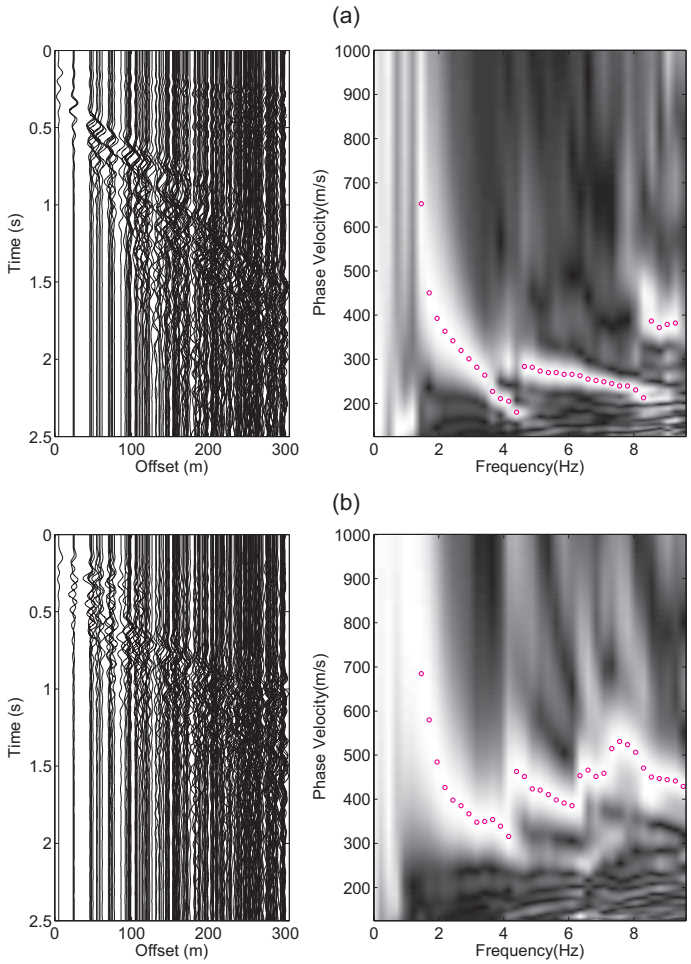

Figure 6.12: The 10-Hz low-pass-filtered seismic data and dispersion images for (a) vertical and (b) horizontal component data. Magenta circles are phase velocities with maximum amplitude for each frequency.

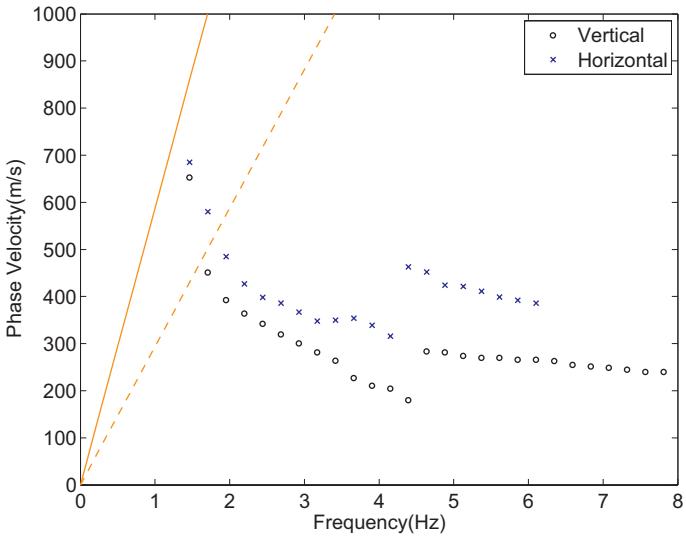

Figure 6.13: Estimated dispersion curves for the lower two modes in the vertical and horizontal component data. The solid line represents a wavelength twice as long as the spread length, and the dashed line represents a wavelength the same length, and the dashed line represents a wavelength the same length as the spread length.

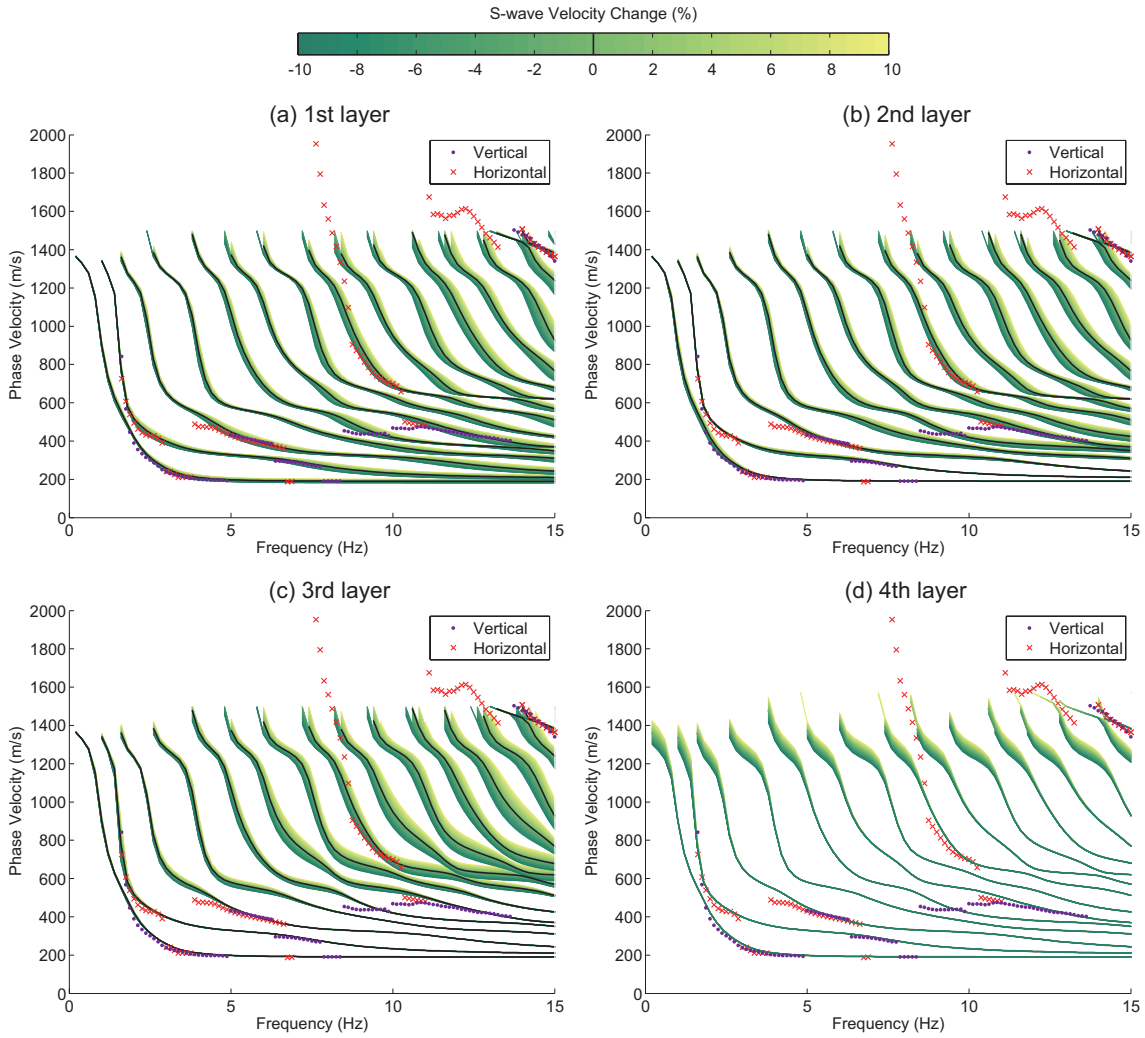

Figure 6.14: Sensitivity analysis results for the (a) first, (b) second, (c) third, and (d) fourth layers of Model A. S-wave velocities of each layer were changed within a range of ±10 % in the simulated model. Circles and crosses are the observed phase velocities from the vertical and horizontal components, respectively.

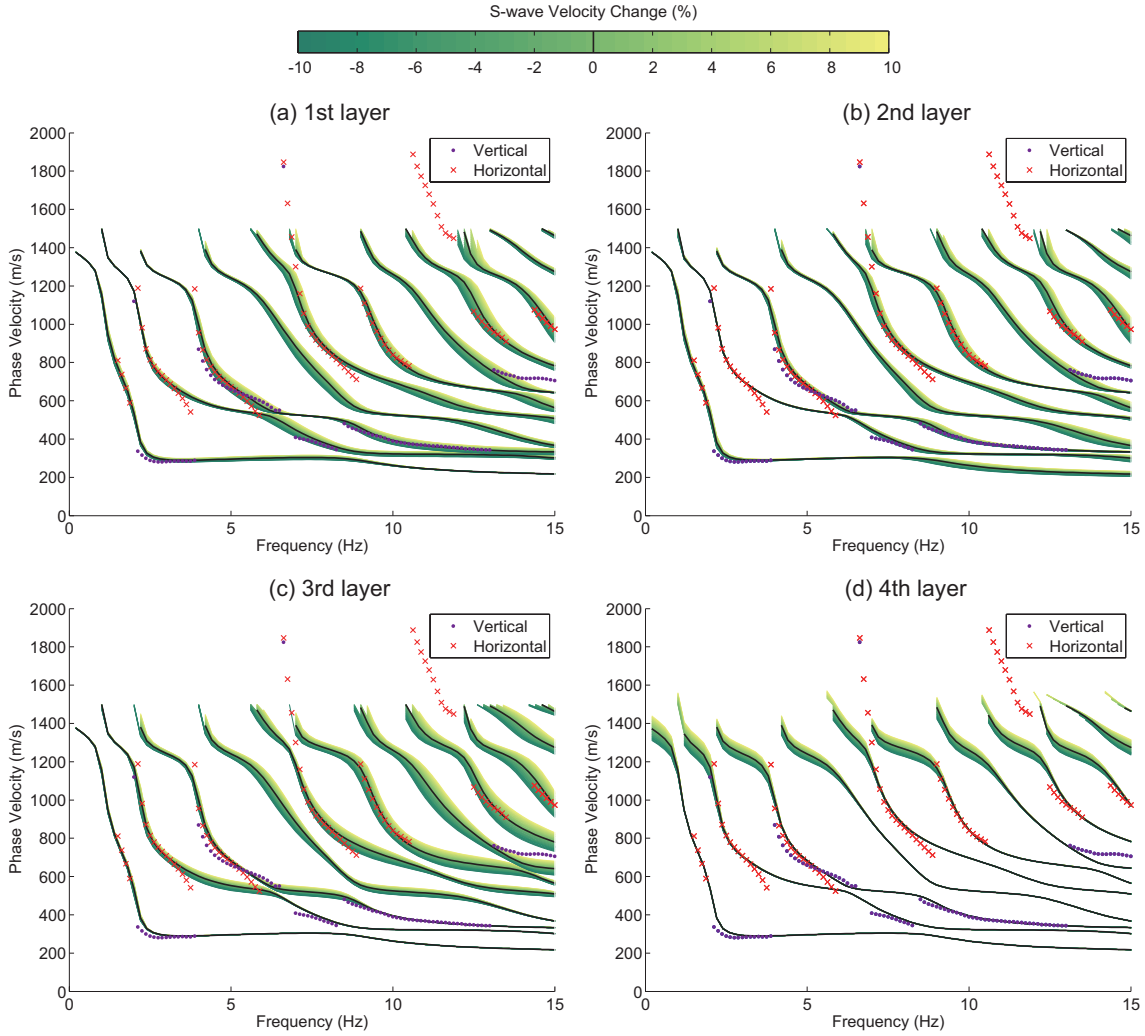

Figure 6.15: Sensitivity analysis results for the (a) first, (b) second, (c) third, and (d) fourth layers of Model B. S-wave velocities of each layer were changed within a range of ± 10 % in the simulated model. Circles and crosses are the observed phase velocities from the vertical and horizontal components, respectively.

CHAPTER VII

Window-controlled CMP crosscorrelation analysis for surface waves in laterally heterogeneous media

7.1 Introduction

As a non-destructive method for obtaining S-wave velocity structures, the surface wave method has been widely applied (e.g. *Miller et al.*, 1999; *Ryden and Lowe*, 2004; *Lin et al.*, 2004; *Foti et al.*, 2009; *Socco et al.*, 2010; *Tsuji et al.*, 2012). The surface wave method utilizes the dispersion characteristics of surface waves. *Nazarian and Stokoe* (1984) introduced the spectral analysis of surface waves (SASW) method, in which dispersion curves of surface waves can be estimated from a pair of receivers. The accuracy of estimating dispersion curves is improved by using multichannel seismic data, for example, by multichannel analysis of surface waves (MASW) (*Park et al.*, 1998, 1999a) or by the *f-k* method (*Foti*, 2000, 2005). *Strobbia and Foti* (2006) also developed the multi-offset phase analysis (MOPA) method to estimate dispersion curves based on linear regression of phase versus offset. S-wave velocity structures can be estimated by inversion of observed dispersion curves of surface waves. In forward modeling of surface wave dispersion curves for inversion analysis, calculations of surface waves based on the theoretical approach of *Thomson* (1950) and *Haskell* (1953) require the assumption of vertically one-dimensional structures.

Therefore, two-dimensional S-wave velocity structures are usually built by assembling one-dimensional structures inverted from local dispersion curves. As long as inversion is applied assuming one-dimensional structures, the key to improving lateral resolution in surface wave analysis is to extract local dispersion curves corresponding to one-dimensional velocity structures beneath local points.

Hayashi and Suzuki (2004) developed common midpoint crosscorrelation (CMPCC) analysis of surface waves, in which crosscorrelations with the same CMP are gathered. Since midpoints of all the crosscorrelation pairs coincide with the CMP, local dispersion curves can be estimated with high lateral resolution from crosscorrelation gathers by the CMPCC method. In another approach, *Vignoli and Cassiani* (2010) improved the MOPA method by adding an analysis to recognize the knee point of phase differences. *Lin and Lin* (2007) and *Obando et al.* (2010) made up shot gathers with long receiver distances by using a walk away survey with phase seaming approach.

Another strategy to improve lateral resolution in surface wave analysis is the application of spatial windows to seismic data. *Bohlen et al.* (2004) applied a Gaussian spatial window for the common receiver gather constructed by single receivers to pick up a local wavefield. *Grandjean and Bitri* (2006) extended this approach to multi-receiver gathers by stacking local wavefields. Similarly, *Boiero and Socco* (2010) applied a moving window to seismic data and stacked the spectrum using the *f-k* method. *Boiero and Socco* (2011) used a Gaussian window with a variable width depending on the wavelength. *Bergamo et al.* (2012) provided a chart quantitatively representing the relationship among Gaussian window widths, lateral resolution and wavenumber resolution by applying the Rayleigh resolution criterion to the array smoothing function (ASF).

In this paper, we describe the application of two kinds of spatial windows to CMPCC analysis to enhance the lateral resolution of dispersion curve estimations. The

first spatial window uses the number of crosscorrelation pairs as a weighting function for crosscorrelation gathers. The second removes crosscorrelation pairs with receiver spacing greater than a threshold to improve the accuracy of phase velocity estimations in terms of wavenumber resolution defined for given receiver configurations. We also introduce the expected wavelength dependence of the window (*Boiero and Socco*, 2011) into CMPCC analysis. The resulting window-controlled CMPCC analysis method is then applied to simulated data for a laterally heterogeneous structure. We also demonstrate the application of the method to field data from Ehime Prefecture, Japan, where lateral heterogeneity is expected from the presence of the Median Tectonic Line.

7.2 Common midpoint crosscorrelation method

In this section, we first summarize the CMPCC method developed by *Hayashi and Suzuki* (2004). We next describe the ASF in the CMPCC analysis in order to evaluate wavenumber resolution for given receiver configurations related to the accuracy of phase velocity estimations. Then we introduce the window-controlled CMPCC analysis method.

7.2.1 Conventional CMPCC analysis

The concept of CMPCC analysis (*Hayashi and Suzuki*, 2004; *Hayashi*, 2008) is shown schematically Figure 7.1. Data acquisition for the CMPCC method is similar to that for a two-dimensional multi-channel seismic reflection survey. CMPs in surface wave analysis are not defined at the midpoint between a source and a receiver, as in reflection seismology, but at the midpoint between two receivers. Crosscorrelations between possible pairs in each shot gather are calculated. If N receivers are employed in data acquisition, ${}_NC_2 (= N(N-1)/2)$ crosscorrelation pairs can be generated from each shot gather. Normalized crosscorrelations in the time domain with the same

CMP are grouped and defined as a CMPCC gather (Figure 7.1b). All crosscorrelations with the same receiver spacing at the same CMP are stacked when making CMPCC gathers. A CMPCC gather includes phase differences extracted from multiple shot data, whereas phase velocities are estimated from a single shot gather by MASW. Moreover, all the crosscorrelations in the CMPCC gather have paths on the CMP because the midpoints of crosscorrelations coincide with the CMP whereas not all the observed waveforms used in MASW have paths on the midpoints between the survey line corresponding to the CMP in the CMPCC analysis. Therefore, CMPCC analysis can generate local dispersion curves on a CMP with higher lateral resolution than the MASW method. Suppose that 75 receivers with 4 m receiver spacing are used and that source intervals are 2 m. If the receivers entirely cover the survey line, the number of crosscorrelation pairs in each CMPCC gather can be described for all receiver spacings and distances from the CMP as shown in Figure 7.2. (We employ this same geometry for the simulation study in the next section.) Then the CMPCC gathers are transformed into the frequency domain by Fourier transform and integrated over all receiver spacings with a phase shift. By taking absolute values of integrated CMPCC gathers, the dispersion image U can be described as

$$U(c,\omega) = \left| \int_{-\infty}^{\infty} F(\omega, x) e^{i\omega x/c} dx \right|, \tag{7.1}$$

where c is the phase velocity, ω is the angular frequency, x is the receiver spacing, and F is the Fourier transform of the stacked CMPCC gather over the same receiver spacings in the frequency domain. Phase velocities can be defined where U has the maximum value for a given frequency.

7.2.2 ASF in CMPCC analysis

To evaluate the accuracy of phase velocity estimates for given receiver configurations in CMPCC analysis, we follow the approach for wavenumber resolution of the ASF used in the *f-k* method (*Boiero and Socco*, 2011; *Bergamo et al.*, 2012). Note that the receiver spacing of CMPCC gathers has the same meaning as the offset of shot gathers in the *f-k* method in the definition of wavenumber resolution. If we assume that observed seismic waves are composed of only the fundamental mode of surface waves and apply the weighting function W for x, F in equation 7.1 can be described as

$$F(\omega, x) = W(x)e^{-i\omega x/c_{true}}, \tag{7.2}$$

where c_{true} is the phase velocity of the fundamental mode. In conventional CMPCC analysis, $W = 1$ for all receiver spacings x because stacked crosscorrelations are normalized by the number of crosscorrelation pairs. In the following, however, the number of crosscorrelation pairs is given as the weighting function W to enhance lateral resolution. By substituting equation 7.2 into equation 7.1, we obtain

$$U(k, \omega) = \left| \int_{-\infty}^{\infty} W(x)e^{i(k-k_{true})x}dx \right|, \tag{7.3}$$

where k_{true} is the wavenumber for the fundamental mode of surface waves. From equation 7.3, the dispersion image U can be considered as the absolute value of the Fourier transform of the weighting function W in which the wavenumber is shifted to k_{true}. Thus, we can write equation 7.1 as

$$U(k, \omega) = |ASF| * P(k, \omega), \tag{7.4}$$

$$ASF = \int_{-\infty}^{\infty} W(x) e^{ikx} dx, \tag{7.5}$$

where P is the theoretical spectrum for the fundamental mode of surface waves. In other words, the dispersion image estimated by CMPCC analysis can be considered as the convolution of the absolute value of the ASF with the theoretical spectrum as in Figure 7.3, similar to the case in *f-k* analysis (*Boiero and Socco*, 2011; *Bergamo et al.*, 2012). As the receiver spacing in CMPCC analysis is a discrete number, equation 7.5 should be rendered by using summation as follows:

$$ASF = \sum_{j=1}^{N} W(x_j) e^{ikx_j}. \tag{7.6}$$

By applying a similar procedure to MASW, we can also describe the estimated dispersion image by the convolution of the absolute value of the ASF with the theoretical spectrum for MASW. In the conventional CMPCC, MASW, and *f-k* methods, W is constant over x. However, *Boiero and Socco* (2011) and *Bergamo et al.* (2012) used a Gaussian window for W in the *f-k* method to concentrate weight on local points to enhance lateral resolution in local dispersion curve estimations.

7.2.3 Wavenumber resolution of the ASF

Suppose the number of pairs in the CMPCC gather is as described in Figure 7.2 and the number of crosscorrelation pairs is used as a weighting function in equations 7.2 and 7.6. For noise-free data, the dispersion image estimated by CMPCC analysis can be described by the convolution of absolute values of the ASF with the theoretical spectrum as in Figure 7.3a. Figures 7.3b and 7.3c depict the estimated dispersion images when CMPCC gathers include data with receiver spacing less than 200 and 100 m, respectively. Although removing longer-spaced receiver pairs enhances the lateral resolution of local dispersion curve estimations, it can be seen that it makes

estimated dispersion images less clear.

Removing crosscorrelation pairs with longer receiver spacing while keeping the accuracy of phase velocity estimations requires care in defining the resolution in terms of maximum detectable wavelength or minimum detectable wavenumber. A maximum detectable wavelength is experimentally defined by 40-50 % of the spread length (e.g. *O'Neill*, 2003; *Bodet et al.*, 2009). Another definition is based on the width of the mainlobe of the ASF (*Johnson and Dudgeon*, 1993). In this study, we used the full width of the mainlobe at one-half the peak value (full-width half-maximum or FWHM) as the wavenumber resolution kmin shown as in Figure 7.3 as *Wathelet et al.* (2008) did in ambient noise data analysis. The FWHM depends on not only the spread length but also the weighting function W for receiver spacings x in equation 7.6. The wavenumber resolution k_{min} is related to the minimum detectable wavenumber and the minimum wavenumber distance between two modes, as demonstrated by *Bergamo et al.* (2012) using k_{min} from the Rayleigh resolution criterion (*Johnson and Dudgeon*, 1993). The wavenumber resolution can also be transformed into wavelength resolution $\lambda_{max}(= 2\pi/k_{min})$. As the maximum detectable wavelength is proportional to the spread length, it would be also proportional to the maximum wavelength λ_{max} corresponding to the FWHM. Therefore, the maximum detectable wavelength is defined as $\alpha\lambda_{max}$ in this study.

7.2.4 Window-controlled CMPCC analysis

Lateral resolution can be improved by window-controlled CMPCC analysis in which we consider the number of crosscorrelation pairs in each CMPCC gather (Figure 7.2a) as a spatial weighting function W. As the receiver spacing of crosscorrelations becomes shorter, the number of crosscorrelation pairs increases, yielding improved lateral resolution.

As a second step, we exclude crosscorrelation pairs with longer receiver spacing to

further improve local dispersion curve estimations. Although this removal decreases the accuracy of phase velocity estimations in terms of wavenumber resolution k_{min} (Figure 7.3), we attempt to maintain the required accuracy through consideration of wavenumber resolution k_{min} or wavelength resolution λ_{max}.

When crosscorrelation pairs are removed from pairs with longer receiver spacing, the ASF and λ_{max} for each receiver configuration can be obtained. The following relationship is proposed to remove as many crosscorrelation pairs as possible such that the maximum detectable wavelength $\alpha\lambda_{max}$ is not less than the observed wavelength λ_{obs}.

$$\lambda_{obs}(f) < \alpha\lambda_{max}(f). \tag{7.7}$$

Because wavelengths corresponding to local dispersion curves are themselves values extracted by surface wave analysis, we use observed wavelengths from the CMPCC analysis without removal of receiver pairs. The maximum detectable wavelength depends on unknown effects in seismic data (e.g., from body waves, higher modes of surface waves, magnitudes of lateral heterogeneity, or incoherent noise) and they are not considered in determining the maximum wavelength λ_{max}. Thus, several tests of α should be carried out to determine the optimal value of α for each dataset.

Figure 7.4 shows the relationship between $\alpha\lambda_{max}$ and maximum receiver spacing for $\alpha = 1.0$ and 0.7 when the receiver configuration described in Figure 7.2 is employed. The maximum detectable wavelength $\alpha\lambda_{max}$ usually decreases with decreasing maximum receiver spacings. If the observed wavelength is 100 m, maximum receiver spacing can be defined as 124 and 184 m for $\alpha = 1.0$ and 0.7, respectively. Thus, the use of small values of α makes the spatial window wide.

7.3 Simulation study

In this section, we apply window-controlled CMPCC analysis to a simulated model with lateral heterogeneity from a synthetic dataset.

Figure 7.5 shows a part of the two-dimensional elastic velocity structure used in this simulation. For simplicity, the simulated model is selected so that higher modes of surface waves have little effect on the surface wave analysis. P-SV waves are computed by a velocity-stress staggered grid using the finite-difference method (*Virieux*, 1986) with an absorbing boundary condition (*Cerjan et al.*, 1985). Sources to normal stress are located on surface grids. The distance between the source and the nearest receiver is 5 m. 75 receivers are used at a receiver spacing of 4 m. Source and receiver locations are moved by 2 m and data acquisitions are repeated. Positions of sources and receivers entirely cover the simulated model. The CMP is defined every 2 m. Other parameters are summarized in Table 7.1.

Figure 7.6a shows the theoretical distribution of dispersion curves at each CMP for the simulated model. The theoretical local dispersion curves are calculated by the compound matrix method (*Saito*, 1988; *Saito and Kabasawa*, 1993) and correspond to the one-dimensional velocity structures beneath the horizontal points. We applied window-controlled CMPCC analysis to the simulated data, using the number of crosscorrelation pairs (described as in Figure 7.2) as the weighting function in equation 7.2 for each CMPCC gather. The maximum receiver spacing in CMPCC gathers was 296 m; however, crosscorrelation pairs with receiver spacing greater than 200 m were excluded so as to cut off the effects of lateral heterogeneity at distances greater than 100 m from the CMP. We used maximum wavelengths up to wavelengths of 400 m in the CMPCC analysis. As the phase velocity of Rayleigh waves of the fundamental mode approximately reflects the average S-wave velocity down to depths of 1/2 to 1/4 wavelength (e.g. *Hayashi*, 2008; *Socco et al.*, 2010), we infer that S-wave velocity structures are robust down to about 100 m. Note that for the same wave-

lengths, higher mode data are more sensitive to S-wave velocities in deeper layers than fundamental mode data (*Xia et al.*, 2003).

An example of CMPCC gather at 100 m horizontal distance is shown in Figure 7.7. The observed dispersion curves (Figure 7.6b) at both ends of the simulated model, where there is almost no lateral heterogeneity, are consistent with the theoretical curves (Figure 7.6a). However, lateral variation of dispersion curves corresponding to the slope of the simulated model, is not clear.

Next we excluded crosscorrelation pairs considering the maximum wavelength (minimum wavenumber) for the ASF. The chart in Figure 7.8 shows the maximum receiver spacing at 150 m horizontal distance when α is 0.6 in equation 7.7. For the observed wavelengths in equation 7.7, we used the dispersion curve without consideration of maximum wavelength for the ASF (Figures 7.6b and 7.8b). For the wavelength of 33.4 m at 15.5 Hz, the maximum receiver spacing satisfying equation 7.7 can be defined as 68 m (Figures 7.8a and 7.8c). On the other hands, there was no crossing point between $0.6\lambda_{max}$ and the observed wavelength of 215.4 m at 4.88 Hz. Although the resolution of observed wavelengths from the ASF was insufficient in our definition, we used a maximum receiver spacing of 200 m for observed wavelengths up to wavelengths of 400 m, to retain the investigation depth down to 100 m.

Maximum receiver spacings were originally 200 m for all frequencies and CMPs. By applying the proposed window based on equation 7.7, maximum receiver spacings for $\alpha = 0.5$ and 0.6 (Figure 7.9) were considerably decreased. Figures 7.6c and 7.6d show the corresponding observed dispersion distributions from CMPCC analysis. Lateral variations of dispersion curves due to lateral heterogeneity are well reproduced by the window-controlled CMPCC analysis. The larger value of α clearly reveals the lateral variation of dispersion curves. Figure 7.10 shows dispersion curves for receiver spacing less than 200 m and four values of α between 0.4 and 0.7 at 100 m horizontal distance, demonstrating that larger values of α yield dispersion curves consistent with

the theoretical dispersion curve where there is lateral heterogeneity near the CMP.

On the other hand, larger values of α reduce the accuracy of phase velocity estimations, in terms of maximum wavelength from the ASF, and it make the dispersion image unclear. Our task, then, is to find an optimal value of α that is as large as possible compatible with suitable resolution of phase velocity estimations. Figure 7.11 shows observed and theoretical dispersion curves at 260 m horizontal distance, where there is little lateral variation. We can perform validation tests of the accuracy of estimated phase velocity for several values of α at this point, neglecting the effect of lateral heterogeneity. Larger values of α produced fluctuations in dispersion curves, especially at high frequencies. These fluctuations are caused by noise effects other than lateral heterogeneity because there is almost no lateral variation in this CMP. To suppress these noise effects, we have to apply smaller values of α. We determined $\alpha = 0.5$ to be the best compromise between lateral resolution and accuracy of phase velocity estimations. Although it is difficult to find locations with no lateral variation in real datasets, we can predict lateral variation using quasi two-dimensional dispersion curves without a frequency-dependent spatial window (e.g., Figure 7.6b). Lateral heterogeneity of the simulated velocity model was well retrieved by inversion of dispersion curves estimated by the window-controlled method (*Ikeda et al.*, 2013a)(Figure 7.12).

7.4 Application to field data

We applied window-controlled CMPCC analysis to a set of field data acquired in Saijo City, Ehime Prefecture, Japan (Figure 7.13). Multi-channel seismic data along a 1-km survey line were originally acquired for reflection survey in an investigation of fault geometry on the Median Tectonic Line (MTL) (*Minato et al.*, 2012). Because the survey line was normal to the MTL, we can evaluate the dip-angle of the fault. The data acquisition parameters are summarized in Table 7.2.

CMPs for surface wave analysis were defined every 10 m along the survey line after applying a linear approximation of the survey line for reflection survey as in Figure 7.13c. Maximum receiver spacing in CMPCC gathers can range from 238 to 638 m because the number of receivers used in data acquisition ranged from 83 to 163 with receiver intervals of about 4 m. However, we used crosscorrelation pairs with less than 200 m receiver spacing to cut off the effect of lateral variation from receiver spacings greater than 200 m. We used maximum wavelengths up to wavelengths of 400 m, keeping the investigation depth down to about 100 m. We used the number of crosscorrelation pairs as the weighting function in equation 7.2.

The CMPCC gather at 10 m horizontal distance is shown in Figure 7.14. For easy visualization of surface waves, a 30 Hz low-pass filter was applied. Figure 7.15 shows three dispersion curves distributions estimated from our CMPCC analysis. The abrupt lateral variation in this field, at $\sim$ 600 m horizontal distance, corresponds to the lithological boundary generated by fault displacements. A lateral variation between 200 and 450 m is also observed. Higher modes of surface waves are predominant from 220 to 320 m and at some points beyond 600 m, where jumping of dispersion curves is observed. Maximum receiver spacings (Figure 7.16) are considerably decreased in the window-controlled CMPCC analysis. Although the observed dispersion curve at 360 m with receiver spacing less than 200 m shows fluctuations at about 10 Hz, these are removed by applying frequency-dependent windows (Figure 7.17).

Next we determined the optimal value of the windowing factor α from the various dispersion curves. Figure 7.18 shows the dispersion curves at 10 m where there is little lateral heterogeneity. The figure shows that observed dispersion curves fluctuated at higher values of α, although the dispersion curves given by window-controlled CMPCC analysis with $\alpha = 0.7$ are mostly stable. At 250 m (Figure 7.19), the discontinuity in the observed dispersion curves indicates the predominance of higher

mode of surface waves at around 8 Hz. As the amplitude of the fundamental mode is relatively large and both modes are close in this frequency range, it is difficult to clearly distinguish both modes by using windows with $\alpha = 0.6$, 0.7, or 0.8. The difficulty is similar at 260 m. Thus, we applied $\alpha = 0.5$ at 250 and 260 m and $\alpha = 0.7$ at other points in this field example.

After that preparation, we obtained two-dimensional S-wave velocity structures by genetic algorithm inversion with dynamic mutation and elite selection (*Yamanaka and Ishida*, 1996) based on the procedure of *Tsuji et al.* (2012). We constructed reference S-wave velocity models with six layers by transforming 1.1 $\times$ observed phase velocity into S-wave velocity and 1/3 $\times$ observed wavelength into depth (e.g. *Heisey et al.*, 1982). The thickness of each layer in reference models is 20 m. We carried out a multi-mode inversion by using the amplitude response of surface waves (*Harkrider*, 1964, 1970), because higher modes were predominant in the observed dispersion curves (e.g., Figure 7.19). In the multi-mode inversion, theoretical phase velocities were defined as velocities of the mode with the maximum amplitude for a given frequency (e.g. *Hayashi and Saito*, 2004; *Lu and Zhang*, 2006; *Tsuji et al.*, 2012). P-wave velocities were obtained from S-wave velocities by using linear regression between P- and S-wave velocities constructed from PS logging at the logging well in Figure 7.13c. Densities were obtained from S-wave velocities through the empirical equation of *Ludwig et al.* (1970). Other parameters for inversion are summarized in Table 7.3.

The inverted two-dimensional S-wave velocity structures and the S-wave velocities measured by PS logging at the logging well are shown in Figure 7.20. Note that the S-wave velocity structure from logging well is overlaid on the inverted S-wave velocity structure at horizontal distance nearest to the survey line for the CMPCC analysis. As expected from the observed dispersion curves (Figure 7.15), the inverted structures have lateral variations between 200 and 450 m and at 600 m horizontal distance (Figure 7.20). The vertical velocity contrast may indicate the material boundary MTL

(*Okada*, 1972). The depth of the high velocity contrast in the logging data is approximately consistent with that of the inverted velocity structures. Slight difference comes from the fact that the logging well is around 20 m from the survey line. There are some differences between the inverted models from the CMPCC analysis without a frequency-dependent window (Figure 7.20a) and those from the window-controlled CMPCC analysis with $\alpha = 0.5$ and 0.7 (Figure 7.13b) at around 360 m horizontal distance owing to lateral heterogeneity. However, there are almost no differences in the inverted velocity models where lateral variation is small. In summary, the lateral resolution of the estimated dispersion curves is improved with respect to the original CMPCC analysis by applying window-controlled CMPCC analysis with enough resolution to estimate phase velocity.

7.5 Conclusions

To improve the lateral resolution in CMPCC analysis of surface waves, we proposed a window-controlled form of CMPCC analysis using two kinds of spatial windows. First, the number of crosscorrelation pairs is used as a spatial weighting function in CMPCC gathers. Crosscorrelation pairs in CMPCC gathers are then removed from pairs with longer receiver spacing. Although removing longer receiver pairs generally degrades dispersion images, we attempted to retain the required accuracy of phase velocity estimations by considering the wavenumber resolution obtained from the ASF. We introduced the coefficient α controlling the width of the window to define detectable wavelengths considering noise effects other than lateral heterogeneity.

We applied window-controlled CMPCC analysis to a simulated model with lateral heterogeneity, testing several values of α to determine the optimal value that retains the required accuracy to estimate phase velocities. The lateral variation of local dispersion curves for the simulated model was successfully improved by the window-controlled CMPCC analysis.

In an application of the method to field data, higher modes of surface waves were predominant at some points in the observed dispersion curves. As the narrow spatial window made it difficult to distinguish multi-mode dispersion curves, smaller values of α were applied to some dispersion curves with the predominant higher mode. S-wave velocity structures were then derived by inversion from the observed dispersion curves. The depth of the high velocity contrast in the logging data was approximately agreed with that of inverted velocity structures. The window-controlled CMPCC analysis modified lateral variations of the inverted S-wave velocity structure without degrading the accuracy of S-wave velocity estimations where lateral heterogeneity was small.

We conclude that window-controlled CMPCC analysis is effective in improving lateral resolution of dispersion curve estimations with respect to the original CMPCC analysis and subsequent two-dimensional S-wave velocity inversions.

Table 7.1: Parameters of P-SV finite-difference modeling for the simulated model.

Size of grid	1 m
Number of cell	1200(horizontal) × 300(vertical)
Source function	10Hz Ricker wavelet
Time interval	0.12 ms
Time step	10,000
The number of absorbing grids for each side	100

Table 7.2: Parameters of field data acquisition.

Length of survey line	1106 m
Source	Impactor
Receiver	Geophone
Natural frequency	30 Hz
Receiver interval	About 4 m
Sampling interval	1.0 ms
Samples	2001
Channel number	82-163
CMP interval	10 m

Table 7.3: Parameters used in the GA inversion; γ is the average coefficient of variation (*Yamanaka and Ishida*, 1996).

Generation	100
Population size	100
Crossover probability	0.7
Dynamic mutation probability	-
$\gamma \geqq 0.1$	0.01
$0.04 < \gamma < 0.1$	0.05
$\gamma \leqq 0.04$	0.1
Trial	20
Search range of V_s and thickness for the reference model, respectively.	±30 % and ±50 %

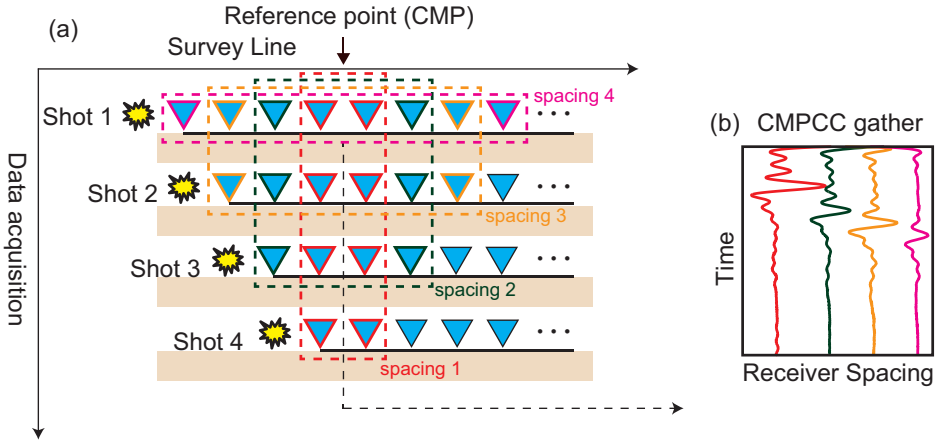

Figure 7.1: The concept of CMPCC analysis.

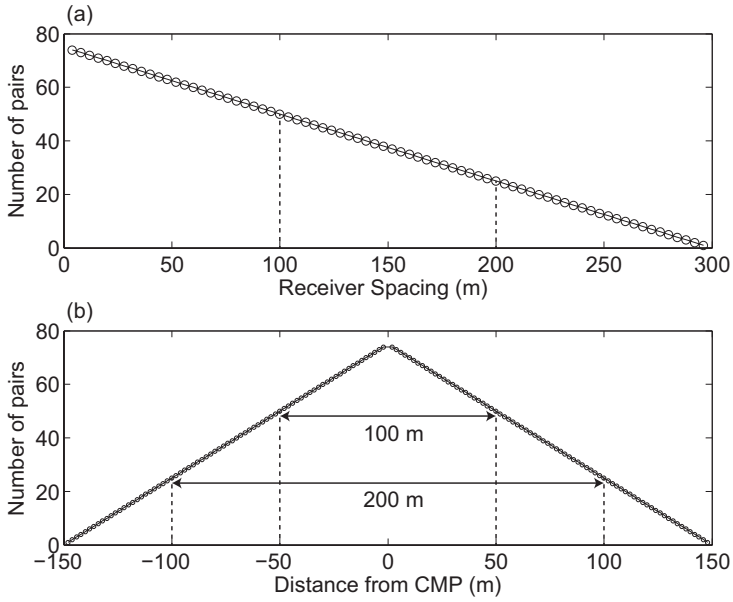

Figure 7.2: The number of pairs of crosscorrelations in each CMPCC gather for (a) receiver spacing and (b) distance from CMP, respectively.

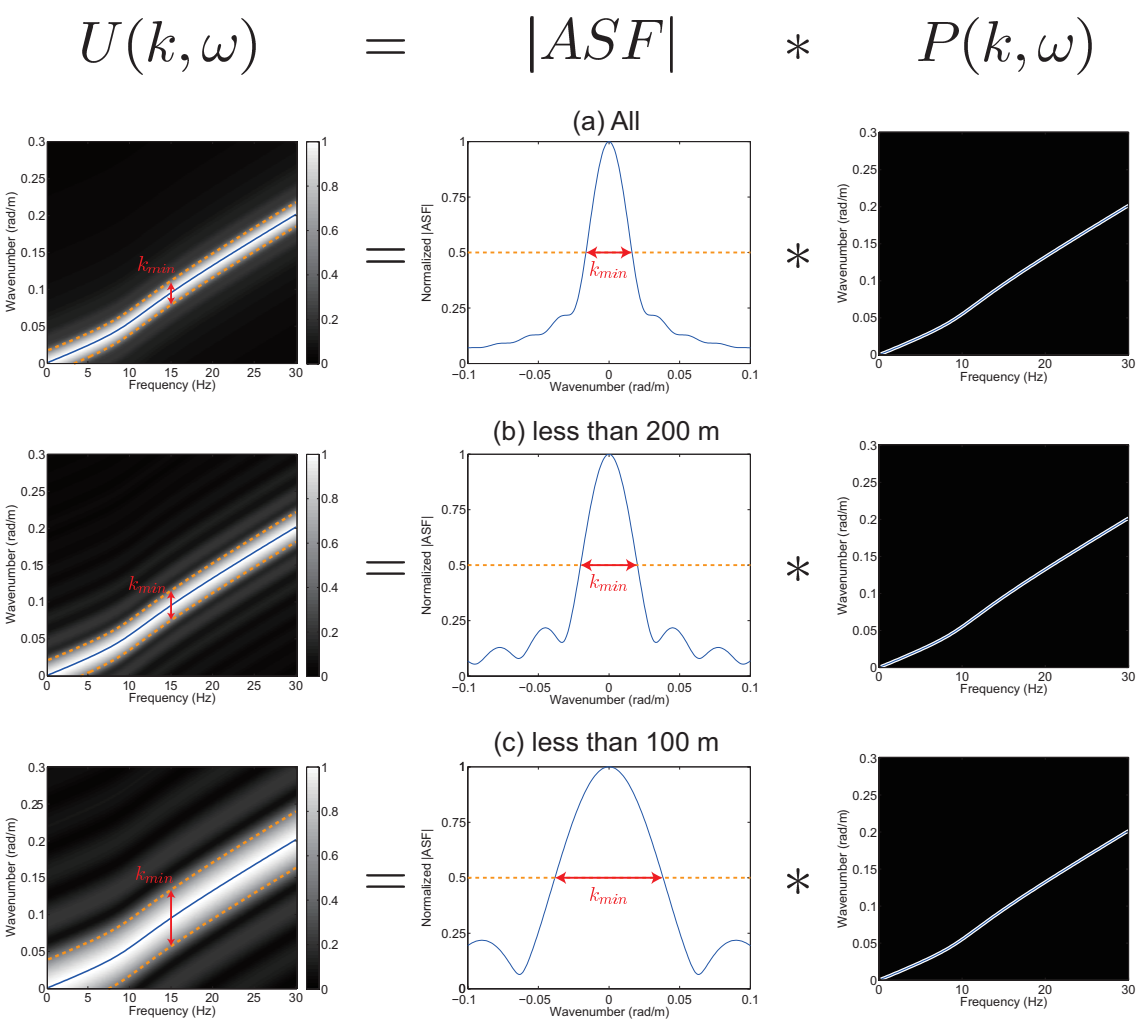

Figure 7.3: Estimated dispersion images described as the convolution of absolute values of ASF with theoretical spectra for the receiver configuration in Figure 7.2 when (a) all the crosscorrelation pairs, crosscorrelation pairs with receiver spacing (b) less than 200 and (c) 100 m are used. Blue lines in dispersion images indicate the theoretical dispersion curves. Red lines are the minimum wavenumber.

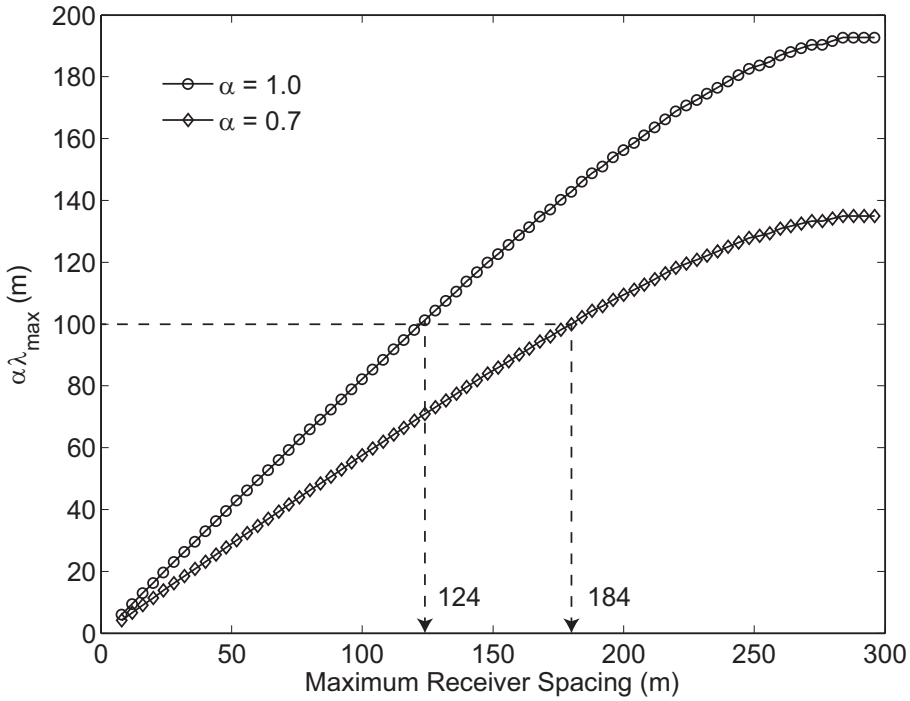

Figure 7.4: The relationship between $\alpha\lambda_{max}$ and maximum receiver spacing for $\alpha = 1.0$ and 0.7 when the receiver configuration described in Figure 7.2 is employed.

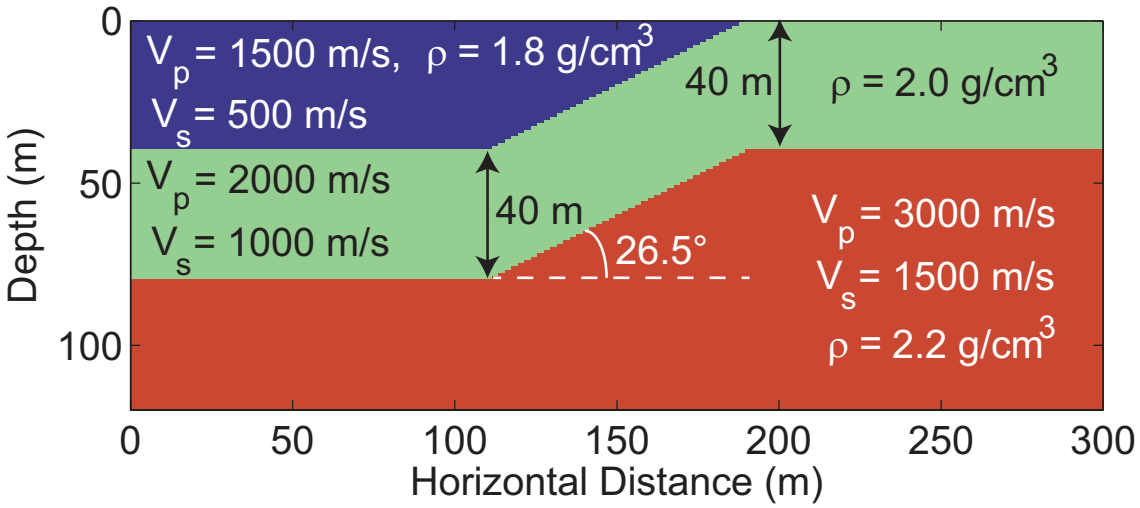

Figure 7.5: The simulated three-layered model. V_p, V_s, and ρ are the P-wave velocity, the S-wave velocity and the density, respectively.

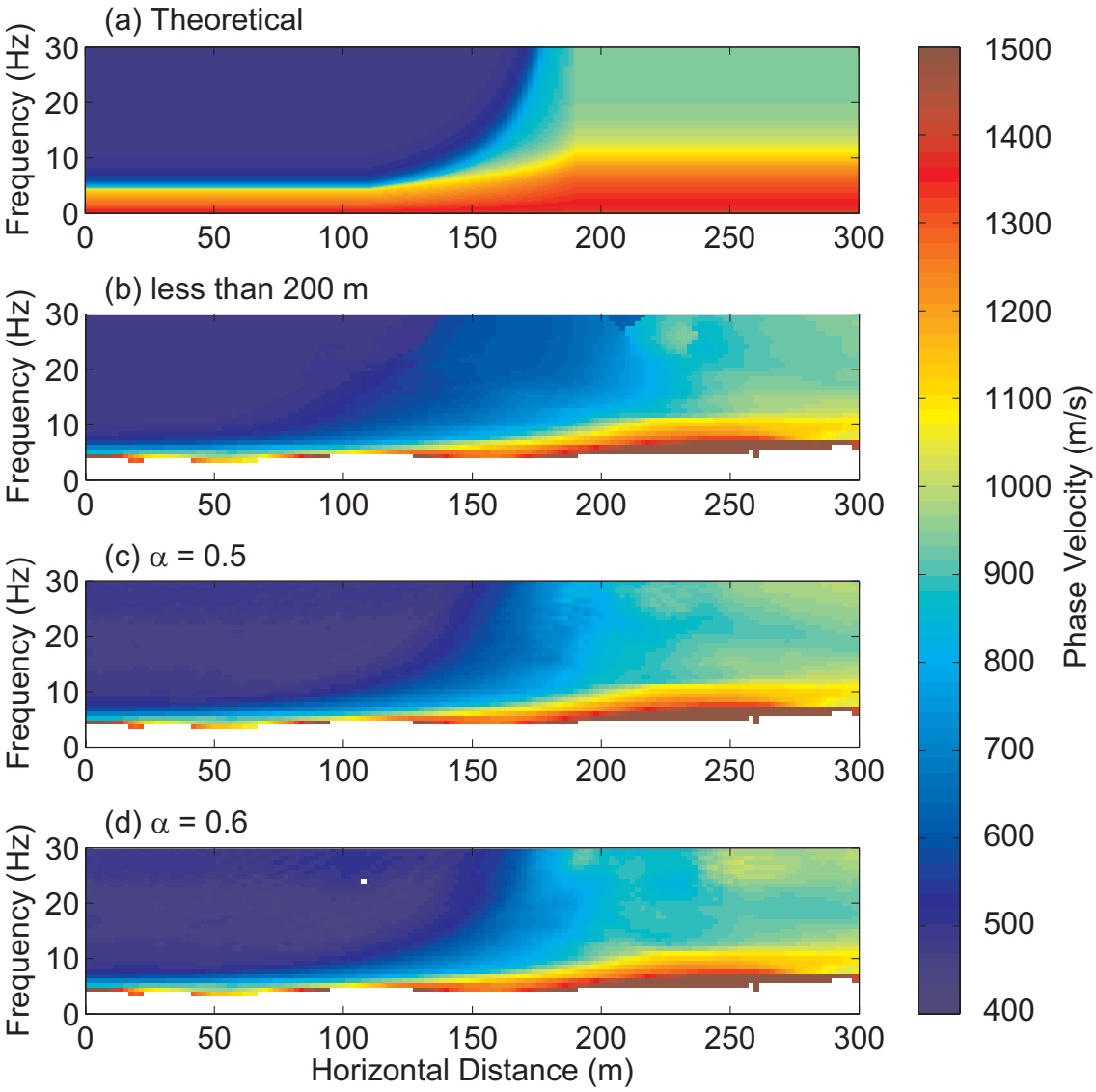

Figure 7.6: Dispersion curve distributions for the simulated model. (a) Theoretical dispersion curves for beneath one-dimensional structures for the horizontal points. Observed dispersion curves from CMPCC analysis with (b) receiver spacing less than 200 m, (c) $\alpha = 0.5$ and (d) 0.6.

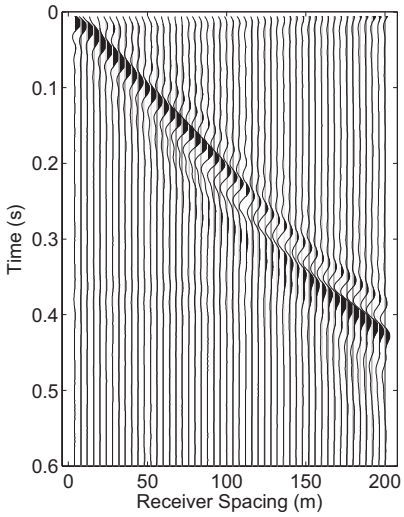

Figure 7.7: The CMPCC gather at 100 m horizontal distance.

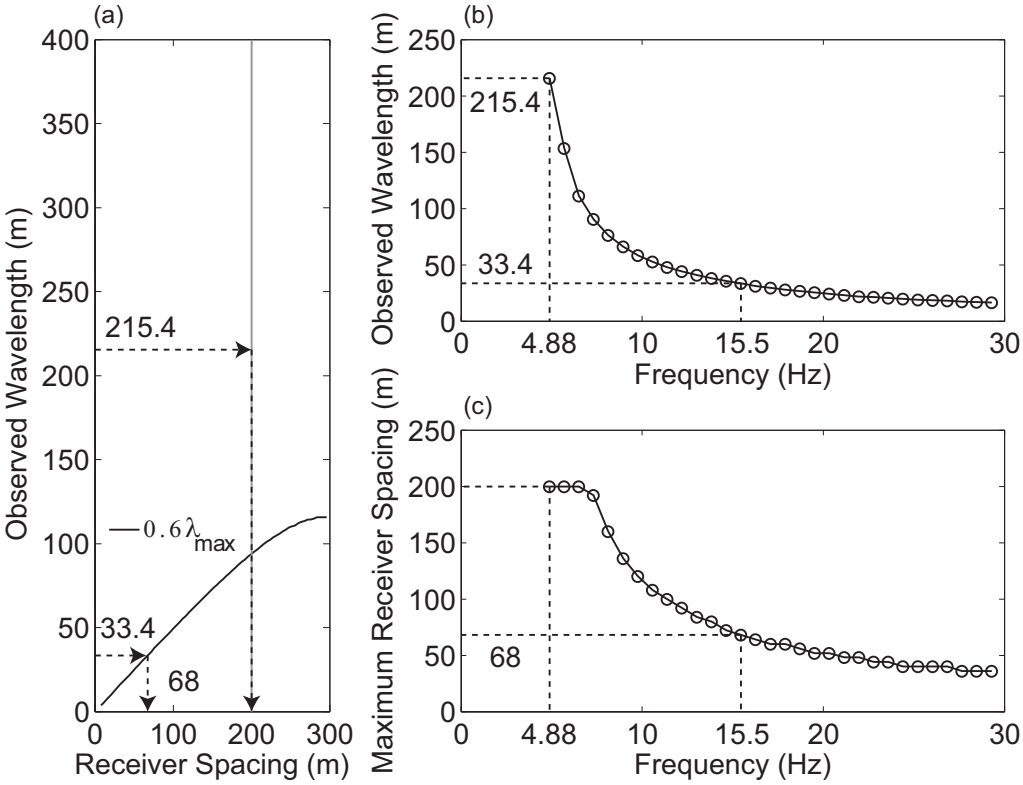

Figure 7.8: (a) Chart to determine maximum receiver spacing considering maximum wavelength for ASF. (b) Wavelengths of the observed dispersion curve and (c) determined maximum receiver spacing at 150 m horizontal distance.

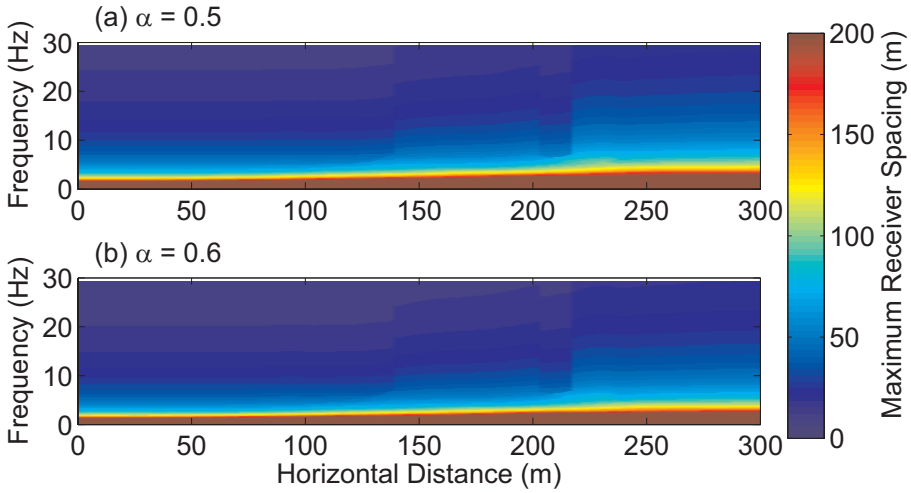

Figure 7.9: Maximum receiver spacings for the simulated model for α = (a) 0.5 and (b) 0.6.

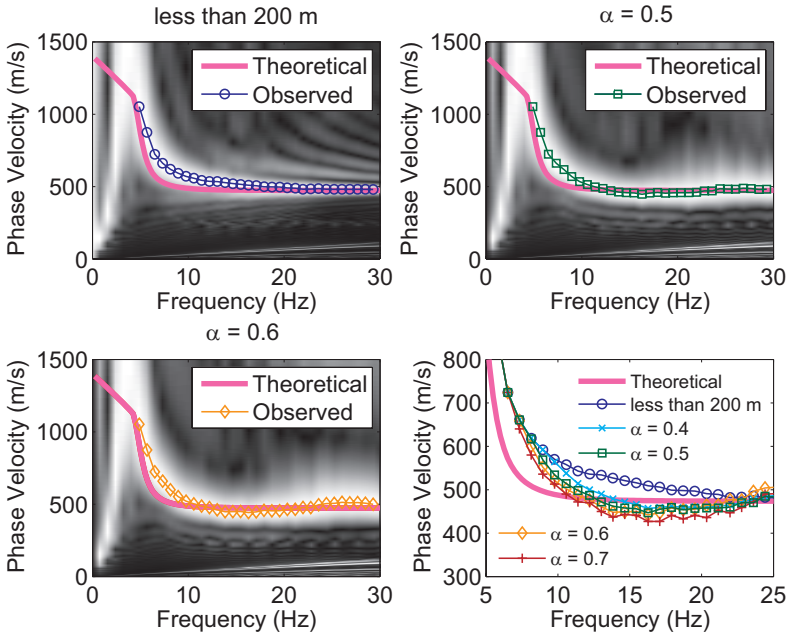

Figure 7.10: Comparison of observed dispersion curves with receiver spacing less than 200 m and α = 0.4-0.7 at 100 m horizontal distance. The corresponding CMPCC gather is described in Figure 7.7.

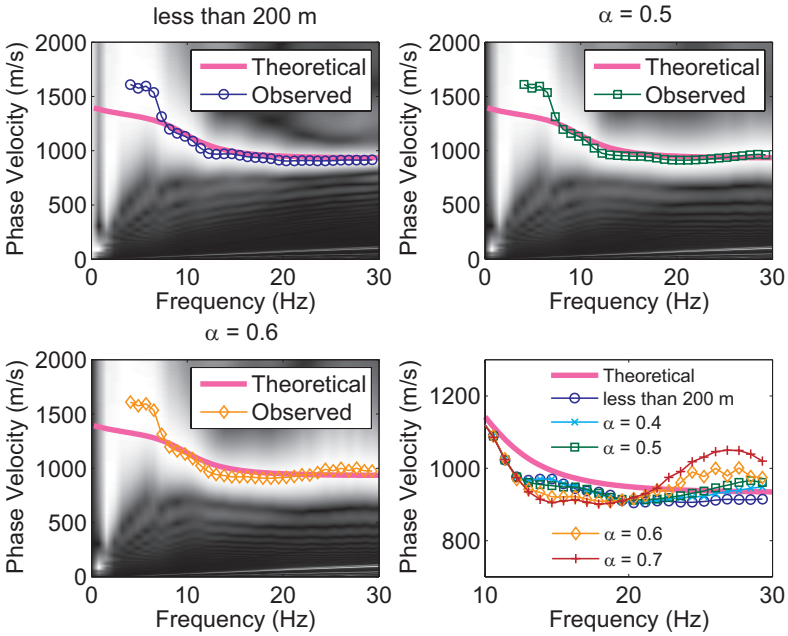

Figure 7.11: Comparison of observed dispersion curves with receiver spacing less than 200 m and α = 0.4-0.7 at 260 m horizontal distance.

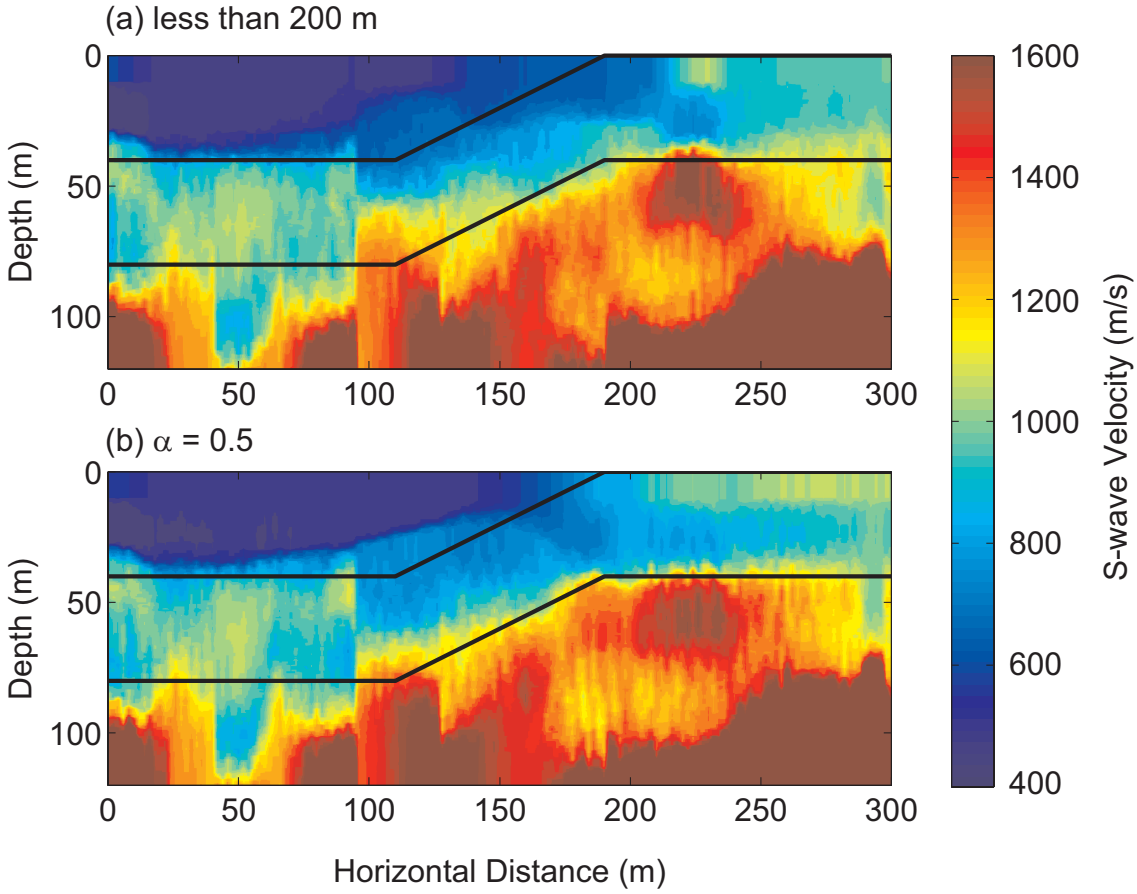

Figure 7.12: Inverted S-wave velocity structures for the simulated model estimated by genetic algorithm inversion for (a) receiver spacing less than 200 m and (b) $\alpha = 0.5$. Solid lines are boundaries of the simulated model (*Ikeda et al.*, 2013a).

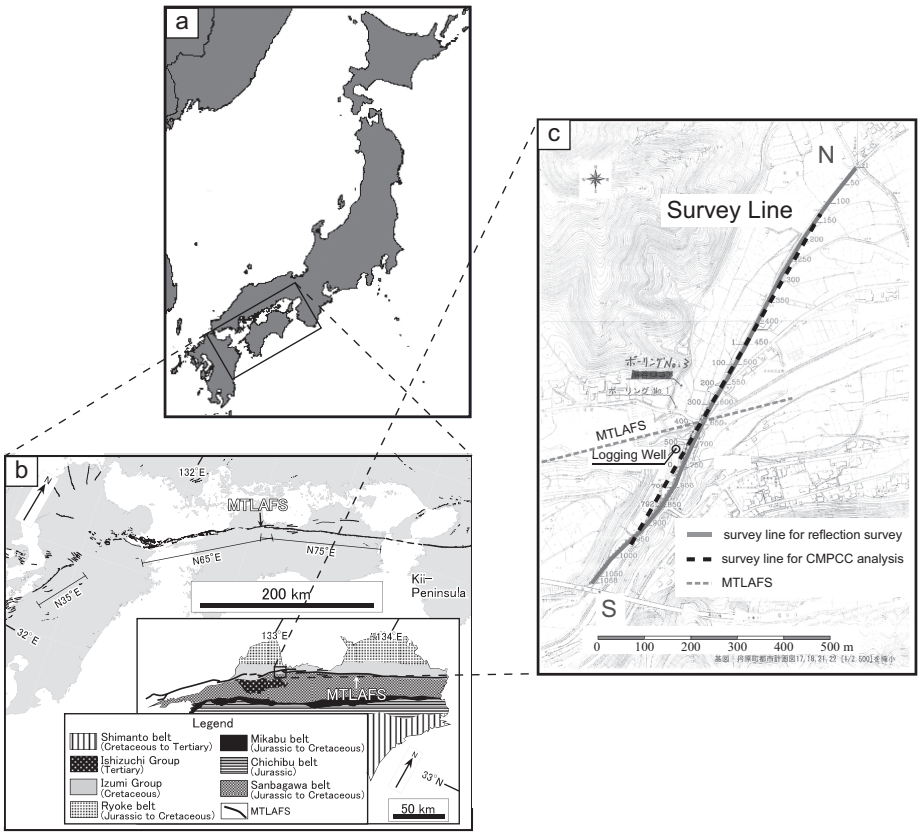

Figure 7.13: Study area with in in Shikoku Island. Panel (b) is modified from *Ikeda et al.* (2009). The relationship between survey line and MTL active fault system (MTLASF) is displayed in panel (c).

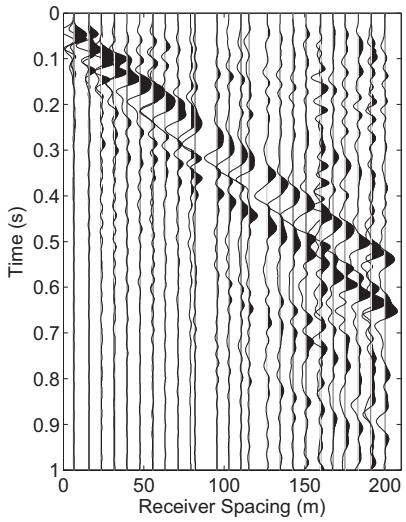

Figure 7.14: The 30Hz low-pass-filtered CMPCC gather at 10 m horizontal distance.

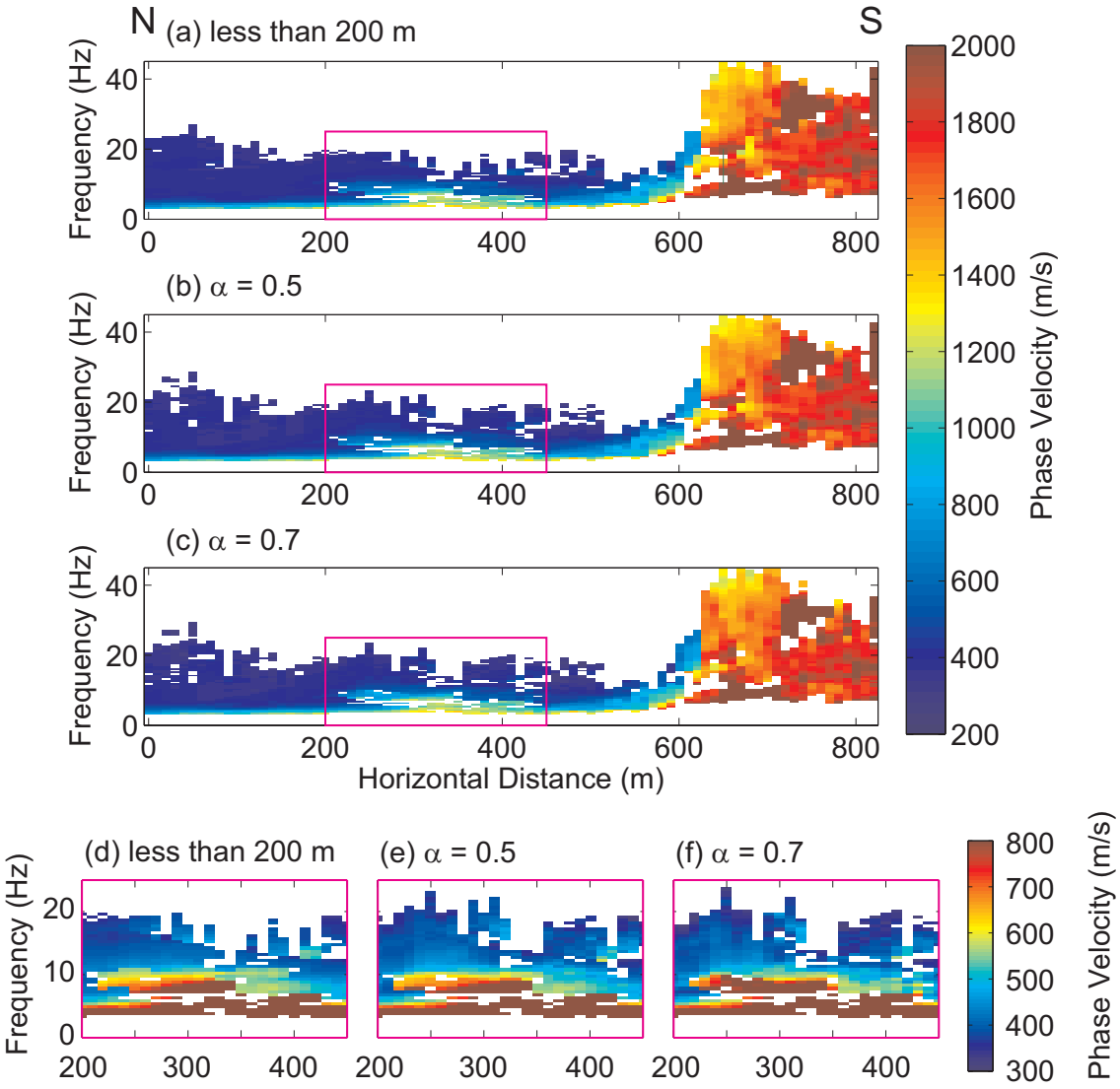

Figure 7.15: Observed dispersion curve distributions for field data calculated from CMPCC analysis with (a) receiver spacing less than 200 m, (b) $\alpha = 0.5$ and (c) 0.7. (d)-(f) are dispersion curve distribution between 200-450 m horizontal distance.

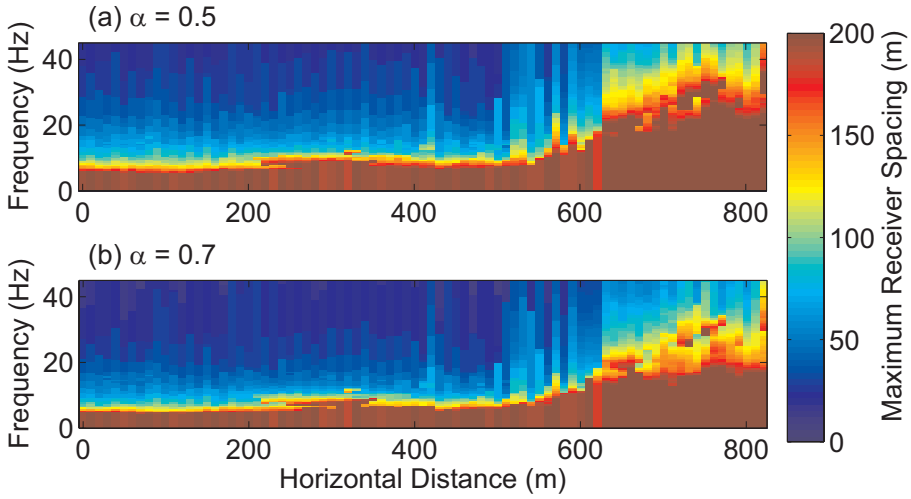

Figure 7.16: Maximum receiver spacings for field data for α = (a) 0.5 and (b) 0.7.

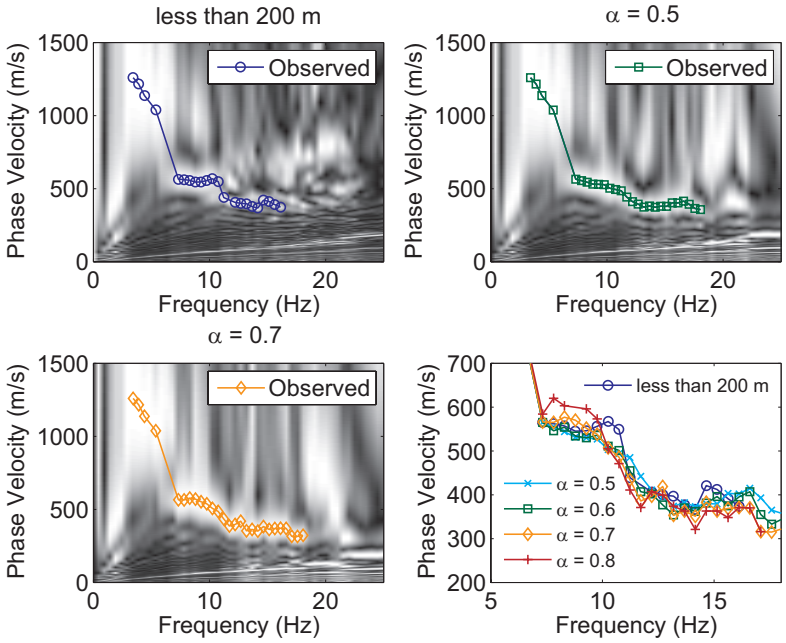

Figure 7.17: Comparison of observed dispersion curves with receiver spacing less than 200 m and α = 0.5-0.8 at 360 m horizontal distance.

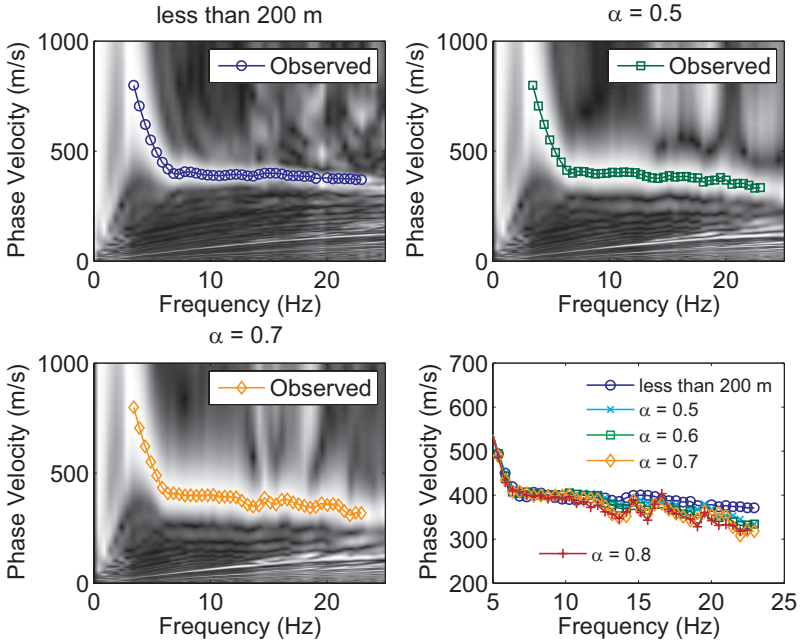

Figure 7.18: Comparison of observed dispersion curves with receiver spacing less than 200 m and $\alpha = 0.5$-0.8 at 10 m horizontal distance. The corresponding CMPCC gather is described in Figure 7.14.

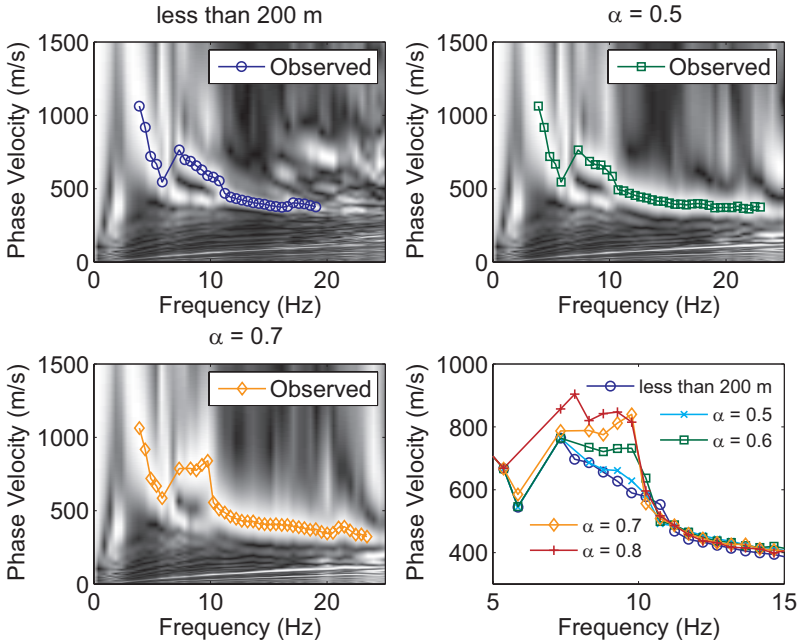

Figure 7.19: Comparison of observed dispersion curves with receiver spacing less than 200 m and $\alpha = 0.5$-0.8 at 250 m horizontal distance.

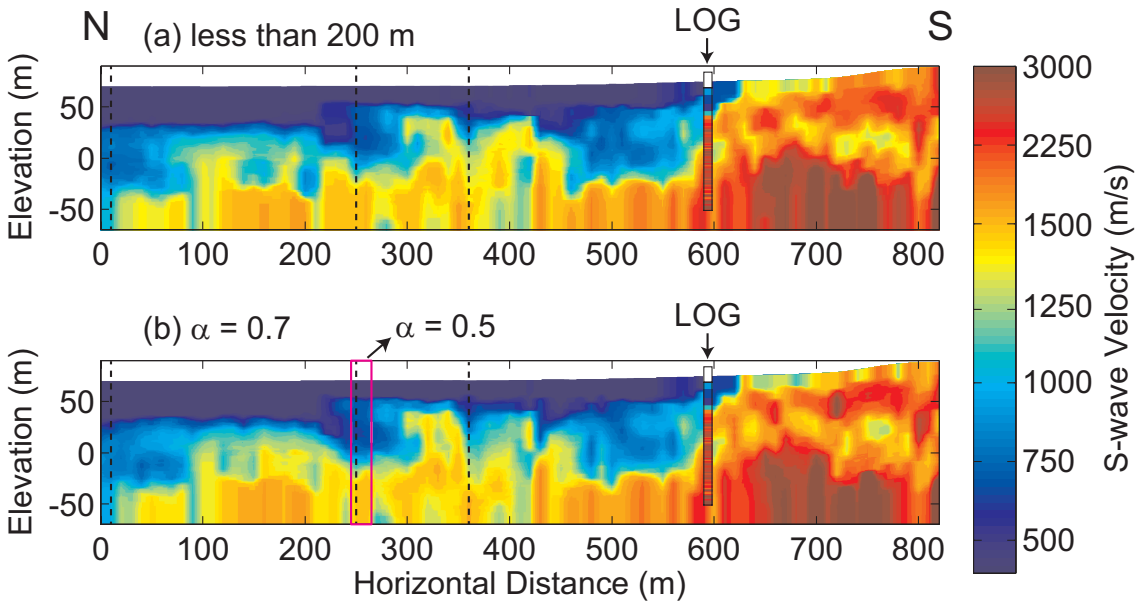

Figure 7.20: Inverted S-wave velocity structures by genetic algorithms inversion for (a) receiver spacing less than 200 m and (b) $\alpha = 0.5$ (cyan border) and 0.7. Dash lines correspond to horizontal points for Figures 7.17-7.19. The S-wave velocities measured by PS logging are overlaid.

CHAPTER VIII

Conclusions

8.1 Conclusions

In this dissertation, we have studied surface wave analysis methods for obtaining improved estimates of subsurface S-wave velocity structures.

In chapter 2, the theoretical computation method of Rayleigh waves on transversely isotropic media was developed by extending the reduced delta matrix method for isotropic media. It was demonstrated that the computational method has enough accuracy in computing theoretical Rayleigh waves such as phase velocities, group velocities, Rayleigh wave ellipticities, and amplitude responses at high frequencies. The method also decreases the computational time compared to the standard delta matrix method. This computational method will be useful in the inversion of surface waves with consideration of transverse isotropy in horizontally layered media.

In chapter 3, we investigated the effect of Love wave contribution to the joint inversion of spatial autocorrelation curves with HVSR curves. Although frequency-dependent Love wave contribution could be extracted by the three-component SPAC method, we failed to extract a Love wave contribution below the peak frequency of HVSR curves because the vertical components of Rayleigh waves have small amplitude at this frequency. Therefore, we needed to make an assumption about Love wave contribution. The results of joint inversion revealed that the choice of the assump-

tion of Love wave contribution is insensitive to the inverted velocity models down to bedrock, although there is an ambiguity in estimating S-wave velocities of bedrock.

In chapter 4, we proposed two multimode inversion techniques in the SPAC method considering the effect of different receiver spacings. One is multimode inversion, in which theoretical effective phase velocities are compared with observed velocities. We extended the method of computing theoretical effective phase velocities in order to consider the effect of different receiver spacings. The other is the direct fitting inversion of SPAC curves for each receiver spacing. The latter approach doesn't generate errors associated with conversion from coherencies to phase velocities that exist in the former approach. We applied two inversion techniques to noise synthetic data and successfully retrieved the S-wave velocity model. We then applied the multimode inversion methods to field data. The direct-fitting inversion generated S-wave velocity structures consistent with logging data without prior information. On the other hand, the multimode inversion using effective phase velocities required the prior information of S-wave velocities because large ambiguity was introduced in conversion from coherencies to phase velocities at low frequencies.

In chapter 5, we proposed a deconvolution technique for retrieving multimode surface waves. We also changed the procedure of the MASW to obtain the description in the proximity of the summation of the convolution for each mode component when multimode components were predominant. When two mode components were mixing, applying the deconvolution analysis separated two modes from single peaks. Although the estimated dispersion spectra with the modified MASW were contaminated by the effect of anelastic attenuation, multimode surface waves could be retrieved by the proposed method from simulated data by considering anelastic attenuation and field data. Separating mixing modes by the deconvolution analysis contributed not only to improving phase velocity estimations but also to identifying mode transition points, which is important to prevent mode misidentification.

In chapter 6, we investigated the characteristics of horizontal components of multimode Rayleigh waves as well as vertical component data. When sources were located near the surface, multimode Rayleigh waves extracted from horizontal component data were similar to those from vertical component data except at low frequencies. However, if the explosive sources were buried at deeper locations, the higher mode components of Rayleigh waves had larger amplitudes with the increase of the source depth. Higher order modes were especially dominant in horizontal component data. The higher modes extracted from horizontal component data had some amount of sensitivity for S-wave velocities, while there was small sensitivity in vertical component data. Additional mode components were also estimated from the additional use of the horizontal components of the field data. Although the use of a buried explosive source is unusual in the near-surface seismic survey, there are plenty of existing data in which three-component data were observed by dynamite at the depth of standard reflection seismic surveys. These results indicate the combined use of multimode Rayleigh waves for horizontal component data contributes to constructing S-wave velocity structures for statics correction in an analysis of seismic reflection.

In chapter 7, we proposed the window-controlled CMP cross-correlation analysis to improve the lateral resolution of dispersion curve estimations. In the proposed method, we applied wavelength-dependent spatial windows for cross-correlation gathers to provide a weight to local points. Applying a shorter window generally decreases the accuracy of phase velocity estimations. However, we reduced the window length as much as possible, keeping enough accuracy to estimate phase velocities considering wavenumber resolution for receiver configurations. We applied the window-controlled CMPCC method for simulated data in laterally heterogeneous media. The lateral variation of local dispersion curves can be successfully improved by the proposed method. We then applied the method to field data for estimating the lateral variation of S-wave velocities associated with fault deformation. Higher modes of surface

waves were predominant at some points. In this case, we used a longer window to identify different modes of surface waves. The two-dimensional S-wave velocity structure was constructed by inversion of local dispersion curves estimated by the proposed method without significant loss in estimating dispersion curves, indicating that lateral variation of the S-wave velocity structure is improved by the proposed method.

In summary, we improved surface wave analysis methods to enhance the accuracy of S-wave velocity structure estimations. We demonstrated the effectiveness of the analysis methods by applying both numerically simulated data and field data.

8.2 Recommendation for future works

The surface wave method is being established as the seismic survey method for estimating near-surface S-wave velocity structures owing to dramatic development caused by social demand for characterizing local ground conditions.

One of the future prospects for surface wave is the joint analysis of surface wave analysis with other data. *Hayashi et al.* (2005) demonstrated the joint analysis of a surface wave method and micro-gravity survey. P-wave refraction data can be easily combined with surface wave data (e.g. *Ivanov et al.*, 2006; *Dal Moro*, 2008; *Piatti et al.*, 2013) because a unique receiver layout can be used taking some care about the proper choice of time sampling (*Socco et al.*, 2010; *Piatti et al.*, 2013). Since surface wave analysis has the potential to construct near-surface velocity models better than other seismic methods, it can also be used jointly for supporting static estimation and correction and for providing a constraint of near-surface velocity models in full waveform inversion and improving PP-PS matching (*Boiero et al.*, 2013). Constructing S-wave velocity structures by the surface wave method contributes to estimating the ratio between P- and S-wave velocities, which is indicative of the pore fluid effect.

The other prospect is the use of amplitude information on surface waves to obtain quality factors (Q). Although near-surface quality factors are important in not only

evaluating local site amplification but also extracting lithological information, there is no nondestructive method for effectively estimating quality factors. In recent years, *Rix et al.* (2000) and *Lai et al.* (2002) obtained shear damping ratios (S-wave quality factor) using surface waves. *Xia et al.* (2002a, 2012) also inverted P-wave quality factors Qp and S-wave quality factors Qs from amplitude information of Rayleigh waves in addition to phase information. *Xia et al.* (2013a,b) further demonstrated that S-wave quality factors can be easily derived from phase and amplitude information of Love waves because Love waves are independent of P-wave velocities and P-wave quality factors. In order to establish a method to obtain quality factors from surface waves, we need to perform further case studies comparing inverted quality factors with those from logging data.

APPENDICES

APPENDIX A

Haskell's layer matrices

$$[\mathbf{A}_n(z)]_{11} = \frac{1}{d_5}(-d_4C_1 + d_3C_3)$$

$$[\mathbf{A}_n(z)]_{12} = \frac{1}{c_{33}d_6}(-\epsilon_3S_1 + \epsilon_1S_3)$$

$$[\mathbf{A}_n(z)]_{13} = \frac{1}{c_{33}d_6}(d_2S_1 - d_1S_3)$$

$$[\mathbf{A}_n(z)]_{14} = \frac{1}{c_{44}d_5}(C_1 - C_3)$$

$$[\mathbf{A}_n(z)]_{21} = \frac{1}{d_5}(-d_1d_4S_1 + d_2d_3S_3)$$

$$[\mathbf{A}_n(z)]_{22} = \frac{1}{c_{33}d_6}(-\epsilon_3d_1C_1 + \epsilon_1d_2C_3) = [\mathbf{A}_n(z)]_{11}$$

$$[\mathbf{A}_n(z)]_{23} = \frac{d_1d_2}{c_{33}d_6}(C_1 - C_3)$$

$$[\mathbf{A}_n(z)]_{24} = \frac{1}{c_{44}d_5}(d_1S_1 - d_2S_3)$$

$$[\mathbf{A}_n(z)]_{31} = \frac{1}{d_5}(-\epsilon_1d_4S_1 + \epsilon_3d_3S_3) = -[\mathbf{A}_n(z)]_{24}$$

$$[\mathbf{A}_n(z)]_{32} = \frac{\epsilon_1\epsilon_3}{c_{33}d_6}(-C_1 + C_3) = -[\mathbf{A}_n(z)]_{14}$$

$$[\mathbf{A}_n(z)]_{33} = \frac{1}{c_{33}d_6}(\epsilon_1d_2C_1 - \epsilon_3d_1C_3)$$

$$[\mathbf{A}_n(z)]_{34} = \frac{1}{c_{44}d_5}(\epsilon_1S_1 - \epsilon_3S_3)$$

$$[\mathbf{A}_n(z)]_{41} = \frac{c_{44}d_3d_4}{d_5}(-C_1 + C_3) = -[\mathbf{A}_n(z)]_{23}$$

$$[\mathbf{A}_n(z)]_{42} = \frac{c_{44}}{c_{33}d_6}(-\epsilon_3 d_3 S_1 + \epsilon_1 d_4 S_3) = -[\mathbf{A}_n(z)]_{13}$$

$$[\mathbf{A}_n(z)]_{43} = \frac{c_{44}}{c_{33}d_6}(d_2 d_3 S_1 - d_1 d_4 S_3)$$

$$[\mathbf{A}_n(z)]_{44} = \frac{1}{d_5}(d_3 C_1 - d_4 C_3) = [\mathbf{A}_n(z)]_{33}$$

APPENDIX B

Relationship among d_i

The following relationship is derived from Newton's relations of equation 2.9:

$$c_{33}c_{44}\nu_1^2\nu_3^2 = (\rho\omega^2 - c_{44}k^2)(\rho\omega^2 - c_{11}k^2).$$

From this equation, we find the following relationships among d_i:

$$\frac{d_1}{d_4} = c_{44}\epsilon_1 \quad \frac{d_2}{d_3} = c_{44}\epsilon_3 \quad \frac{d_6}{d_5} = \frac{c_{44}}{c_{33}}\epsilon_1\epsilon_3.$$

APPENDIX C

Matrix elements in the delta matrix method

In the derivation of symmetry among b_{1212}, b_{1312}, b_{1313}, b_{1412}, b_{2312}, b_{2412}, and b_{3412}, the relationship among d_i in Appendix B is used.

$$
\begin{aligned}
b_{1212}(z) &= \frac{1}{c_{33}d_5d_6}[(\epsilon_1 d_2 d_3 + \epsilon_3 d_1 d_4) - (\epsilon_1 d_2 d_4 + \epsilon_3 d_1 d_3)C_1C_3 + (\epsilon_1 d_1 d_4 + \epsilon_3 d_2 d_3)S_1S_3] \\
&= 1 - b_{1234}(z) \\
b_{1213}(z) &= \frac{1}{c_{33}d_5d_6}[d_1d_2(d_3+d_4)(C_1C_3-1) - (d_2^2d_3 + d_1^2d_4)S_1S_3] \\
b_{1214}(z) &= \frac{1}{c_{44}d_5}(-d_2C_1S_3 + d_1C_3S_1) \\
b_{1223}(z) &= \frac{1}{c_{33}d_6}(d_1C_1S_3 - d_2C_3S_1) \\
b_{1224}(z) &= \frac{1}{c_{33}c_{44}d_5d_6}[(\epsilon_1 d_2 + \epsilon_3 d_1)(1 - C_1C_3) + (\epsilon_1 d_1 + \epsilon_3 d_2)S_1S_3] \\
b_{1234}(z) &= \frac{1}{c_{33}c_{44}d_5d_6}[2d_1d_2(C_1C_3 - 1) - (d_1^2 + d_2^2)S_1S_3] \\
b_{1312}(z) &= \frac{1}{c_{33}d_5d_6}[\epsilon_1\epsilon_3(d_3+d_4)(1 - C_1C_3) + (\epsilon_1^2 d_4 + \epsilon_3^2 d_3)S_1S_3] \\
&= b_{1224}(z) \\
b_{1313}(z) &= \frac{1}{c_{33}d_5d_6}[(-(\epsilon_1 d_2 d_4 + \epsilon_3 d_1 d_3) + (\epsilon_1 d_2 d_3 + \epsilon_3 d_1 d_4)C_1C_3 - (\epsilon_1 d_1 d_4 + \epsilon_3 d_2 d_3)S_1S_3] \\
&= C_1C_3 + b_{1234}(z) \\
b_{1314}(z) &= \frac{1}{c_{44}d_5}(-\epsilon_3 C_1S_3 + \epsilon_1 C_3S_1)
\end{aligned}
$$

$$b_{1323}(z) = \frac{1}{c_{33}d_6}(\epsilon_1 C_1 S_3 - \epsilon_3 C_3 S_1)$$

$$b_{1324}(z) = \frac{1}{c_{33}c_{44}d_5d_6}[2\epsilon_1\epsilon_3(1 - C_1C_3) + (\epsilon_1^2 + \epsilon_3^2)S_1S_3]$$

$$b_{1334}(z) = -b_{1312}(z)$$

$$b_{1412}(z) = \frac{c_{44}}{c_{33}d_6}(\epsilon_1 d_4 C_1 S_3 - \epsilon_3 d_3 C_3 S_1)$$

$$= b_{1223}(z)$$

$$b_{1413}(z) = \frac{c_{44}}{c_{33}d_6}(-d_1 d_4 C_1 S_3 + d_2 d_3 C_3 S_1)$$

$$b_{1414}(z) = C_1 C_3$$

$$b_{1423}(z) = \frac{c_{44}d_5}{c_{33}d_6}S_1 S_3$$

$$b_{1424}(z) = b_{1323}(z)$$

$$b_{1434}(z) = -b_{1412}(z)$$

$$b_{2312}(z) = \frac{1}{d_5}(-\epsilon_3 d_3 C_1 S_3 + \epsilon_1 d_4 C_3 S_1)$$

$$= b_{1214}(z)$$

$$b_{2313}(z) = \frac{1}{d_5}(d_2 d_3 C_1 S_3 - d_1 d_4 C_3 S_1)$$

$$b_{2314}(z) = \frac{c_{33}d_6}{c_{44}d_5}S_1 S_3$$

$$b_{2323}(z) = b_{1414}(z)$$

$$b_{2324}(z) = b_{1314}(z)$$

$$b_{2334}(z) = -b_{2312}(z)$$

$$b_{2412}(z) = \frac{c_{44}}{c_{33}d_5d_6}[(\epsilon_1 d_2 + \epsilon_3 d_1)d_3 d_4(C_1C_3 - 1) - (\epsilon_1 d_1 d_4^2 + \epsilon_3 d_2 d_3^2)S_1S_3]$$

$$= b_{1213}(z)$$

$$b_{2413}(z) = \frac{c_{44}}{c_{33}d_5d_6}[2d_1d_2d_3d_4(1 - C_1C_3) + (d_1^2d_4^2 + d_2^2d_3^2)S_1S_3]$$

$$b_{2414}(z) = b_{2313}(z)$$

$$b_{2423}(z) = b_{1413}(z)$$

$$b_{2424}(z) = b_{1313}(z)$$

$$b_{2434}(z) = -b_{1213}(z)$$

$$b_{3412}(z) = \frac{c_{44}}{c_{33}d_5d_6}[2\epsilon_1\epsilon_3 d_3d_4(C_1C_3 - 1) - (\epsilon_1^2 d_4^2 + \epsilon_3^2 d_3^2)S_1S_3]$$

$$= b_{1234}(z)$$

$$b_{3413}(z) = -b_{1213}(z)$$

$$b_{3414}(z) = -b_{1214}(z)$$

$$b_{3423}(z) = -b_{1223}(z)$$

$$b_{3424}(z) = -b_{1224}(z)$$

$$b_{3434}(z) = b_{1212}(z)$$

APPENDIX D

HAM03

The results for site HAM03 are similar to those for site BRD02. The triangle array described in Figure 3.1b was used. Figure D.1 shows the observed SPAC and HVSR curves and estimated values of β by the three-component SPAC method. The lowest frequency of the estimated β is slightly higher than the peak frequency of the HVSR curve.

By including HVSR curves in joint inversion with weighting $w \leq 0.7$, ZLCC misfits are significantly improved (Figure D.2). We have determined the optimal value to be $w = 0.5$ for this data. Figure D.3 shows the inverted velocity models by joint inversion with $w = 1.0$ and $w = 0.5$. When only SPAC curves are considered in joint inversion, inverted velocity models at depths deeper than 20 m are not resolved. On the other hand, inclusion of HVSR curves constrains velocity contrast at about 22 m and it indicates the existence of high S-wave velocities below 30 m. From independent SCPT data, the depth of bedrock is estimated as 31.5 m which is significantly shallower than the result of joint inversion. Further investigation is necessary to explain this discrepancy; it could be due to gravels presenting a block to the cone penetrometer, or could be due to a real variation in bedrock depth between the SCPT site and the centre of the microtremor array.

When we compare the observed values with the theoretical values corresponding to the velocity models with minimum misfit functions, it can be seen that theoretical HVSR curves are significantly improved by considering HVSR curves (Figure D.4). Inclusion of the HVSR curves in inversion improves corresponding theoretical SPAC curves at low frequencies with longer receiver spacing (x = 99.9 m) rather than theoretical curves corresponding to x = 33.3 m.

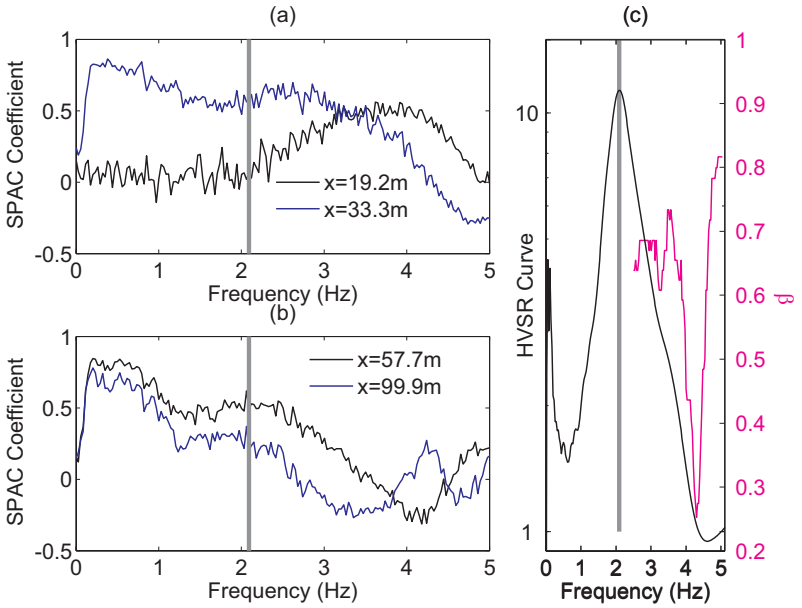

Figure D.1: The observed SPAC curves for HAM03 corresponding to (a) x = 19.2 and 33.3 and (b) x = 57.7 and 99.9 m. (c) The observed HVSR curve for HAM03. Gray lines are the peak frequency of the observed HVSR curve. The magenta line is the values of β estimated by the three-component SPAC method.

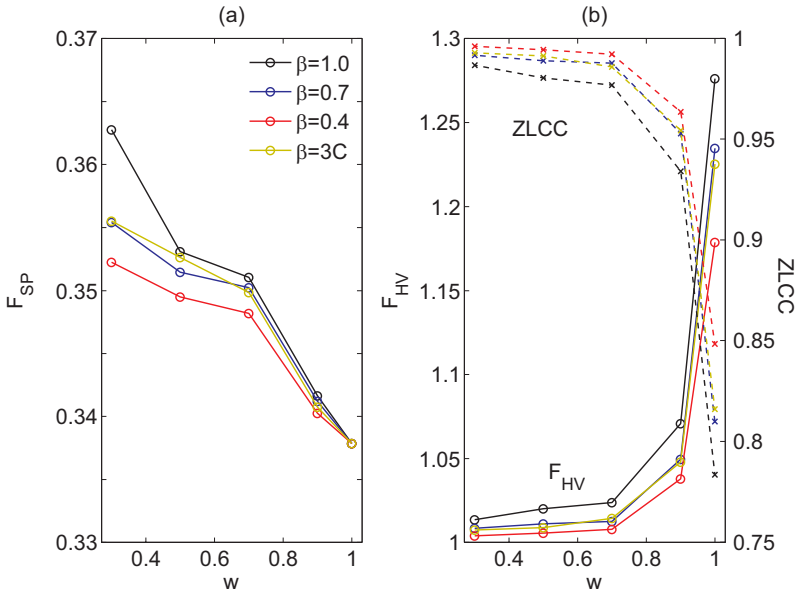

Figure D.2: Misfit functions for (a) SPAC curves and (b) HVSR curves corresponding to HAM03. ZLCC are also described as dashed lines.

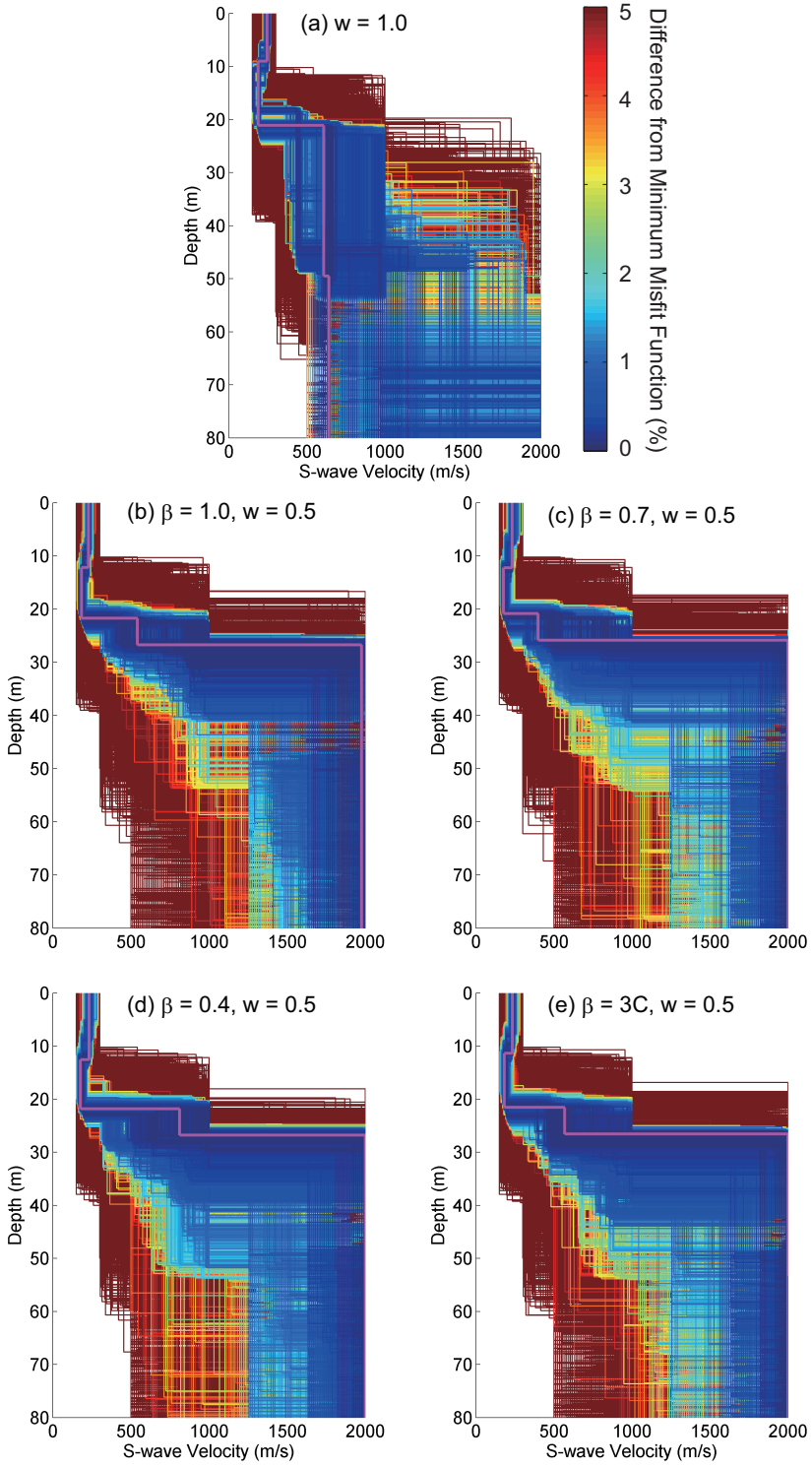

Figure D.3: Inverted velocity models by joint inversion for HAM03 when (a) $w = 1.0$, (b)-(e) $w = 0.5$ with $\beta = 1.0$, 0.7, 0.4 and 3C, respectively. Magenta lines are the velocity models with minimum misfit functions for each inversion.

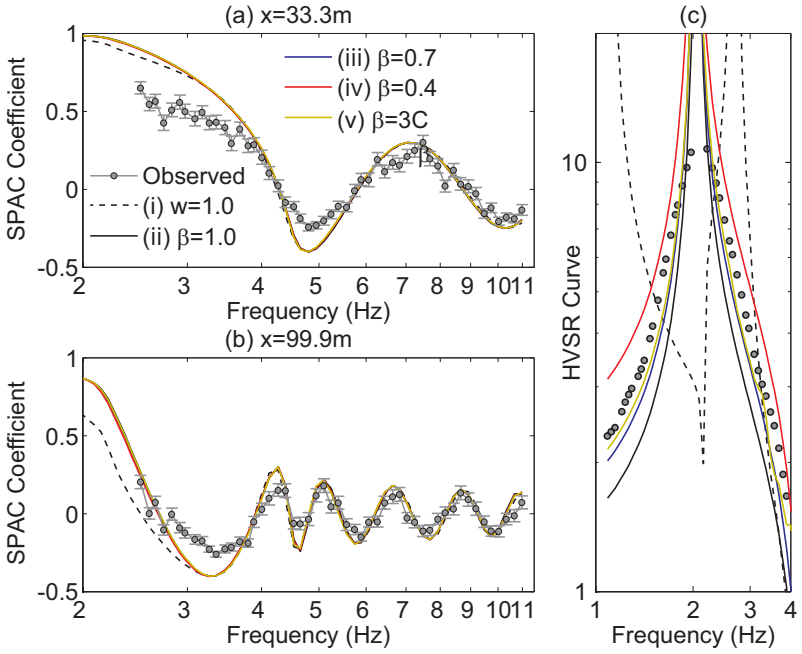

Figure D.4: Comparison of theoretical SPAC curves for the inverted velocity models with minimum misfit functions corresponding to (a) $x = 33.3$ and (b) 99.9 m and (c) HVSR curves with observed curves for HAM03 when (i) $w = 1.0$, (ii)-(v) $w = 0.5$ with $\beta = 1.0$, 0.7, 0.4 and 3C, respectively. Standard errors of SPAC curves are described in (a) and (b).

APPENDIX E

Dependence of effective phase velocities with a distance

Here, we discuss how the distance between receivers influences to the theoretical calculation of effective phase velocities by using a simulated velocity structure (Figure 4.3). Effective phase velocities from equation 4.9 using a geometry of observation array and ones for r = 7.21, 14.4, 25 and 28.9 m from equation 4.8 are shown in Figure E.1. It can be seen that effective phase velocities from equation 4.8 have some differences associated with the receiver interval. The frequency ranges where effective phase velocities can be calculated from equation 4.8 are restricted by the spatial aliasing depending on the distance (dashed lines in Figure E.1. In the calculation of effective phase velocities from equation 4.9, however, there is no effect on the spatial aliasing at more than 20 Hz in addition to an agreement with observed values. This advantage would be important in an inversion since theoretical phase velocities have to be completely covered with the frequency range where phase velocities are estimated.

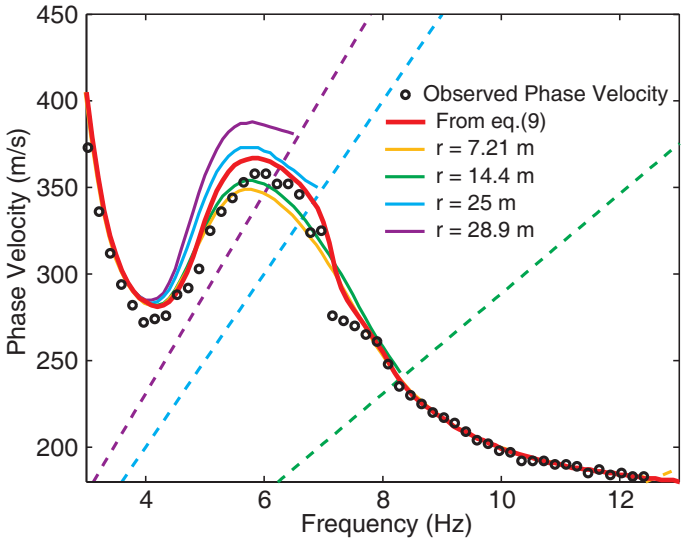

Figure E.1: Effects on the theoretical calculation of effective phase velocities depending on the distance between receivers using simulated data. Observed phase velocities (black circles), theoretical phase velocities from equation 4.9 and ones from equation 4.8 for $r = 7.21$, 14.4, 25 and 28.9 m. Dashed lines show the limit of the high frequency caused by the spatial aliasing.

APPENDIX F

Acknowledgements for published contents

F.1 Chapter 2

Computation of Rayleigh waves on transversely isotropic media by the reduced delta matrix method (http://dx.doi.org/10.1785/01200120207) published in *Bulletin of the Seismological Society of America* (2013): **103**, 2083-2093. The author gratefully acknowledges the Seismological Society of America.

F.2 Chapter 4

Multimode inversion with amplitude response of surface waves in the spatial autocorrelation method (http://dx.doi.org/10.1111/j.1365-246X.2012.05496.x) published in *Geophysical Journal International* (2012): **190**, 541-552. The author gratefully acknowledges the Royal Astronomical Society. Note that the content is slightly modified from the original paper.

F.3 Chapter 7

Window-controlled CMP crosscorrelation analysis for surface waves in laterally heterogeneous media (http://dx.doi.org/10.1190/GEO2013-0010.1) published in *Geophysics* (2013): **78**, EN95-EN105. The author gratefully acknowledges the Society of Exploration Geophysicists (SEG). SEG possesses a copyright for this content. Note that the content is slightly modified from the original paper.

BIBLIOGRAPHY

BIBLIOGRAPHY

Abbiss, C. (1983), Calculation of elasticities and settlements for long periods of time and high strains from seismic measurements, *Geotechnique*, *33*(4), 397–405.

Abo-Zena, A. (1979), Dispersion function computations for unlimited frequency values, *Geophysical Journal of the Royal Astronomical Society*, *58*(1), 91–105.

Aki, K. (1957), Space and time spectra of stationary stochastic waves, with special reference to microtremors, *Bulletin of the Earthquake Research Institute*, *35*, 415–456.

Aki, K. (1965), A note on the use of microseisms in determining the shallow structures of the earth's crust, *Geophysics*, *30*(4), 665–666.

Alvizuri, C., and T. Tanimoto (2011), Azimuthal anisotropy from array analysis of rayleigh waves in southern california, *Geophysical Journal International*, *186*(3), 1135–1151.

Anderson, D. L. (1961), Elastic wave propagation in layered anisotropic media, *Journal of Geophysical Research*, *66*(9), 2953–2963.

Arai, H., and K. Tokimatsu (2000), Effects of rayleigh and love waves on microtremor h/v spectra, in *Proc. 12th World Conf. on Earthquake Engineering*, pp. 2232–2240.

Arai, H., and K. Tokimatsu (2004), S-wave velocity profiling by inversion of microtremor h/v spectrum, *Bulletin of the Seismological Society of America*, *94*(1), 53–63.

Arai, H., and K. Tokimatsu (2005), S-wave velocity profiling by joint inversion of microtremor dispersion curve and horizontal-to-vertical (h/v) spectrum, *Bulletin of the Seismological Society of America*, *95*(5), 1766–1778.

Askari, R., J. Ferguson, and J. H. Isaac (2013), Estimation of converted waves static correction using cmp cross-correlation of surface waves, *Geophysics, in revision.*

Asten, M., and J. Roberts (2006), Analysis of esg2006 blind-trial microtremor data using the mmspac method, in *Third International Symposium on the Effects of Surface Geology on Seismic Motion, Grenoble, France*, vol. 30.

Asten, M., C. Collins, T. Volti, and T. Ikeda (2013), The good, the bad and the ugly-lessons from and methodologies for extracting shear-wave velocity profiles from microtremor array measurements in urban newcastle, *ASEG Extended Abstracts*, pp. 1–7.

Asten, M., A. Askan, E. Ekincioglu, F. Sisman, and B. Ugurhan (2014), Site characterization in northwestern turkey based on spac and hvsr analysis of microtremor noise, *Exploration Geophysics, in press*.

Asten, M. W. (1976), The use of microseisms in geophysical exploration, Ph.D. thesis, Macquarie University.

Asten, M. W. (1978), Geological control on the three-component spectra of rayleigh-wave microseisms, *Bulletin of the Seismological Society of America*, *68*(6), 1623–1636.

Asten, M. W. (2001), The spatial auto-correlation method for phase velocity of microseisms–another method for characterisation of sedimentary overburden, in *Proceedings of the 2001 Conference, Canberra*, vol. 28.

Asten, M. W. (2006), On bias and noise in passive seismic data from finite circular array data processed using spac methods, *Geophysics*, *71*(6), V153–V162.

Asten, M. W., N. Lam, G. Gibson, and J. Wilson (2002), Microtremor survey design optimised for application to site amplification and resonance modelling, in *Total Risk Management in the Privatised Era, editted by M Griffith, D. Love, P McBean, A McDougall, B. Butler, Proceedings of Conference, Australian Earthquake Engineering Soc., Adelaide*, vol. 7.

Asten, M. W., T. Dhu, and N. Lam (2004), Optimised array design for microtremor array studies applied to site classification; comparison of results with scpt logs, in *Proceedings of the 13th World Conference of Earthquake Engineering, Vancouver, Aug1-6*, vol. 2903.

Ben-Menahem, A., and S. J. Singh (1981), *Seismic waves and sources*, Springer-Verlag (New York).

Bergamo, P., D. Boiero, and L. V. Socco (2012), Retrieving 2d structures from surface-wave data by means of space-varying spatial windowing, *Geophysics*, *77*(4), EN39–EN51.

Bettig, B., P. Bard, F. Scherbaum, J. Riepl, F. Cotton, C. Cornou, and D. Hatzfeld (2001), Analysis of dense array noise measurements using the modified spatial auto-correlation method (spac): application to the grenoble area, *Bollettino di Geofisica Teorica ed Applicata*, *42*(3-4), 281–304.

Boaga, J., G. Cassiani, C. L. Strobbia, and G. Vignoli (2013), Mode misidentification in rayleigh waves: Ellipticity as a cause and a cure, *Geophysics*, *78*(4), EN17–EN28.

Bodet, L., O. Abraham, and D. Clorennec (2009), Near-offset effects on rayleigh-wave dispersion measurements: Physical modeling, *Journal of Applied Geophysics*, *68*(1), 95–103.

Bohlen, T., S. Kugler, G. Klein, and F. Theilen (2004), 1.5 d inversion of lateral variation of scholte-wave dispersion, *Geophysics*, *69*(2), 330–344.

Boiero, D., and L. V. Socco (2010), Retrieving lateral variations from surface wave dispersion curves, *Geophysical Prospecting*, *58*(6), 977–996.

Boiero, D., and L. V. Socco (2011), The meaning of surface wave dispersion curves in weakly laterally varying structures, *Near Surface Geophysics*, *9*(6), 561–570.

Boiero, D., E. Wiarda, and P. Vermeer (2013), Surface-and guided-wave inversion for near-surface modeling in land and shallow marine seismic data, *The Leading Edge*, *32*(6), 638–646.

Bonnefoy-Claudet, S., C. Cornou, J. Kristek, M. Ohrnberger, M. Wathelet, P.-Y. Bard, P. Moczo, D. Fäh, and F. Cotton (2004), Simulation of seismic ambient noise: I. results of h/v and array techniques on canonical models, in *Proceedings of the 13th World Conference on Earthquake Engineering, Vancouver, Canada, 1–6 August*, vol. 2903.

Bonnefoy-Claudet, S., C. Cécile, B. Pierre-Yves, C. Fabrice, M. Peter, K. Jozef, and D. Fäh (2006a), H/v ratio: a tool for site effects evaluation. results from 1-d noise simulations, *Geophysical Journal International*, *167*(2), 827–837.

Bonnefoy-Claudet, S., F. Cotton, and P.-Y. Bard (2006b), The nature of noise wavefield and its applications for site effects studies: a literature review, *Earth-Science Reviews*, *79*(3), 205–227.

Bonnefoy-Claudet, S., A. Köhler, C. Cornou, M. Wathelet, and P.-Y. Bard (2008), Effects of love waves on microtremor h/v ratio, *Bulletin of the Seismological Society of America*, *98*(1), 288–300.

Boore, D. M. (2004), Estimating vs (30)(or nehrp site classes) from shallow velocity models (depths $<$ 30 m), *Bulletin of the Seismological Society of America*, *94*(2), 591–597.

Borcherdt, R. D. (1994), Estimates of site-dependent response spectra for design (methodology and justification), *Earthquake spectra*, *10*(4), 617–653.

Bouchon, M., and K. Aki (1977), Discrete wave-number representation of seismic-source wave fields, *Bulletin of the Seismological Society of America*, *67*(2), 259–277.

Boxberger, T., M. Picozzi, and S. Parolai (2011), Shallow geology characterization using rayleigh and love wave dispersion curves derived from seismic noise array measurements, *Journal of Applied Geophysics*, *75*(2), 345–354.

Buchen, P., and R. Ben-Hador (1996), Free-mode surface-wave computations, *Geophysical Journal International*, *124*(3), 869–887.

Capon, J. (1969), High-resolution frequency-wavenumber spectrum analysis, *Proceedings of the IEEE*, *57*(8), 1408–1418.

Castellaro, S., and F. Mulargia (2009), Vs30 estimates using constrained h/v measurements, *Bulletin of the Seismological Society of America*, *99*(2A), 761–773.

Cercato, M. (2007), Computation of partial derivatives of rayleigh-wave phase velocity using second-order subdeterminants, *Geophysical Journal International*, *170*(1), 217–238.

Cerjan, C., D. Kosloff, R. Kosloff, and M. Reshef (1985), A nonreflecting boundary condition for discrete acoustic and elastic wave equations, *Geophysics*, *50*(4), 705–708.

Chávez-García, F. J., and F. Luzón (2005), On the correlation of seismic microtremors, *Journal of Geophysical Research*, *110*(B11).

Chen, X. (1993), A systematic and efficient method of computing normal modes for multilayered half-space, *Geophysical Journal International*, *115*(2), 391–409.

Cho, I., T. Tada, and Y. Shinozaki (2004), A new method to determine phase velocities of rayleigh waves from microseisms, *Geophysics*, *69*(6), 1535–1551.

Cho, I., T. Tada, and Y. Shinozaki (2006), Centerless circular array method: Inferring phase velocities of rayleigh waves in broad wavelength ranges using microtremor records, *Journal of Geophysical Research*, *111*(B9).

Claprood, M., M. Asten, and J. Kristek (2012), Combining hvsr microtremor observations with the spac method for site resonance study of the tamar valley in launceston (tasmania, australia), *Geophysical Journal International*, *191*(2), 765–780.

Cornou, C., M. Ohrnberger, D. Boore, K. Kudo, and P. Bard (2006), Derivation of structural models from ambient vibration array recordings: results from an international blind test, in *Proceedings 3rd International Symposium on the Effects of Surface Geology on Seismic Motion*.

Crampin, S. (1970), The dispersion of surface waves in multilayered anisotropic media, *Geophysical Journal of the Royal Astronomical Society*, *21*(3), 387–402.

Crampin, S. (1981), A review of wave motion in anisotropic and cracked elastic-media, *Wave motion*, *3*(4), 343–391.

Crampin, S., and S. Peacock (2008), A review of the current understanding of seismic shear-wave splitting in the earth ' s crust and common fallacies in interpretation, *Wave Motion*, *45*(6), 675–722.

Crampin, S., R. Evans, B. Üçer, M. Doyle, J. P. Davis, G. V. Yegorkina, and A. Miller (1980), Observations of dilatancy-induced polarization anomalies and earthquake prediction, *Nature*, *286*(5776), 874–877.

Dal Moro, G. (2008), Vs and vp vertical profiling via joint inversion of rayleigh waves and refraction travel times by means of bi-objective evolutionary algorithm, *Journal of Applied Geophysics*, *66*(1), 15–24.

Dal Moro, G., and F. Ferigo (2011), Joint analysis of rayleigh-and love-wave dispersion: Issues, criteria and improvements, *Journal of Applied Geophysics*, *75*(3), 573–589.

Dunkin, J. W. (1965), Computation of modal solutions in layered, elastic media at high frequencies, *Bulletin of the Seismological Society of America*, *55*(2), 335–358.

Endrun, B. (2011), Love wave contribution to the ambient vibration h/v amplitude peak observed with array measurements, *Journal of seismology*, *15*(3), 443–472.

Fäh, D., F. Kind, and D. Giardini (2003), Inversion of local s-wave velocity structures from average h/v ratios, and their use for the estimation of site-effects, *Journal of Seismology*, *7*(4), 449–467.

Feng, S., T. Sugiyama, and H. Yamanaka (2005), Effectiveness of multi-mode surface wave inversion in shallow engineering site investigations, *Exploration Geophysics*, *36*(1), 26–33.

Forbriger, T. (2003), Inversion of shallow-seismic wavefields: Ii. inferring subsurface properties from wavefield transforms, *Geophysical Journal International*, *153*(3), 735–752.

Foti, S. (2000), Multistation methods for geotechnical characterization using surface waves, Ph.D. thesis, Politecnico di Torino.

Foti, S. (2005), Surface wave testing for geotechnical characterization, *direct and inverse modelling for soils and rocks, CISM Series*.

Foti, S., C. Comina, D. Boiero, and L. V. Socco (2009), Non-uniqueness in surface-wave inversion and consequences on seismic site response analyses, *Soil Dynamics and Earthquake Engineering*, *29*(6), 982–993.

Friederich, W., and Z.-X. Huang (1996), Evidence for upper mantle anisotropy beneath southern germany from love and rayleigh wave dispersion, *Geophysical research letters*, *23*(10), 1135–1138.

Gaherty, J. B. (2004), A surface wave analysis of seismic anisotropy beneath eastern north america, *Geophysical Journal International*, *158*(3), 1053–1066.

Galgaro, A., J. Boaga, and M. Rocca (2013), Hvsr technique as tool for thermal-basin characterization: a field example in n-e italy, *Environmental Earth Sciences*, pp. 1–14.

Goldberg, D. E. (1989), Genetic algorithms in search, optimization, and machine learning, *Reading, MA: Addison-Wesley*.

Grandjean, G., and A. Bitri (2006), 2m-sasw: Multifold multichannel seismic inversion of local dispersion of rayleigh waves in laterally heterogeneous subsurfaces: application to the super-sauze earthflow, france, *Near surface geophysics*, *4*(6), 367–375.

Gucunski, N., and R. D. Woods (1992), Numerical simulation of the sasw test, *Soil Dynamics and Earthquake Engineering*, *11*(4), 213–227.

Harkrider, D. G. (1964), Surface waves in multilayered elastic media i. rayleigh and love waves from buried sources in a multilayered elastic half-space, *Bulletin of the Seismological Society of America*, *54*(2), 627–679.

Harkrider, D. G. (1970), Surface waves in multilayered elastic media. part ii. higher mode spectra and spectral ratios from point sources in plane layered earth models, *Bulletin of the Seismological Society of America*, *60*(6), 1937–1987.

Harkrider, D. G., and D. L. Anderson (1962), Computation of surface wave dispersion for multilayered anisotropic media, *Bulletin of the Seismological Society of America*, *52*(2), 321–332.

Haskell, N. A. (1953), The dispersion of surface waves on multilayered media, *Bulletin of the Seismological Society of America*, *43*, 17–34.

Hayashi, K. (2008), Development of surface-wave methods and its application to site investigations, Ph.D. thesis, Kyoto University.

Hayashi, K., and M. Saito (2004), The dispersion curve of p-sv wave propagation with a high velocity top layer and its analysis (in japanese), in *110th SEGJ conference*, pp. 39–42.

Hayashi, K., and H. Suzuki (2004), Cmp cross-correlation analysis of multi-channel surface-wave data, *Exploration Geophysics*, *35*(1), 7–13.

Hayashi, K., T. Matsuoka, and H. Hatakeyama (2005), Joint analysis of a surface-wave method and micro-gravity survey, *Journal of Environmental & Engineering Geophysics*, *10*(2), 175–184.

Hayashi, K., A. Nozu, M. Tanaka, H. Suzuki, and E. O. Shelley (2011), Joint inversion of three-component microtremor measurements and microtremor array measurements at mexico city, in *2011 SEG Annual Meeting*.

Heisey, J. S., I. Stokoe, W. R. Hudson, and A. Meyer (1982), *Determination of in situ shear wave velocities from spectral analysis of surface waves*, Center for Transportation Research, Bureau of Engineering Research, University of Texas at Austin (Austin).

Hobiger, M., P.-Y. Bard, C. Cornou, and N. Le Bihan (2009), Single station determination of rayleigh wave ellipticity by using the random decrement technique (raydec), *Geophysical Research Letters*, *36*(14).

Hobiger, M., et al. (2013), Ground structure imaging by inversions of rayleigh wave ellipticity: sensitivity analysis and application to european strong-motion sites, *Geophysical Journal International*, *192*(1), 207–229.

Ikeda, M., S. Toda, S. Kobayashi, Y. Ohno, N. Nishizaka, and I. Ohno (2009), Tectonic model and fault segmentation of the median tectonic line active fault system on shikoku, japan, *Tectonics*, *28*(5), TC5006.

Ikeda, T., and T. Matsuoka (2013), Computation of rayleigh waves on transversely isotropic media by the reduced delta matrix method, *Bulletin of the Seismological Society of America*, *103*(3), 2083–2093.

Ikeda, T., T. Matsuoka, T. Tsuji, and K. Hayashi (2012), Multimode inversion with amplitude response of surface waves in the spatial autocorrelation method, *Geophysical Journal International*, *190*(1), 541–552.

Ikeda, T., T. Tsuji, and T. Matsuoka (2013a), Retrieving two-dimensional s-wave velocity structure by the cmp cross-correlation analysis for surface waves with spatial window, in *Near surface Geophysics Asia Pacific Conference, Beijin, China*.

Ikeda, T., T. Tsuji, and T. Matsuoka (2013b), Window-controlled cmp crosscorrelation analysis for surface waves in laterally heterogeneous media, *Geophysics*, *78*(6), EN95–EN105.

Ivanov, J., R. D. Miller, J. Xia, D. Steeples, and C. B. Park (2006), Joint analysis of refractions with surface waves: An inverse solution to the refraction-traveltime problem, *Geophysics*, *71*(6), R131–R138.

Johnson, D. H., and D. E. Dudgeon (1993), *Array signal processing: concepts and techniques*, PTR Prentice Hall.

Kasamatsu, K., and H. Yamanaka (2006), Estimation of a 3d basin model around the fault area of the 2004 mid niigata prefecture earthquake using simulation of earthquake ground motion from small events(in japanese), *Butsuri-tansa*, *59*(5), 475–484.

Kato, A., S. Onozuka, and T. Nakayama (2008), Elastic property changes in a bitumen reservoir during steam injection, *The Leading Edge*, *27*(9), 1124–1131.

Kawasaki, I., and K. Koketsu (1990), Rayleigh-love wave coupling in an azimuthally anisotropic medium, *Journal of Physics of the Earth*, *38*(5), 361–390.

Kennett, B. (1974), Reflections, rays, and reverberations, *Bulletin of the Seismological Society of America*, *64*(6), 1685–1696.

Kennett, B., and N. Kerry (1979), Seismic waves in a stratified half space, *Geophysical Journal International*, *57*(3), 557–583.

Kitsunezaki, C., N. Goto, Y. Kobayashi, T. Ikawa, M. Horike, T. Saito, T. Kurota, K. Yamane, and K. Okuzumi (1990), Estimation of p-and s-wave velocities in deep soil deposits for evaluating ground vibrations in earthquake(in japanese), *Sizen-saigai-kagaku*, *9*, 1–17.

Köhler, A., M. Ohrnberger, F. Scherbaum, M. Wathelet, and C. Cornou (2007), Assessing the reliability of the modified three-component spatial autocorrelation technique, *Geophysical Journal International*, *168*(2), 779–796.

Konno, K., and T. Ohmachi (1998), Ground-motion characteristics estimated from spectral ratio between horizontal and vertical components of microtremor, *Bulletin of the Seismological Society of America*, *88*(1), 228–241.

Kramer, S. L. (1996), *Geotechnical earthquake engineering*, Pearson Education India.

Lacoss, R., E. Kelly, and M. Toksöz (1969), Estimation of seismic noise structure using arrays, *Geophysics*, *34*(1), 21–38.

Lai, C. G., G. J. Rix, S. Foti, and V. Roma (2002), Simultaneous measurement and inversion of surface wave dispersion and attenuation curves, *Soil Dynamics and Earthquake Engineering*, *22*(9), 923–930.

Lin, C.-P., and C.-H. Lin (2007), Effect of lateral heterogeneity on surface wave testing: Numerical simulations and a countermeasure, *Soil Dynamics and Earthquake Engineering*, *27*(6), 541–552.

Lin, C.-P., C.-C. Chang, and T.-S. Chang (2004), The use of masw method in the assessment of soil liquefaction potential, *Soil Dynamics and Earthquake Engineering*, *24*(9), 689–698.

Ling, S., and H. Okada (1993), An extended use of the spatial autocorrelation method for the estimation of geological structure using microtremors(in japanese), in *89th SEGJ conference*, pp. 44–48.

Louie, J. N. (2001), Faster, better: shear-wave velocity to 100 meters depth from refraction microtremor arrays, *Bulletin of the Seismological society of America*, *91*(2), 347–364.

Lu, L., and B. Zhang (2006), Inversion of rayleigh waves using a genetic algorithm in the presence of a low-velocity layer, *Acoustical Physics*, *52*(6), 701–712.

Lu, L., C. Wang, and B. Zhang (2007), Inversion of multimode rayleigh waves in the presence of a low-velocity layer: numerical and laboratory study, *Geophysical Journal International*, *168*(3), 1235–1246.

Ludwig, W. J., J. E. Nafe, and C. L. Drake (1970), Seismic refraction, *The Sea: Ideas and observations on progress in the study of the seas*, *4*(Part 1), 53–84.

Luo, Y., J. Xia, J. Liu, Q. Liu, and S. Xu (2007), Joint inversion of high-frequency surface waves with fundamental and higher modes, *Journal of Applied Geophysics*, *62*(4), 375–384.

Luo, Y., J. Xia, R. D. Miller, Y. Xu, J. Liu, and Q. Liu (2009), Rayleigh-wave mode separation by high-resolution linear radon transform, *Geophysical Journal International*, *179*(1), 254–264.

Mandal, B., and B. Mitchell (1986), Complete seismogram synthesis for transversely isotropic media, *J. Geophys*, *59*, 149–156.

Maraschini, M., and S. Foti (2010), A monte carlo multimodal inversion of surface waves, *Geophysical Journal International*, *182*(3), 1557–1566.

Maraschini, M., F. Ernst, S. Foti, and L. V. Socco (2010), A new misfit function for multimodal inversion of surface waves, *Geophysics*, *75*(4), G31–G43.

Matsuoka, M., K. Wakamatsu, K. Fujimoto, and S. Midorikawa (2005), Average shear-wave velocity mapping using japan engineering geomorphologic classification map(in japanese), *JSCE journal*, *794*, 239–251.

Matsushima, T., and H. Okada (1990), An exploration method using microtremors, part 2: An experiment to identify love waves in long- period microtremors(in japanese), in *82th SEGJ conference*, pp. 5–8.

Maupin, V. (2011), Upper-mantle structure in southern norway from beamforming of rayleigh wave data presenting multipathing, *Geophysical Journal International*, *185*(2), 985–1002.

Maupin, V., and M. Cara (1992), Love-rayleigh wave incompatibility and possible deep upper mantle anisotropy in the iberian peninsula, *pure and applied geophysics*, *138*(3), 429–444.

McPherson, A., and L. Hall (2013), Site classification for earthquake hazard and risk assessment in australia, *Bulletin of the Seismological Society of America*, *103*(2A), 1085–1102.

Miller, R. D., J. Xia, C. B. Park, and J. M. Ivanov (1999), Multichannel analysis of surface waves to map bedrock, *The Leading Edge*, *18*(12), 1392–1396.

Minato, S., T. Tsuji, T. Matsuoka, N. Nishizaka, and M. Ikeda (2012), Global optimisation by simulated annealing for common reflection surface stacking and its application to low-fold marine data in southwest japan, *Exploration Geophysics*, *43*(2), 59–69.

Nakamura, Y. (1989), A method for dynamic characteristics estimation of subsurface using microtremor on the ground surface, *Railway Technical Research Institute, Quarterly Reports*, *30*(1).

Nakayama, T., A. Takahashi, L. Skinner, and A. Kato (2008), Monitoring an oil-sands reservoir in northwest alberta using time-lapse 3d seismic and 3d p-sv converted-wave data, *The Leading Edge*, *27*(9), 1158–1175.

Nazarian, S., and K. Stokoe (1984), In situ shear wave velocities from spectral analysis of surface waves, in *Proceedings of the world conference on Earthquake Engineering*, vol. 3, pp. 31–38.

Nazarian, S., I. Stokoe, and W. R. Hudson (1983), Use of spectral analysis of surface waves method for determination of moduli and thicknesses of pavement systems, *Transportation Research Record*, *930*, 38–45.

Nishida, K., H. Kawakatsu, Y. Fukao, and K. Obara (2008), Background love and rayleigh waves simultaneously generated at the pacific ocean floors, *Geophysical Research Letters*, *35*(16), L16,307.

Nogoshi, M., and T. Igarashi (1971), On the amplitude characteristics of microtremor (part 2)(in japanese), *Jour. Seism. Soc. Japan*, *24*(26-40).

Obando, E. A., C. B. Park, N. Ryden, and P. Ulriksen (2010), Phase-scanning approach to correct time-shift inaccuracies in the surface-wave walk-away method, *Soil Dynamics and Earthquake Engineering*, *30*(12), 1528–1539.

Obuchi, T., H. Yamamoto, T. Sano, and T. Saito (2004), Estimation of underground velocity structure based on both fundamental and higher modes(in japanese), in *111th SEGJ conference*, pp. 25–28.

Ohori, M., A. Nobata, and K. Wakamatsu (2002), A comparison of esac and fk methods of estimating phase velocity using arbitrarily shaped microtremor arrays, *Bulletin of the Seismological Society of America*, *92*(6), 2323–2332.

Okada, A. (1972), Quaternary faulting of the median tectonic line fault system in the northwestern part of shikoku, *Bull. Fac. Liter. Aichi Prefect. Univ*, *23*, 68–94.

Okada, H. (2003), *The microtremor survey method*, vol. 12, Society of Exploration Geophysicists with the cooperation of Society of Exploration Geophysicists of Japan and Australian Society of Exploration Geophysicists.

Okada, H. (2008), Present situation of the microtremor survey method and subject related to its practical application(in japanese), *Butsuri-tansa*, *61*, 445–456.

O'Neill, A. (2003), Full-waveform reflectivity for modelling, inversion and appraisal of seismic surface wave dispersion in shallow site investigations, Ph.D. thesis, University of Western Australia.

O'Neill, A., and T. Matsuoka (2005), Dominant higher surface-wave modes and possible inversion pitfalls, *Journal of Environmental & Engineering Geophysics*, *10*(2), 185–201.

O'Neill, A., M. Dentith, and R. List (2003), Full-waveform p-sv reflectivity inversion of surface waves for shallow engineering applications, *Exploration Geophysics*, *34*(3), 158–173.

Pan, Y., J. Xia, L. Gao, C. Shen, and C. Zeng (2013), Calculation of rayleigh-wave phase velocities due to models with a high-velocity surface layer, *Journal of Applied Geophysics*, *96*, 1–6.

Park, C. B. (2011), Imaging dispersion of masw data-full vs. selective offset scheme, *Journal of Environmental and Engineering Geophysics*, *16*(1), 13–23.

Park, C. B., R. D. Miller, J. Xia, et al. (1998), Imaging dispersion curves of surface waves on multi-channel record, in *SEG Expanded Abstracts*, pp. 1377–1380.

Park, C. B., R. D. Miller, and J. Xia (1999a), Multichannel analysis of surface waves, *Geophysics*, *64*(3), 800–808.

Park, C. B., R. D. Miller, and J. Xia (1999b), Multimodal analysis of high frequency surface waves, in *Proceedings of the symposium on the application of geophysics to engineering and environmental problems*, vol. 99, pp. 115–121.

Park, J. (1996), Surface waves in layered anisotropic structures, *Geophysical Journal International*, *126*(1), 173–183.

Parolai, S., M. Picozzi, S. Richwalski, and C. Milkereit (2005), Joint inversion of phase velocity dispersion and h/v ratio curves from seismic noise recordings using a genetic algorithm, considering higher modes, *Geophysical research letters*, *32*(1).

Piatti, C., L. Socco, D. Boiero, and S. Foti (2013), Constrained 1d joint inversion of seismic surface waves and p-refraction traveltimes, *Geophysical Prospecting*, *61*, 77–93.

Picozzi, M., and D. Albarello (2007), Combining genetic and linearized algorithms for a two-step joint inversion of rayleigh wave dispersion and h/v spectral ratio curves, *Geophysical Journal International*, *169*(1), 189–200.

Picozzi, M., S. Parolai, and S. Richwalski (2005), Joint inversion of h/v ratios and dispersion curves from seismic noise: Estimating the s-wave velocity of bedrock, *Geophysical research letters*, *32*(11), L11,308.

Picozzi, M., S. Parolai, and D. Bindi (2010), Deblurring of frequency–wavenumber images from small-scale seismic arrays, *Geophysical Journal International*, *181*(1), 357–368.

Poggi, V., and D. Fäh (2010), Estimating rayleigh wave particle motion from three-component array analysis of ambient vibrations, *Geophysical Journal International*, *180*(1), 251–267.

Richwalski, S. M., M. Picozzi, S. Parolai, C. Milkereit, F. Baliva, D. Albarello, K. Roy-Chowdhury, H. van der Meer, and J. Zschau (2007), Rayleigh wave dispersion curves from seismological and engineering-geotechnical methods: a comparison at the bornheim test site (germany), *Journal of Geophysics and Engineering*, *4*, 349–361.

Rix, G. J., C. G. Lai, and A. W. Spang Jr (2000), In situ measurement of damping ratio using surface waves, *Journal of geotechnical and geoenvironmental engineering*, *126*(5), 472–480.

Roberts, J. C., and M. W. Asten (2004), Resolving a velocity inversion at the geotechnical scale using the microtremor (passive seismic) survey method, *Exploration geophysics*, *35*(1), 14–18.

Roten, D., D. Fäh, C. Cornou, and D. Giardini (2006), Two-dimensional resonances in alpine valleys identified from ambient vibration wavefields, *Geophysical Journal International*, *165*(3), 889–905.

Ryden, N., and M. J. Lowe (2004), Guided wave propagation in three-layer pavement structures, *The Journal of the Acoustical Society of America*, *116*, 2902–2913.

Ryden, N., and C. B. Park (2006), Fast simulated annealing inversion of surface waves on pavement using phase-velocity spectra, *Geophysics*, *71*(4), R49–R58.

Saito, M. (1988), Disper80: A subroutine package for the calculation of seismic normal-mode solutions, *Seismological Algorithms*, pp. 293–319.

Saito, M., and H. Kabasawa (1993), Computations of reflectivity and surface wave dispersion curves for layered media; 2. rayleigh wave calculations(in japanese), *Butsuri-tansa*, *46*, 283–298.

Scherbaum, F., K.-G. Hinzen, and M. Ohrnberger (2003), Determination of shallow shear wave velocity profiles in the cologne, germany area using ambient vibrations, *Geophysical Journal International*, *152*(3), 597–612.

Schwab, F. (1970), Surface-wave dispersion computations: Knopoff's method, *Bulletin of the Seismological Society of America*, *60*(5), 1491–1520.

Schwab, F., and L. Knopoff (1972), Fast surface wave and free mode computations, *Methods in computational physics*, *11*, 87–180.

Sen, M. K., and P. L. Stoffa (1995), *Global optimization methods in geophysical inversion*, Elsevier.

Silver, P. G., and W. W. Chan (1991), Shear wave splitting and subcontinental mantle deformation, *Journal of Geophysical Research*, *96*(B10), 16,429–16,454.

Socco, L. V., S. Foti, and D. Boiero (2010), Surface-wave analysis for building near-surface velocity models-established approaches and new perspectives, *Geophysics*, *75*(5), 75A83–75A102.

Socco, L. V., D. Boiero, M. Maraschini, M. Vanneste, C. Madshus, H. Westerdahl, K. Duffaut, and E. Skomedal (2011), On the use of the norwegian geotechnical institute's prototype seabed-coupled shear wave vibrator for shallow soil characterization–ii. joint inversion of multimodal love and scholte surface waves, *Geophysical Journal International*, *185*(1), 237–252.

Strobbia, C., and S. Foti (2006), Multi-offset phase analysis of surface wave data (mopa), *Journal of Applied Geophysics*, *59*(4), 300–313.

Strobbia, C., A. El Emam, J. Al-Genai, and J. Roth (2010), Rayleigh wave inversion for the near-surface characterization of shallow targets in a heavy oil field in kuwait, *First Break*, *28*(5), 102–109.

Strobbia, C., A. Laake, P. Vermeer, and A. Glushchenko (2011), Surface waves: use them then lose them. surface-wave analysis, inversion and attenuation in land reflection seismic surveying, *Near Surface Geophysics*, *9*(6), 503–514.

Suzuki, H., and T. Takahashi (1999), S-wave velocity survey in tukuba city by array microtremor measurements comparison with deep borehole data(in japanese), in *101th SEGJ conference*, pp. 50–53.

Takeuchi, H., and M. Saito (1972), Seismic surface waves, *Methods in computational physics*, *11*, 217–295.

Thomson, W. T. (1950), Transmission of elastic waves through a stratified solid medium, *Journal of Applied Physics*, *21*, 89–93.

Tokimatsu, K. (1997), Geotechnical site characterization using surface waves, in *in Ishihara, K. ed., Earthquake Geotechnical Engineering: Proceedings of IS-Tokyo' 95, The First International Conference on Earthquake Geotechnical Engineering, A. A. Balkema, Rotterdam*, pp. 1333–1368.

Tokimatsu, K., K. Shinzawa, and S. Kuwayama (1992a), Use of short-period microtremors for vs profiling, *Journal of Geotechnical Engineering*, *118*(10), 1544–1558.

Tokimatsu, K., S. Tamura, and H. Kojima (1992b), Effects of multiple modes on rayleigh wave dispersion characteristics, *Journal of Geotechnical Engineering*, *118*(10), 1529–1543.

Tsuji, T., T. A. Johansen, B. O. Ruud, T. Ikeda, and T. Matsuoka (2012), Surface-wave analysis for identifying unfrozen zones in subglacial sediments, *Geophysics*, *77*(3), EN17–EN27.

Vignoli, G., and G. Cassiani (2010), Identification of lateral discontinuities via multi-offset phase analysis of surface wave data, *Geophysical Prospecting*, *58*(3), 389–413.

Virieux, J. (1986), P-sv wave propagation in heterogeneous media: Velocity-stress finite-difference method, *Geophysics*, *51*(4), 889–901.

Volti, T., C. Collins, and M. Asten (2013), The 2012 newcastle and sydney spac microtremor surveys using geopsy software and comparisons, *ASEG Extended Abstracts*, pp. 1–6.

Wald, D. J., and T. I. Allen (2007), Topographic slope as a proxy for seismic site conditions and amplification, *Bulletin of the Seismological Society of America*, *97*(5), 1379–1395.

Watanabe, Y., S. Sassa, F. Yamada, and K. Hayashi (2011), Improvement of estimation accuracy of sandflat stratigraphy with intermediate soft sublayer-combination use of masw and microtremor array measurements, *Journal of Japan Society of Civil Engineers, Ser. B2 (Coastal Engineering)*, *67*(2), I_1361–I_1365.

Wathelet, M., D. Jongmans, and M. Ohrnberger (2005), Direct inversion of spatial autocorrelation curves with the neighborhood algorithm, *Bulletin of the Seismological Society of America*, *95*(5), 1787–1800.

Wathelet, M., D. Jongmans, M. Ohrnberger, and S. Bonnefoy-Claudet (2008), Array performances for ambient vibrations on a shallow structure and consequences over vs inversion, *Journal of Seismology*, *12*(1), 1–19.

Watson, T. (1970), A note on fast computation of rayleigh wave dispersion in the multilayered elastic half-space, *Bulletin of the Seismological Society of America*, *60*(1), 161–166.

Xia, J., R. D. Miller, and C. B. Park (1999), Estimation of near-surface shear-wave velocity by inversion of rayleigh waves, *Geophysics*, *64*(3), 691–700.

Xia, J., R. D. Miller, C. B. Park, and G. Tian (2002a), Determining q of near-surface materials from rayleigh waves, *Journal of applied geophysics*, *51*(2), 121–129.

Xia, J., R. D. Miller, C. B. Park, E. Wightman, and R. Nigbor (2002b), A pitfall in shallow shear-wave refraction surveying, *Journal of applied geophysics*, *51*(1), 1–9.

Xia, J., R. D. Miller, C. B. Park, and G. Tian (2003), Inversion of high frequency surface waves with fundamental and higher modes, *Journal of Applied Geophysics*, *52*(1), 45–57.

Xia, J., Y. Xu, R. D. Miller, and J. Ivanov (2012), Estimation of near-surface quality factors by constrained inversion of rayleigh-wave attenuation coefficients, *Journal of Applied Geophysics*, *82*, 137–144.

Xia, J., C. Shen, and Y. Xu (2013a), Near-surface shear-wave velocities and quality factors derived from high-frequency surface waves, *The Leading Edge*, *32*(6), 612–618.

Xia, J., X. Yin, and Y. Xu (2013b), Feasibility of determining q of near-surface materials from love waves, *Journal of Applied Geophysics*, *95*, 47–52.

Xu, P., S. Ling, C. Li, J. Du, D. Zhang, X. Xu, K. Dai, and Z. Zhang (2012), Mapping deeply-buried geothermal faults using microtremor array analysis, *Geophysical Journal International*, *188*(1), 115–122.

Yamanaka, H., and H. Ishida (1996), Application of genetic algorithms to an inversion of surface-wave dispersion data, *Bulletin of the Seismological Society of America*, *86*(2), 436–444.

Yamanaka, H., and N. Yamada (2006), Modeling 3d s-wave velocity structure of kanto basin for estimation of earthquake ground motion(in japanese), *Butsuritansa*, *59*(6), 549–560.

Yokoi, T. (2010), New formulas derived from seismic interferometry to simulate phase velocity estimates from correlation methods using microtremor, *Geophysics*, *75*(4), SA71–SA83.

Zhang, S. X., and L. S. Chan (2003), Possible effects of misidentified mode number on rayleigh wave inversion, *Journal of Applied Geophysics*, *53*(1), 17–29.

Zhang, S. X., Y. Wang, H.-W. Zhou, and L. S. Chan (2009), Dispersion splitting of rayleigh waves in layered azimuthally anisotropic media, *Journal of Applied Geophysics*, *67*(2), 130–142.

Zor, E., S. Özalaybey, A. Karaaslan, M. C. Tapırdamaz, S. Ç. Özalaybey, A. Tarancıoğlu, and B. Erkan (2010), Shear wave velocity structure of the izmit bay area (turkey) estimated from active–passive array surface wave and single-station microtremor methods, *Geophysical Journal International*, *182*(3), 1603–1618.